Final Technical Report to the Department of Energy, National Energy Technology Lab

Intermetallic Strengthened Alumina-Forming Austenitic Steels for Energy Applications

DOE Award Number: DE-FE0008857

09/07/2012 to 12/17/2015

By

Bin Hu and Ian Baker

Thayer School of Engineering,
Dartmouth College,
Hanover NH 03755, USA

March 2016

Abstract

In order to achieve energy conversion efficiencies of >50 % for steam turbines/boilers in power generation systems, the materials required must be strong, corrosion-resistant at high temperatures (>700°C), and economically viable. Austenitic steels strengthened with Laves phase and $L1_2$ precipitates, and alloyed with aluminum to improve oxidation resistance, are potential candidate materials for these applications. The creep resistance of these alloys is significantly improved through intermetallic strengthening (Laves-Fe_2Nb + $L1_2$-Ni_3Al precipitates) without harmful effects on oxidation resistance.

Microstructural and microchemical analyses of the recently developed alumina-forming austenitic (AFA) steels (Fe-14Cr-32Ni-3Nb-3Al-2Ti-based) indicated they are strengthened by Ni_3Al(Ti) $L1_2$, NiAl B2, Fe_2Nb Laves phase and MC carbide precipitates. Different thermo-mechanical treatments (TMTs) were performed on these stainless steels in an attempt to further improve their mechanical properties. The thermo-mechanical processing produced nanocrystalline grains in AFA alloys and dramatically increased their yield strength at room temperature. Unfortunately, the TMTs didn't increase the yield strengths of AFA alloys at ≥700ºC. At these temperatures, dislocation climb is the dominant mechanism for deformation of TMT alloys according to strain rate jump tests. After the characterization of aged AFA alloys, we found that the largest strengthening effect from $L1_2$ precipitates can be obtained by aging for less than 24 h. The coarsening behavior of the $L1_2$ precipitates was not influenced by carbon and boron additions. Failure analysis and post-mortem TEM analysis were performed to study the creep failure mechanisms of these AFA steels after creep tests. Though the Laves and B2-NiAl phase precipitated along the boundaries can improve the creep properties, cracks were still initiated and propagated along the boundaries, which suggests that the boundaries are still the weaker regions for causing fracture during creep, possibly due to the presence of a precipitate-free zone. The precipitate size distribution and kinetics of precipitate growth were quantified.

Table of Contents

1. Executive Summary

This final report to the Department of Energy (DOE) for task of DE-FE0008857 covers the period from September 2012 to December 2015. Under this task, DOE awarded Dartmouth College $294,072 to conduct research on intermetallic strengthened alumina-forming austenitic steels for energy applications.

This research project studied the microstructure and mechanical properties of recently developed alumina forming austenitic (AFA) stainless steels, specifically the Fe-14Cr-32Ni-3Nb-3Al-2Ti wt.% based AFA alloy after two kinds of thermo-mechanical treatments (TMTs). The major research accomplishments under this task can be divided in five laboratory experiments.

1. Microstructure and room temperature mechanical analysis
2. High temperature mechanical analysis
3. Analysis of precipitate size distributions and precipitate kinetics
4. Boron and carbon effects on AFA alloys
5. Failure analysis of AFA creep specimens

The materials used in this study were obtained from Oak Ridge National Laboratory (ORNL). Ingots of the alloys had been hot-rolled at 1100ºC (80 % thickness reduction with ~15-20 % thickness reduction per pass) and then annealed at 1100ºC for 30 min in Ar + 4 % H_2 gas, followed by air-cooling.

This project started with microstructural and microchemical analyses of these intermetallic strengthened AFA alloys in a scanning electron microscope (SEM) and transmission electron microscope (TEM) in the Dartmouth EM facility. The microchemistry of the precipitates, as determined by energy-dispersive x-ray spectroscopy in the SEM and TEM, was also studied.

Two different TMTs – cold rolling followed by various anneals - were carried out on these AFA steels in an attempt to further improve their mechanical properties. The microstructural and microchemical analyses were again performed after the thermo-mechanical processing. Synchrotron X-ray diffraction at Argonne National Laboratory (ANL) was used to measure the lattice parameters of these steels after different TMTs. The room temperature mechanical properties of the TMT alloys were performed in our materials lab.

Tensile tests at elevated temperatures were performed to study mechanical behaviors of this novel alloy system; the deformation mechanisms were studied by strain rate jump tests at elevated temperatures.

The effect of boron and carbon additions on the aged AFA alloys was investigated by comparing two alloys with and without boron and carbon. The microstructure and elevated temperature mechanical properties were studied to explore influence of boron addition.

Failure analysis and post-mortem TEM analysis were performed at the Dartmouth EM facility to study the creep failure mechanisms of these AFA steels after creep tests performed at Carpenter Technology Corporation (Wyomissing, PA).

Finally, this report summarizes other activities that we engaged in to support the advanced materials for future clean coal research, such as professional presentations, and publication in peer reviewed journals.

2. Experiments:

2.1 Overview of Work

This research first investigated the effect of TMTs on the microstructure and room temperature mechanical properties of recently-developed AFA stainless steels, specifically the Fe-14Cr-32Ni-3Nb-3Al-2Ti wt.% based AFA alloys. During the TMTs, the as-received AFA alloys were cold-rolled to a 90 % thickness reduction (both with and without a solutionizing anneal at 1200ºC) and then heat treated at 800ºC for 2.4, 24, or 240 h. Detailed microstructural analysis was performed on the samples before and after two thermo-mechanical treatments using a scanning electron microscope (SEM), transmission electron microscope (TEM), and synchrotron-based X-ray diffraction (XRD). The TMT reduced the grain size significantly to the nanoscale (~100 nm) and increased the room temperature yield strength to above 1000 MPa.

In order to better understand the strengthening mechanisms at room temperature, analyses were carried out to study the effect of grain boundary strengthening and precipitate strengthening using the Hall-Petch equation.

The deformation behavior of this AFA alloy in both the as-received condition and after the TMTs was also studied at elevated temperatures from 600-800ºC. The flow stress of the TMT materials was evaluated at different strain rates from 1 x 10^{-5} to 1 x 10^{-2} s^{-1}, and the high temperature deformation mechanisms were studied.

We also investigated the effects of aging on the microstructures and mechanical properties of two recently-developed AFA stainless steels, DAFA26 and DAFA29, which are Fe-14Cr-32Ni-3Nb-3Al-2Ti-based alloys. Their compositions are given below in Table 1. DAFA26 has the same composition as DAFA29 minus the addition of carbon and boron.

Table 1: Nominal and Analyzed compositions of DAFA26 and DAFA29

	Wt. %	Fe	Cr	Mn	Ni	Cu	Al	Si	Nb	V	Ti	Mo	W	Zr	C	B	P	S	O	N
DAFA26	Nominal	45.55	14.		32		3	0.15	3		2			0.3						
	Analyzed	45.29	14.00		32.47		2.95	0.13	2.93		1.97		0.01	0.29	0.002	<0.0003	<0.002	<0.0001	0.0012	0.0004
DAFA29	Nominal	45.44	14		32		3	0.15	3		2			0.3	0.1	0.01				
	Analyzed	45.3415	13.83	0.13	32	0.12	3.02	0.15	2.87	<0.01	2	0.1	<0.01	0.32	0.11	0.0085	<0.005			<0.0001

We also explored the effects of aging time on the microstructures of the alloys, specifically on the precipitation of Fe_2Nb Laves phase and B2-NiAl on the grain boundaries and of $L1_2$ in the f.c.c. matrix in an attempt to further improve the mechanical properties of AFA stainless steels. The effects of boron and carbon additions on the microstructures and various precipitates were studied.

The DAFA29 specimens after creep failure were also analyzed using optical microscopy, a SEM, and TEM. The fracture surfaces and deformed cross-sectional surfaces were characterized using the SEM. The mechanisms for creep failure were analyzed and discussed.

2.2 Significant Results

2.2.1 As-Received Microstructure

The as-received microstructure was characterized using a SEM, a TEM and XRD. Figure 1 shows a SEM analysis of the as-cast DAFA 26 alloy. In Figure 1a) the backscattered electron (BSE) image of the alloy surface shows the presence of precipitates in the matrix. Energy-dispersive X-ray spectroscopy (EDS) analysis in b) and c), revealed that these white precipitates were Niobium-rich compared with the matrix. These precipitates are most likely the niobium-rich Fe_2Nb-type Laves phase that is commonly found in AFA type alloys.

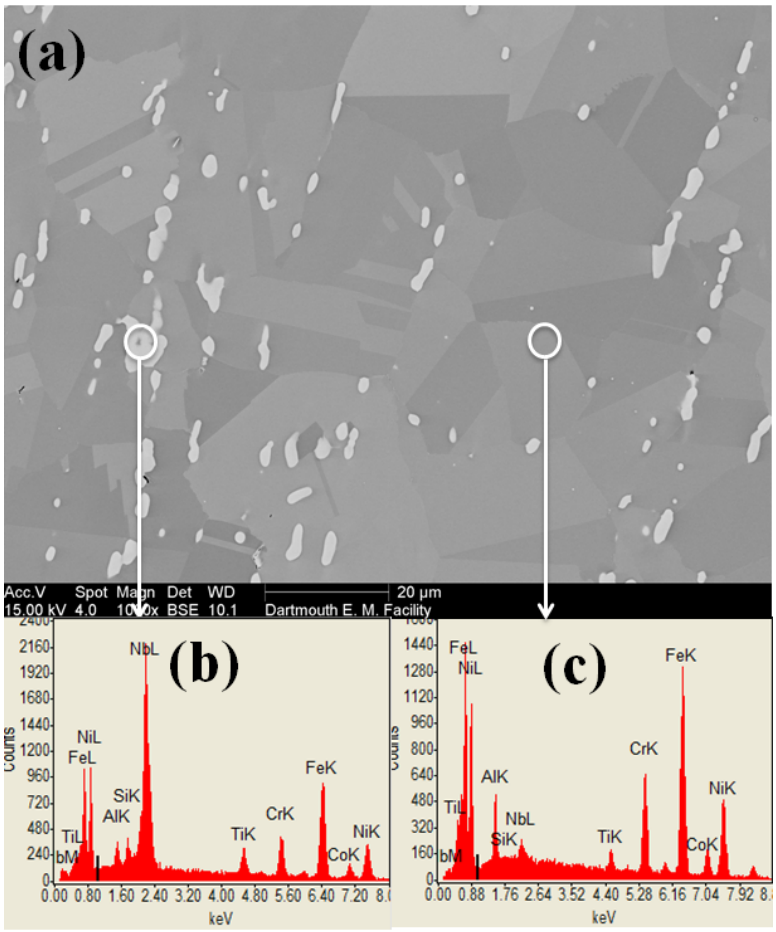

Figure 1: (a) BSE image of hot-rolled DAFA 26, and EDS of (b) Nb-rich precipitates, and (c) the matrix.

Figure 2 a) shows a selected area diffraction (SAD) pattern of the fcc matrix. The diffraction pattern consists of two sets of different diffraction spots. They are identified as being a superimposition of diffraction patterns from $L1_2$-Ni_3Al and austenitic fcc phases. The smaller diffraction spots are from $L1_2$-Ni_3Al, while the larger spots are from both $L1_2$-Ni_3Al and austenitic f.c.c. phases. Figure 2 b) shows the diffraction simulation of $L1_2$-Ni_3Al and austenitic fcc phases using the program CrystalMaker. The orientation relationship of $L1_2$-Ni_3Al and iron fcc phases is $[001]\gamma'//[001]\gamma$. The simulated diffraction pattern is a good match for the experimental SAD pattern.

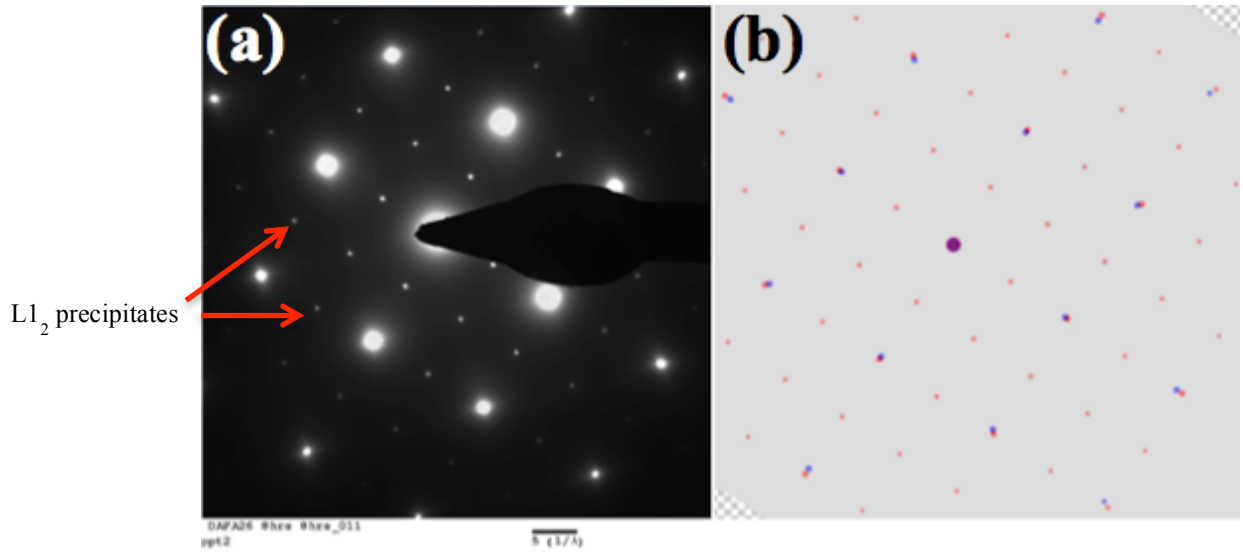

Figure 2: a) SAD pattern of fcc matrix along [001] showing superlattice reflections from $L1_2$ γ' precipitates in DAFA 26, b) corresponding simulated SAD pattern.

Figure 3 a) shows a precipitate in DAFA 26 located on the edge of a thin TEM foil. Figure 3 b) shows the corresponding convergent beam electron diffraction (CBED) pattern of the precipitate with a characteristic hexagonal pattern from [0001]. From this result and the EDS results, such as those shown in Figure 1, we concluded that these precipitates have a Laves phase Fe_2Nb structure. A schematic view of the Laves phase crystal structure of Fe_2Nb is shown in Figure 4.

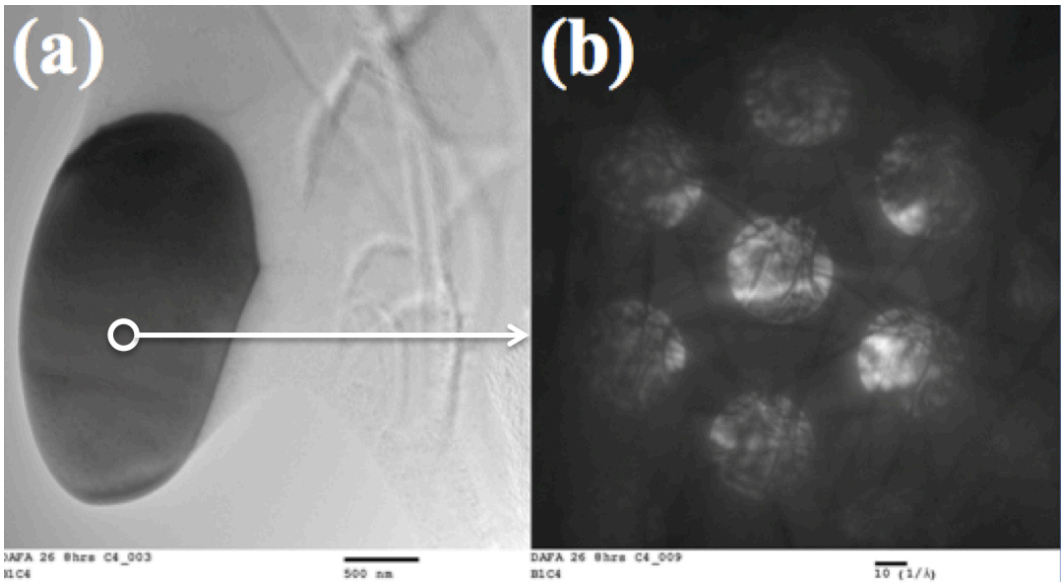

Figure 3: a) Bright field TEM image of precipitate in the matrix of DAFA26, b) CBED pattern of C14 hexagonal Fe_2Nb Lave phase precipitate.

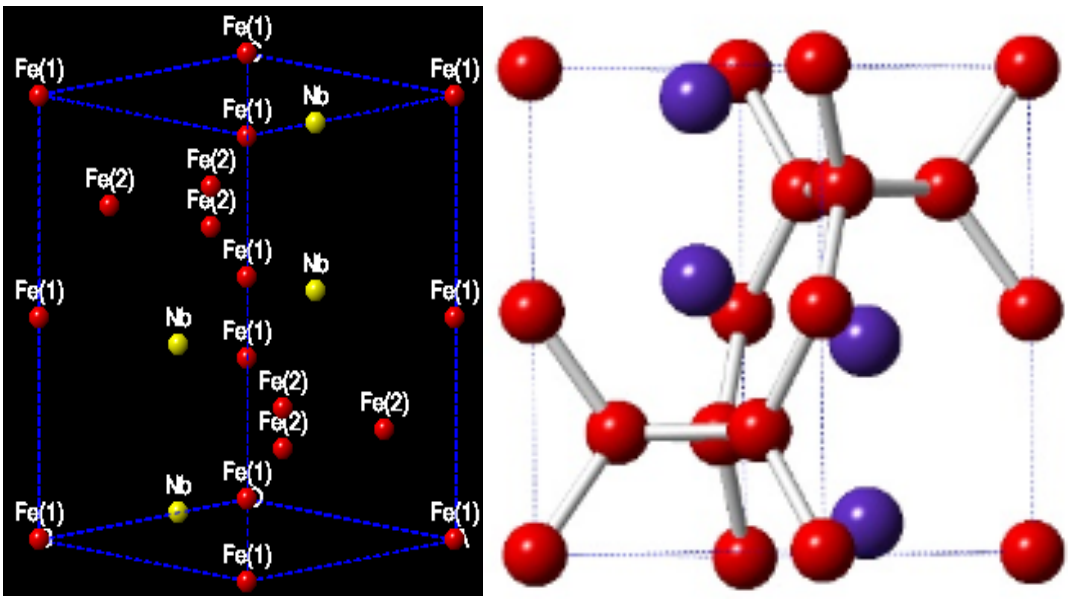

Figure 4: Schematic of C14 Laves phase Fe_2Nb.

2.2.2 Mechanical Properties of the As-Received Material

Two different sets of tensile samples were prepared from DAFA29: one along the rolling direction, and the other perpendicular to the rolling direction. Figure 5 shows the tensile test results for hot-rolled DAFA29 with specimens taken from the two orientations. For the samples parallel to the rolling direction, the yield strength and elongation to failure were 560 MPa and 22 %, respectively. For the specimens cut perpendicular to rolling direction, the yield strength was significantly lower at 360 MPa but the elongation was greater at 37 %.

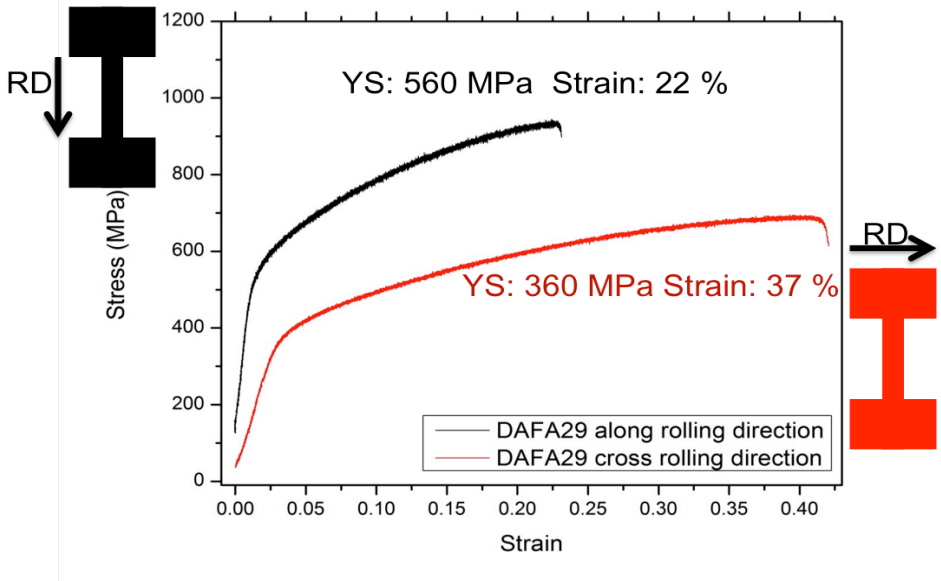

Figure 5: Tensile tests results for as-hot-rolled DAFA 29 for specimens cut parallel and perpendicular to the rolling direction.

Figure 6 is a comparison of the fracture surfaces of DAFA29 for the tensile specimens from the two different directions. For both samples, the fracture surfaces consist of many microvoids and dimples. The Laves phase precipitates are located in the center of these dimples, indicating that the Laves phase precipitates act as void initiators. The microvoids grow from them and coalesce when the applied stress increases. The microvoids then coalesce to form cracks. The cracks then rapidly propagate and result in fracture. Comparing Figures 6a and 6c, the sample perpendicular to the hot rolling direction has larger dimples. This is in agreement with the tensile test results as shown in Figure 5, where this specimen shows a greater elongation to failure. Figures 6b and 6d show high magnification images of the fracture surfaces. Many of the Laves phase precipitates in the samples along the hot rolling direction appear to be fractured, the fractured precipitates aiding the microvoid formation. For the samples perpendicular to the hot rolling direction, the Laves phase precipitates appeared to be elongated and less fractured.

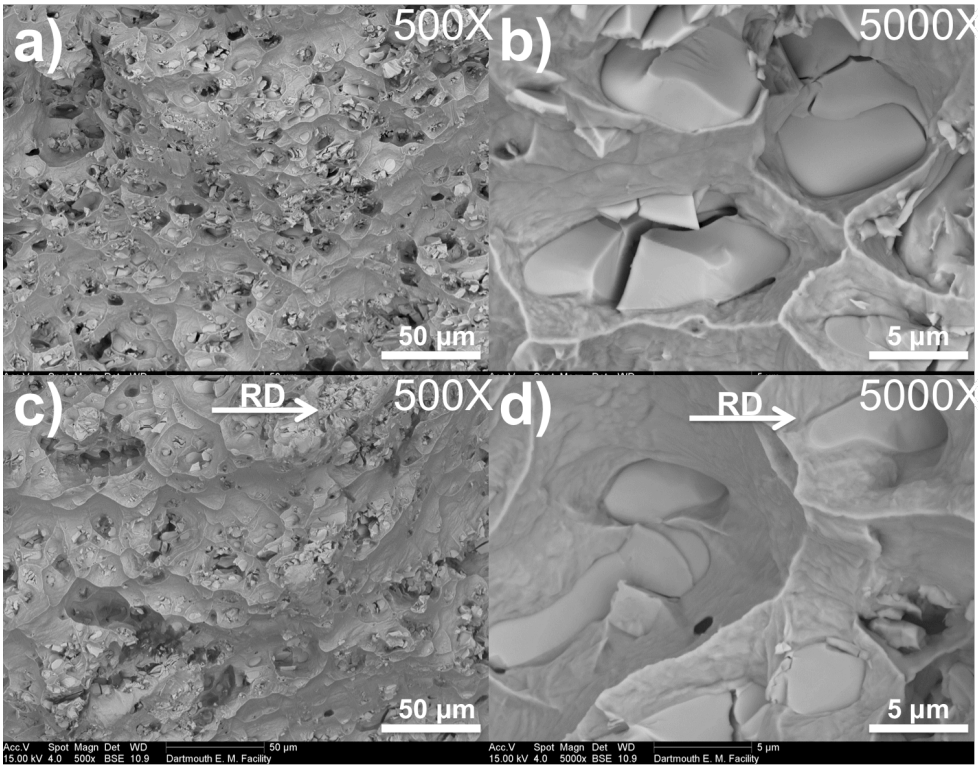

Figure 6: Secondary electron images comparing the fracture surfaces of DAFA29 specimens tested (a, c) parallel and (b, d) perpendicular to the rolling direction

Figure 7 shows the polished sidewalls surfaces of the two sets of tensile samples. Both of the samples show cracks in the Laves phase precipitates. Those cracks are presumably generated from the stress concentration on the surface of precipitates when dislocations moving in the matrix are arrested at the brittle Laves phase.

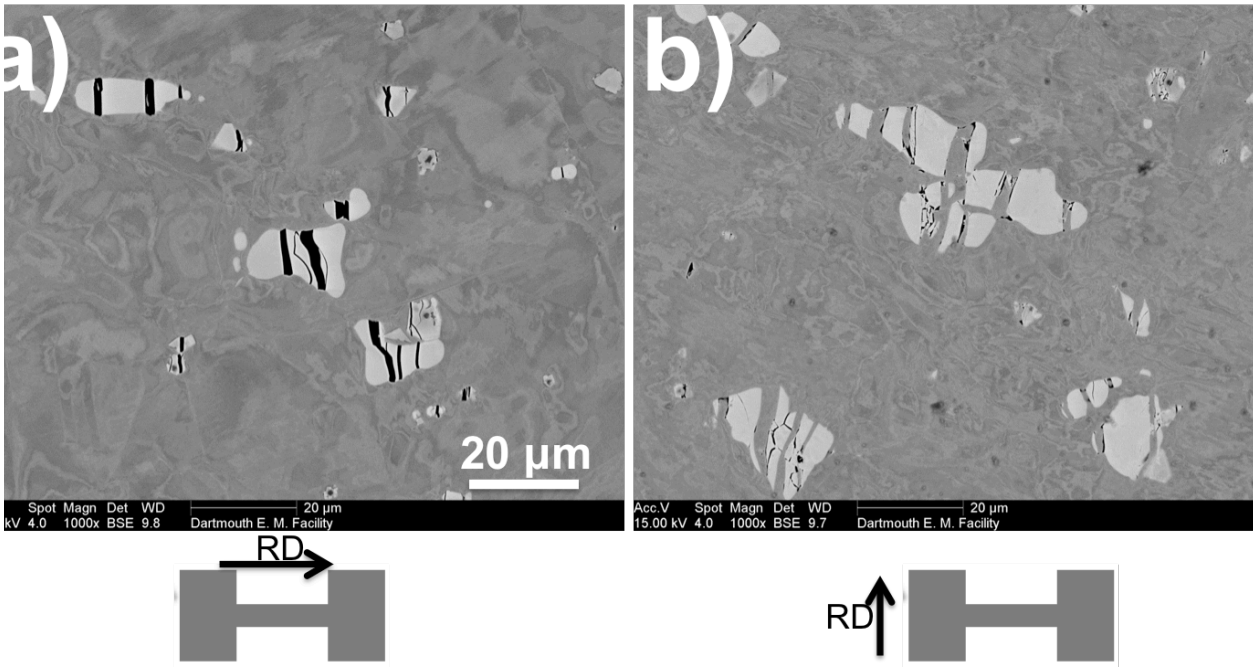

Figure 7: Backscattered electron images of the polished sidewall surfaces of the tensile samples tested (a) parallel and (b) perpendicular to the rolling direction.

2.2.3 Thermomechanical Treatments

Two TMTs of the DAFA29 were performed in an attempt to produce finer and uniformly distributed precipitates, as shown in Figure 8. In the first approach (referred to as Method #1), the DAFA29 was cold rolled to a 90 % reduction in thickness with a ~4.5 % reduction per pass, and then annealed at 800ºC for 2.4, 24, or 240 h. In the second approach (referred to as Method #2), the alloy is given a solutionizing anneal at 1200ºC and then cold rolled to a 90 % reduction in thickness with a ~4.5 % reduction per pass before annealing at 800ºC for 2.4, 24, or 240 h.

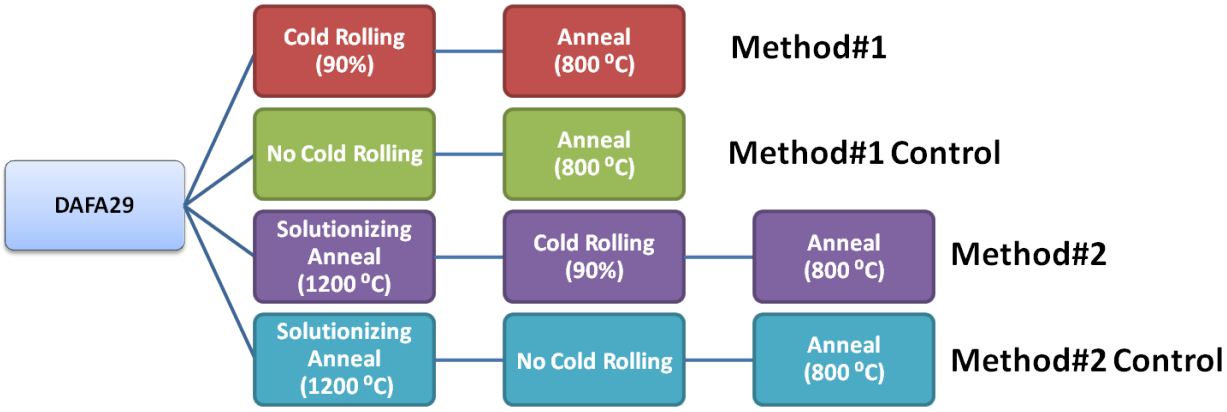

Figure 8: Flowchart of the two thermo-mechanical treatment methods and the control methods used on DAFA 29.

Previous research has reported that cold rolling (with 10 % thickness reduction) of precipitate-strengthened austenitic stainless steels could improve creep properties, because the dislocations introduced by cold rolling acted as nucleation sites for fine MC (NbC) carbide precipitates, resulting in enhanced creep resistance [1-3]. It should be noted that the alloy examined here (DAFA29) can be cold rolled to more than 90 % thickness reduction, indicating that the coarse second phase precipitates do not degrade room temperature workability of the AFA alloys, similar to the results previously reported in [4].

BSE images of DAFA29 after thermo-mechanical treatment Method #1 are shown in Figure 9. The steel was cold rolled to a 90 % reduction in thickness, after which it is evident that the large Laves phase precipitates had fractured (Figure 9b inset). These samples were then annealed at 800°C for 2.4 h (Figure 9c), 24 h (Figure 9d), or 240 h (Figure 9e). The cold rolling fractured many of the Laves phase precipitates in the matrix resulting in smaller precipitates (Figure 9c, d and e).

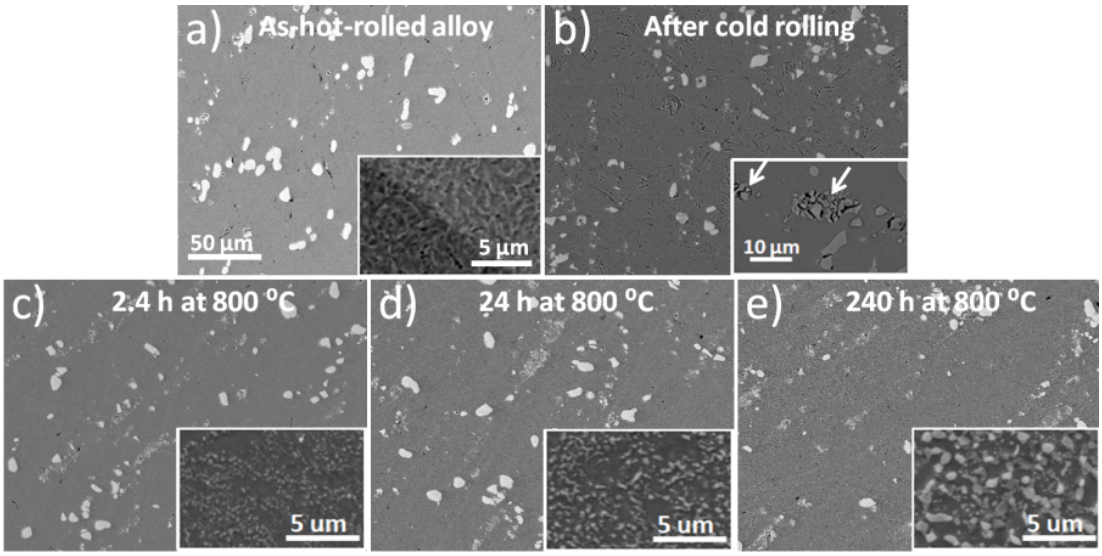

Figure 9: BSE images of DAFA29 showing fracturing of the Laves phase after cold rolling: (a) as-received, (b) after cold rolling (90 % thickness reduction), and after annealing at 800ºC for (c) 2.4 h, (d) 24 h, or (e) 240 h.

BSE images of DAFA 29 after thermo-mechanical treatment Method #2 are shown in Figure 10. The aim of using this method is to solutionize the large Laves phase precipitates before cold rolling. Unfortunately, the large Laves phase precipitates could not be completely solutionized at 1200 ºC, although the solutionizing anneal significantly reduced their volume fraction from 4 % to 2 % (compare Figures 10a and b). The solutionizing anneal also produced a substantial increase in the average grain size from 40 to 250 µm (all grain sizes were measured using the linear line intercept method). As observed for thermo-mechanical treatment Method #1, the residual large Laves phase precipitates also fractured during the cold rolling. Upon subsequent annealing, the size of the residual Laves phase precipitates did not change significantly. After the 240 h anneal, fine-scale particles precipitated out and were evenly distributed in the matrix (Figure 10f). These new precipitates presumably nucleated on the dislocations generated during

the 90 % cold rolling. The inset in Figure 10f clearly shows precipitates with two different types of brighter contrast, white and light gray, likely due to the presence of two different phase compositions. The light gray phase is likely the Laves phase and the dark gray phase is likely B2 NiAl. These small precipitates were also observed in previous research on AFA alloys [3, 5].

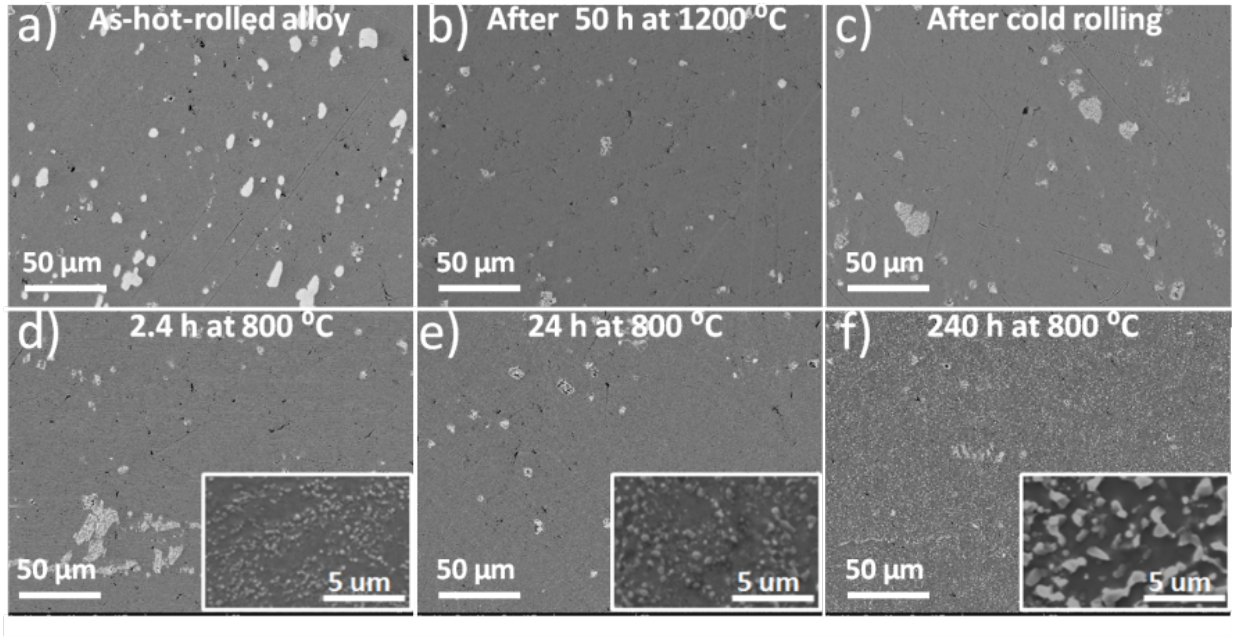

Figure 10: BSE images of DAFA29: (a) as-received, (b) after a solutionizing anneal of 50 h at 1200ºC, (c) after a subsequent 90 % cold rolling reduction, and after solutionizing, cold rolling, and annealing at 800ºC for (d) 2.4 h, (e) 24 h, or (f) 240 h.

Table 2 shows the average size of the Laves phase precipitates after both thermo-mechanical treatments using the particle size image analysis technique used by Trotter et al. [6]. The sizes of the Laves phase precipitates are in the range 167-562 nm, i.e.: much smaller than the large Laves phase precipitates in Figures 1 and 3 which are 0.5-10 µm. As the annealing times increases from 2.4 h to 240 h, the size of Laves phase increases from 167 nm to 417 nm for the samples treated by Method#1. The size of Laves phase in materials treated with Method#2 is slightly larger than those treated by Method#1 for all annealing times. This is due to the extra step of solutionizing in Method#2.

Table 2: Average size of Laves phase particles inside of thermo-mechanical treated DAFA29.

	Average size (nm)	
Annealing time (h)	**Method#1**	**Method#2**
2.4	167 ± 37	175 ± 45
24	237± 64	244 ±65
240	417 ± 165	562 ± 173

Comparing Figures 9 and 10, the BSE images of the samples after solutionizing anneal show fewer Laves phase precipitates. This is especially clear in Figure 10f, where the large Laves phase precipitates are barely observed. Instead, the small precipitates are uniformly distributed in the matrix. The solutionizing annealing used in Method #2 is an effective way to reduce the size and redistribute the Laves phase precipitates, resulting in a finer and denser distribution. Most of the small Laves phase precipitates appeared to be coupled with B2 NiAl precipitates. Figure 11 shows a BSE image of the precipitates. Based on EDS results, the brighter contrast precipitates are either Laves phase or MC carbides and the darker contrast precipitates are B2 NiAl precipitates. The B2 NiAl normally co-precipitates with the Laves phase during the thermo-mechanical treatment process. Such finer and denser distributed Laves phase and B2 NiAl precipitates (size are less than 1 μm) may be effective in further increasing the creep strength.

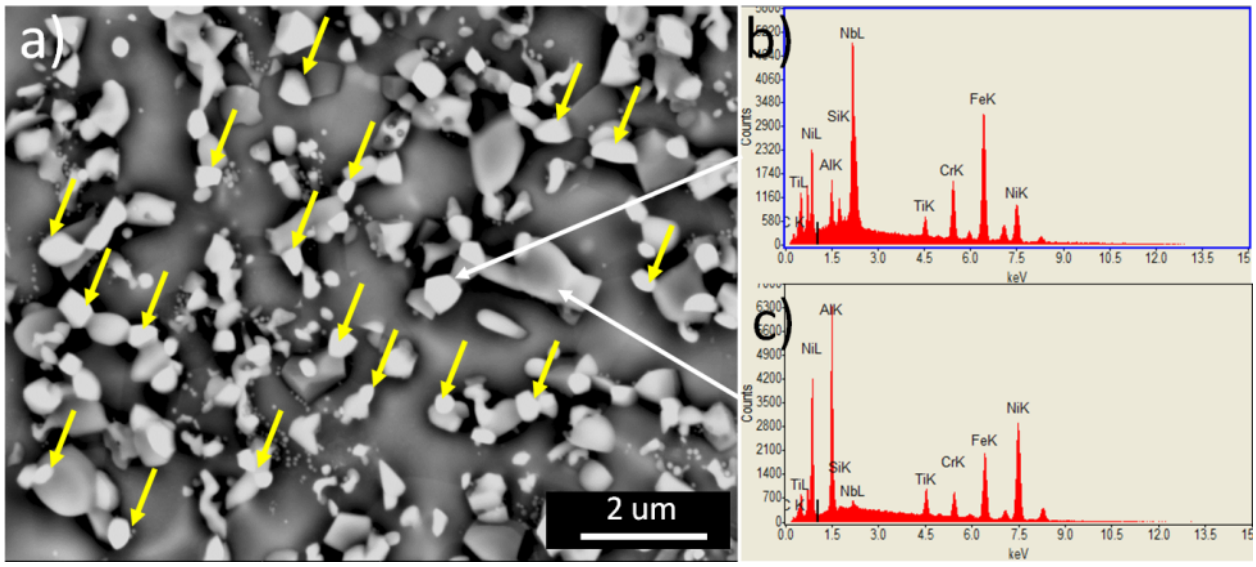

Figure 11: a) BSE image of DAFA29 after solutionizing annealing 50 h at 1200ºC, cold rolling (90 %) and further annealing at 800ºC for 240 h; b) and c) are the EDS results from the Laves phase and NiAl precipitates (yellow arrows indicate the Laves phase co-precipitates)

Bright field (BF) TEM images and SAD patterns of DAFA 29 after cold rolling and annealing at 800ºC for 2.4, 24, or 240 h (Method #1) are shown in Figure 12. After the 2.4 h anneal many small grains with an average grain size of ~100 nm are present. The SAD pattern shows diffraction rings (Figure 12d), a feature characteristic of fine-scale f.c.c. grains having many different orientations. As the annealing time is increased from 2.4 to 240 h, the grain size increased from ~100 nm to ~1μm. The diffraction patterns changed accordingly as the number of grains captured within the SAD aperture decreased resulting in a single crystal diffraction pattern from a single grain.

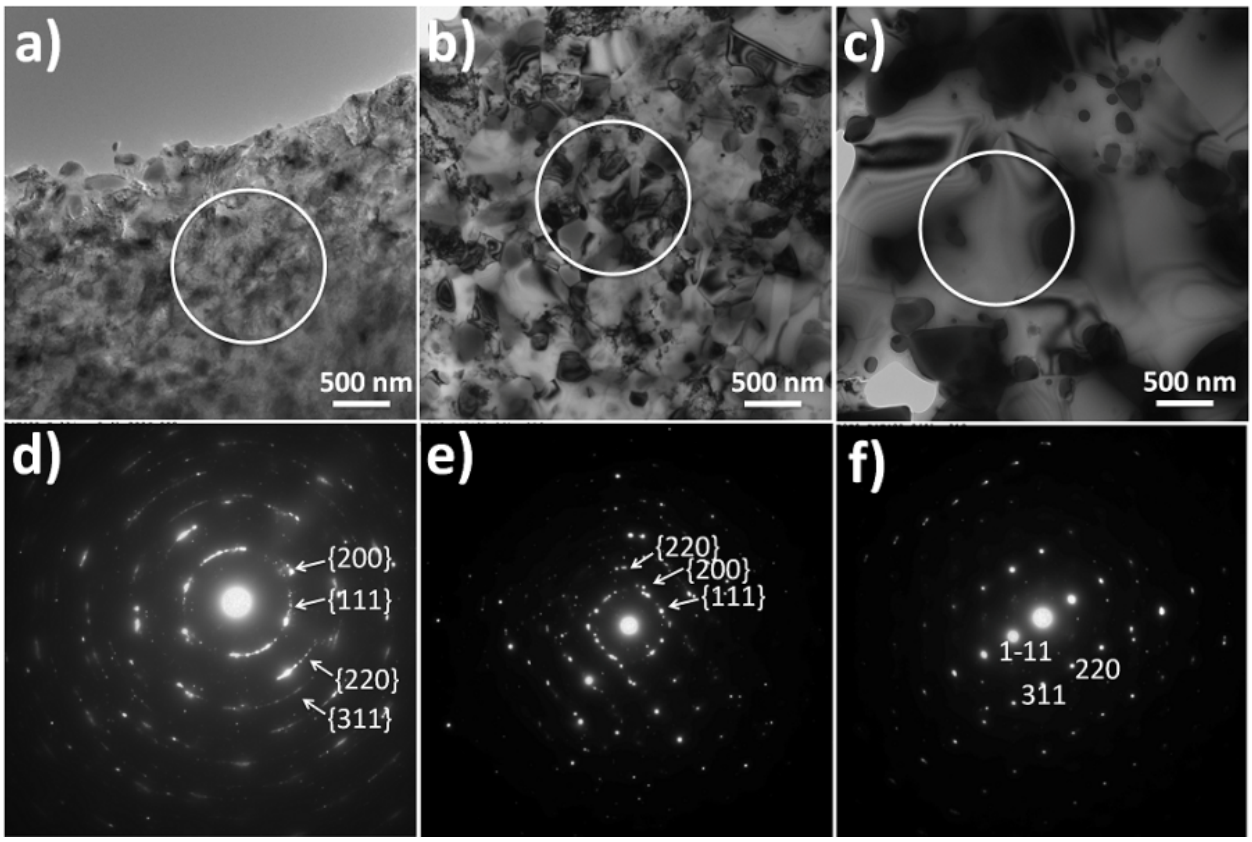

Figure 12: BF TEM images and SAD patterns of DAFA29 after cold rolling and annealing at 800ºC for (a, d) 2.4 h, (b, e) 24 h, or (c, f) 240 h (Method #1).

In conventional steels, elongated grains and/or aligned second-phase particles parallel to the rolling direction are developed after large strain cold rolling. For the AFA steels, no elongated grains are observed. Instead, a large number of irregular nanoscale grains are observed in the TEM images of the 90 % cold rolled material after 2.4 h annealing, indicating that all the grains are fully recrystallized after the 2.4 h annealing process.

BF TEM images and SAD patterns of DAFA29 after a solutionizing anneal at 1200ºC, cold rolling, and then annealing at 800ºC for 2.4, 24, or 240 h (Method #2) are shown in Figure 13. For the sample annealed for 2.4 h, many small grains are observed with an average grain size of ~200 nm with the SAD pattern exhibiting diffraction rings (Figure 13d). This is similar to 2.4 h samples after thermo-mechanical treatment Method #1, where fine grains (~200 nm) are produced by cold rolling and annealing for 2.4 h. As the annealing time increases from 2.4 to 240 h, the grain size increases from ~200 nm to ~2 μm.

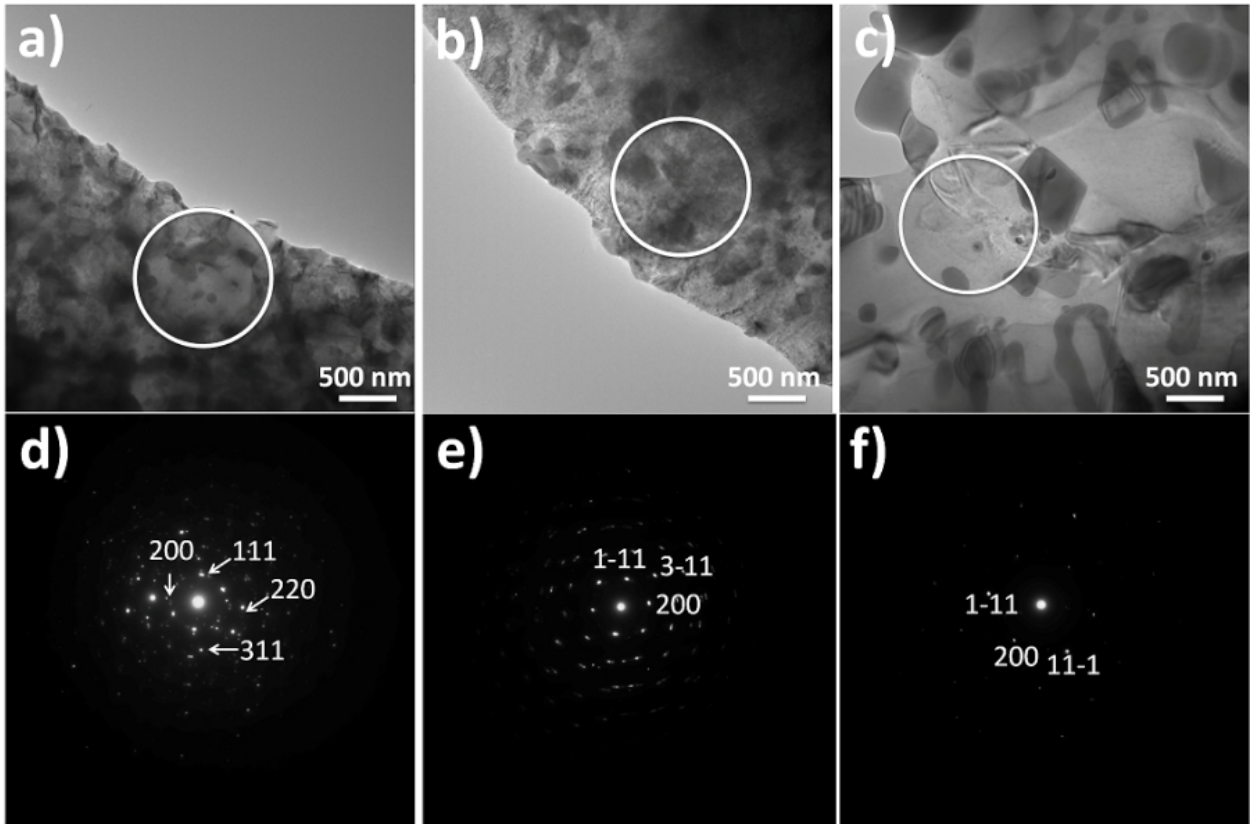

Figure 13: BF TEM images and SAD patterns of DAFA 29 after solutionizing, cold rolling, and annealing at 800ºC for (a, d) 2.4 h, (b, e) 24 h, or(c, f) 240 h (Method #2).

Comparing Figures 12 and 13, the average grain size produced by Method #2 is approximately twice that produced by Method #1, which is due to grain growth during the solutionizing anneal process. This annealing step increases the average grain size of DAFA29 from 40 to 250 μm.

After thermo-mechanical treatment, multiple second phase precipitates in treated DAFA29 were studied by TEM/EDS/CBED.

A BF TEM image and EDS spectrum from a Laves phase precipitate in DAFA29 after thermo-mechanical treatment Method #1 annealed for 240 h are shown in Figure 14. The Laves phase precipitates appear darker than the matrix in the TEM image due to their greater thickness and/or compositional difference (heavy element Nb), and, hence, greater absorption. The inset in Figure 14a shows a CBED pattern from the circled region. The diffraction pattern indicates a hexagonal crystal structure aligned at [0001] direction. EDS results from the same region of the Laves phase precipitate, Figure 14b, indicate that it is enriched in Nb and Fe. The EDS data shows an atomic ratio of Fe to Nb of approximately 2:1 consistent with Fe_2Nb precipitates although the precipitates also contain some other elements.

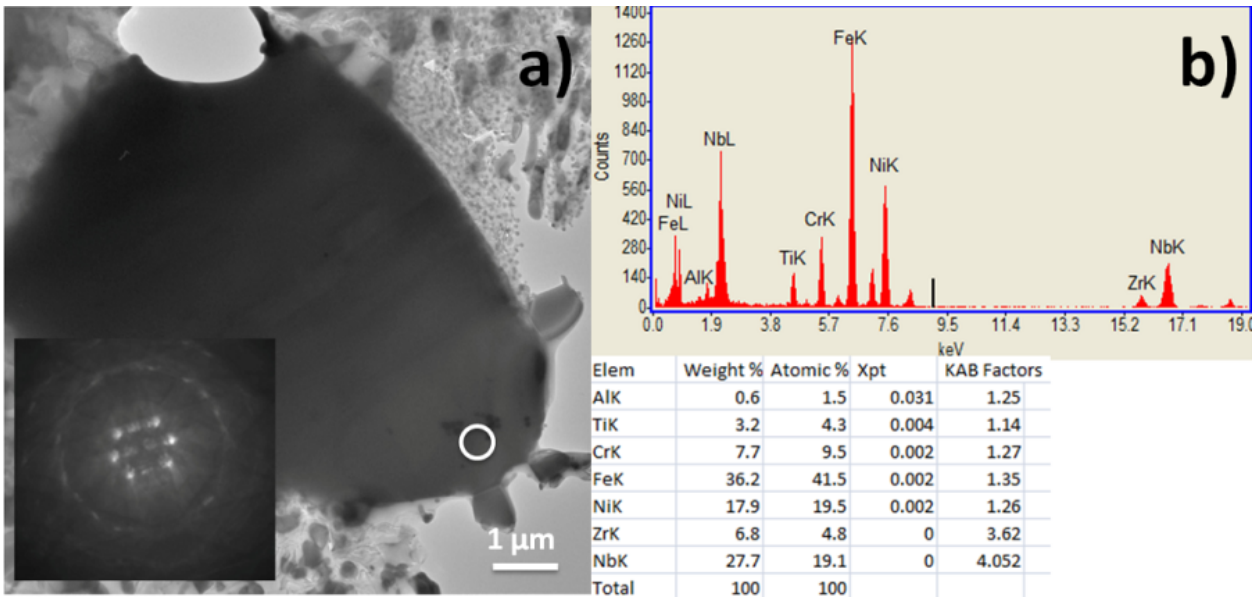

Elem	Weight %	Atomic %	Xpt	KAB Factors
AlK	0.6	1.5	0.031	1.25
TiK	3.2	4.3	0.004	1.14
CrK	7.7	9.5	0.002	1.27
FeK	36.2	41.5	0.002	1.35
NiK	17.9	19.5	0.002	1.26
ZrK	6.8	4.8	0	3.62
NbK	27.7	19.1	0	4.052
Total	100	100		

Figure 14: (a) BF TEM image, (b) EDS spectrum, and CBED pattern from a Fe2Nb Laves phase precipitate in DAFA29 after thermo-mechanical treatment Method #1, annealed 240 h. The EDS data and CBED pattern are from the region circled in the TEM image.

The creep resistance of the alloys strengthened by Fe_2Nb Laves phase particles alone was previously found to be relatively low at 750ºC and 100 MPa in air, which was attributed to the relatively coarse size of the Fe_2Nb precipitates [3]. Both large size and small size Fe_2Nb precipitates can be observed in DAFA29 after thermo-mechanical treatment Method #1, as shown in Figure 14. These newly formed small Laves phase precipitates (~1 µm) might be helpful to enhance the creep performance.

A BF TEM image and EDS results from a NiAl precipitate in DAFA29 after thermo-mechanical treatment Method #1 and annealed for 240 h are shown in Figure 15. The CBED pattern in the Figure 15a inset corresponds to a B2 structure viewed along the [211] zone axis. EDS analysis results from the circled region of the NiAl precipitate are shown in Figure 15b. Although the precipitates are mostly Ni and Al, they also contain other elements. The NiAl precipitates are observed after both thermo-mechanical treatments. They are not present in the as-received DAFA29. A previous study suggested this B2 phase is likely to increase the creep resistance by affecting dislocation climb in the f.c.c. matrix due to their resistance to dislocation cutting during creep deformation [4, 5].

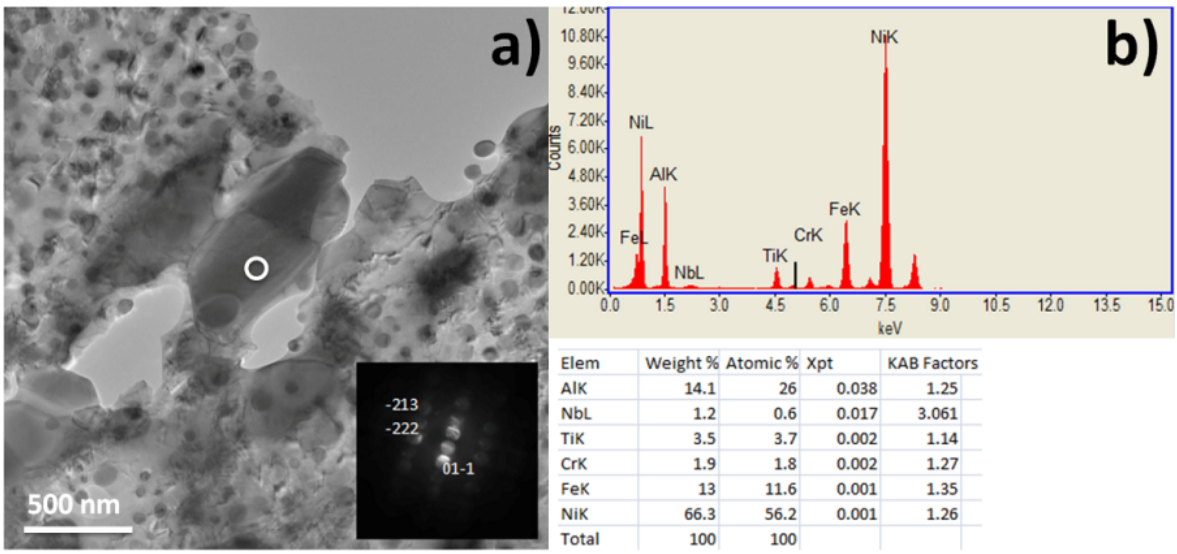

Elem	Weight %	Atomic %	Xpt	KAB Factors
AlK	14.1	26	0.038	1.25
NbL	1.2	0.6	0.017	3.061
TiK	3.5	3.7	0.002	1.14
CrK	1.9	1.8	0.002	1.27
FeK	13	11.6	0.001	1.35
NiK	66.3	56.2	0.001	1.26
Total	100	100		

Figure 15: (a) BF TEM image, (b) EDS spectrum, and CBED pattern for a NiAl precipitate in DAFA29 after thermo-mechanical treatment Method #1, annealed 240 h. The EDS data and CBED pattern are from the region circled in the TEM image.

A BF TEM image and EDS results from a Ni_3Al precipitate on the edge of a thin foil from DAFA29 after thermo-mechanical treatment Method #1 and annealed 240 h are shown in Figure 16. The Ni_3Al precipitates are spherical with a diameter less than 100 nm. The inset in Figure 16a shows a CBED pattern from the circled region of theNi_3Al precipitate. This corresponds to a pattern from an $L1_2$ structure viewed along the [212] zone axis. EDS data acquired from the region circled in TEM image of this precipitate is shown in Figure 16b. The atomic ratio of Ni to Al(Ti) is approximately 3:1, with small amounts of other elements present.

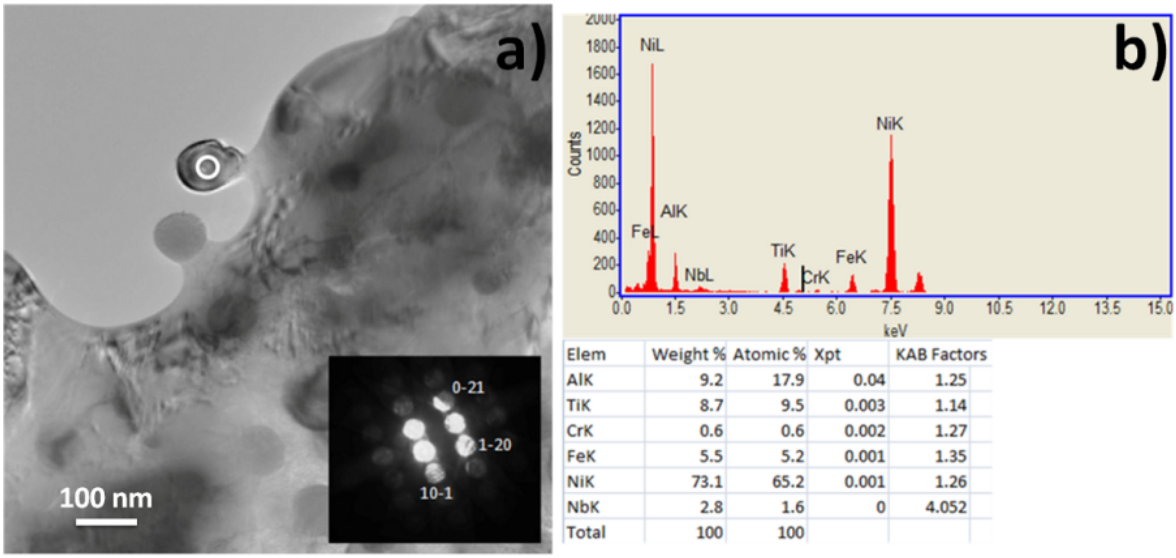

Elem	Weight %	Atomic %	Xpt	KAB Factors
AlK	9.2	17.9	0.04	1.25
TiK	8.7	9.5	0.003	1.14
CrK	0.6	0.6	0.002	1.27
FeK	5.5	5.2	0.001	1.35
NiK	73.1	65.2	0.001	1.26
NbK	2.8	1.6	0	4.052
Total	100	100		

Figure 16: (a) BF TEM image, (b) EDS spectrum, and CBED pattern from a Ni_3Al precipitate in DAFA29 after thermo-mechanical treatment Method #1, annealed for 240 h.

The average size of the $L1_2$ precipitates in this heat-treated alloy is ~84 nm, which is about eight times larger than in the as-received alloy. These $L1_2$ precipitates have a similar size to the Ni_3Al observed in the AFA alloy after creep tests of 3008 h at 750ºC and 100 MPa [7]. Besides the spherical $L1_2$ precipitates, no other nanoscale particles, such as carbides or borides, are observed after the thermo-mechanical treatments.

MC carbide (M: Nb, Ti) precipitates are observed in DAFA29 both before and after thermo-mechanical treatments. Figure 17 shows a secondary electron image of MC carbides in one thermo-mechanically treated DAFA29 sample. The upper inset in Figure 17b is an EBSD pattern, indicating that this is the [011] zone axis of a f.c.c. precipitate. Both the pattern and EDS results show this is an MC precipitate.

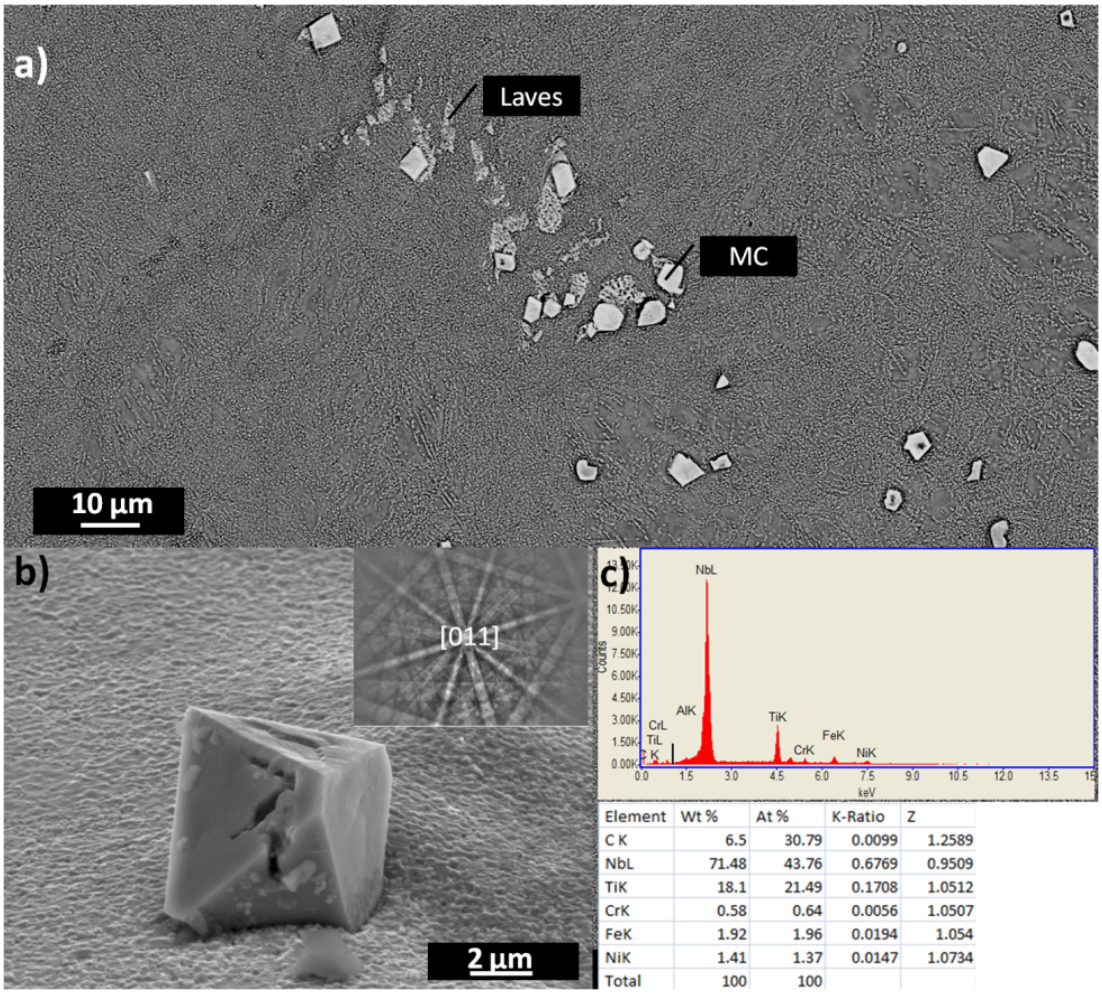

Element	Wt %	At %	K-Ratio	Z
C K	6.5	30.79	0.0099	1.2589
NbL	71.48	43.76	0.6769	0.9509
TiK	18.1	21.49	0.1708	1.0512
CrK	0.58	0.64	0.0056	1.0507
FeK	1.92	1.96	0.0194	1.054
NiK	1.41	1.37	0.0147	1.0734
Total	100	100		

Figure 17: (a) SEM image, (b) EBSD pattern, and (c) EDS spectrum from a MC carbide precipitate in DAFA29 after thermo-mechanical treatment Method #1, annealed 240 h

Since the lattice parameters of the f.c.c. matrix and $L1_2$ precipitates are similar, synchrotron XRD was used to determine their respective lattice parameters in the alloy. Synchrotron XRD results from the DAFA29 samples after a 1200ºC solutionizing anneal for 50 h, 90 % cold rolling, and then an 800ºC anneal for 240 h, are shown in Figure 18. The 240 h annealed samples were

selected for this measurement because the size of precipitates is larger due to particle coarsening, and hence, the XRD signal will be stronger than in the 24 or 2.4 h annealed samples. In the XRD pattern, the Miller indices of the f.c.c. peaks are labeled in blue, the $L1_2$ superlattice peaks are labeled in red, the Laves phase peaks are labeled in black, and B2 peaks are labeled in green.

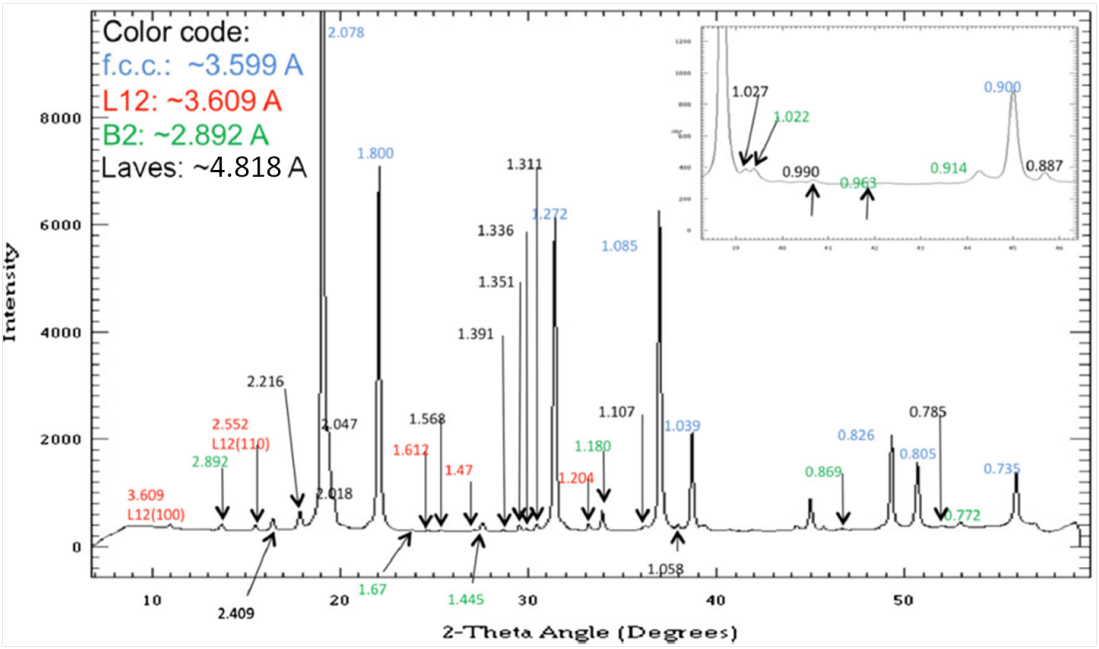

Figure 18: Synchrotron XRD results for DAFA29 after a 1200ºC solutionizing anneal for 50 h followed by 90 % cold roll and an 800ºC anneal for 240 h. The inset shows the region from ~38° to ~46° expanded.

The lattice parameters for each phase were calculated based on the highest angle peaks of each phase. The calculated lattice parameters for the phases in the 240 h annealed sample were: the $L1_2$ phase is equal to 3.609 Å, the f.c.c. matrix is equal to 3.599 Å, and the NiAl phase is equal to 2.892 Å. The lattice misfit between the $L1_2$ precipitates and the f.c.c. matrix was only 0.28 % after the 240 h heat treatment, indicating that very small elastic strain (~0.28 %) between the precipitates and the f.c.c. matrix is developed.

2.2.4 Room temperature tensile properties of thermomechanical treated AFA

The room temperature tensile test results for DAFA29 after the two different thermo-mechanical treatments are shown in Figure 19. The samples in Figure 19a were cold rolled and then annealed at 800ºC for different times. The yield strength and plastic strain to failure of as-received DAFA29 are 560 MPa and 22 %, respectively. The yield strength increased to 1280 MPa and the plastic strain decreased to 5.1 % after cold rolling and a 2.4 h anneal. The yield strength decreased with further annealing; the yield strength of the sample after a 24 h anneal was 1070 MPa, and was reduced to 800 MPa when the sample was annealed for 240 h. Surprisingly, the strain to failure for all the cold rolled and annealed samples did not change significantly as the annealing time increased and the yield strength decreased.

The samples shown in Figure 19b were treated with the additional step of a solutionizing anneal before cold rolling. Again, the yield strength increased to 1150 MPa and the plastic strain decreases to 6.2 % after this treatment followed by a 2.4 h anneal. The yield strength decreased to 1020 MPa for an increase in the annealing time to 24 h, and was further reduced to 750 MPa after an anneal for 240 h. Again, the strain to failure for the samples treated by this method did not change significantly after cold rolling and different annealing times.

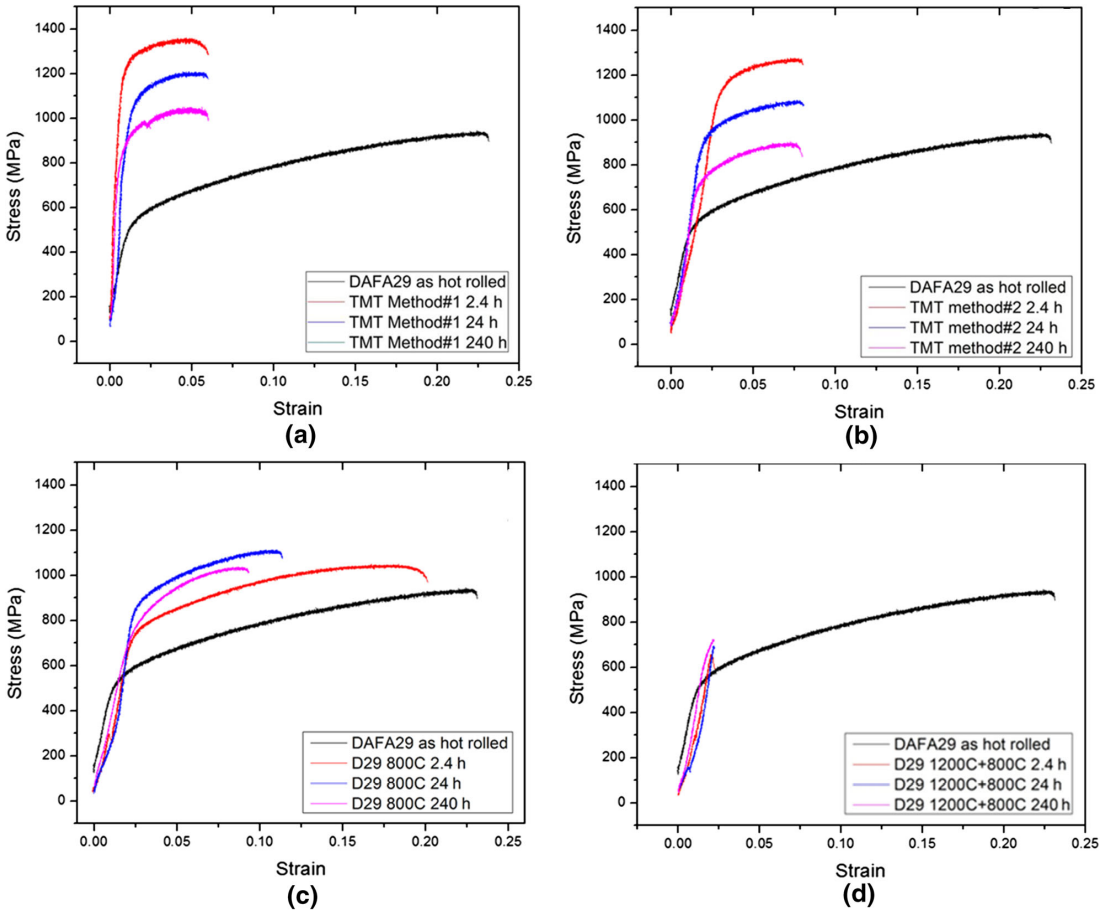

Figure 19: Tensile test results for DAFA29 after the two different thermo-mechanical treatments. (a) Samples are treated under Method #1 compared to as-hot-rolled DAFA29, (b) Samples are treated under Method #2 compared to as-hot-rolled DAFA29, (c) Samples are treated under Method #1 without cold rolling, and (d) two step annealed samples without cold rolling compared to as-hot-rolled DAFA29

The room temperature yield strengths of these treated DAFA29 specimens are four times higher than previous solution heat treated AFA alloys and twice that of the aged AFA alloys studied in [4]. This difference is mainly due to the nm-scale or μm-scale grains generated after either thermo-mechanical treatment. Comparing Figures 19a and 19b reveals that the solutionizing anneal is not effective in enhancing the tensile strength of DAFA29, although it is helpful to reduce the size of Laves phase and produce a finer and denser distribution of the Laves phase precipitates.

The tensile test results of the DAFA29 control samples after thermal treatment (Method #1 without cold work) are shown in Figure 19c. Simply, the control samples are annealed at 800ºC for different periods without any cold work. The yield strength increased to 747 MPa from 560 MPa and the plastic strain decreased slightly to 20 % after a 2.4 h anneal. The yield strength further increased to 890 MPa and the plastic strain decreased to 10 % after a 24 h anneal. For a 240 h annealing time, the yield strength decreased to 760 MPa, while the plastic strain still continued to decrease to 8 %.

For comparison, the tensile test results for DAFA29 control samples after using the thermal treatment (Method #2 without cold work) are shown in Figure 19d. Basically, the control samples undergo a solutionizing anneal at 1200ºC followed by an anneal at 800ºC for different periods without any cold work. The results show that all the samples after this two-step annealing are brittle and exhibit no plastic strain. The yield strength is slightly higher than that of the as-hot-rolled DAFA29 of 560 MPa.

In order to better understand the correlation between the grain size and the room temperature mechanical properties obtained, the Hall-Petch relation for all treated DAFA29 alloys was determined and is shown in Figure 20. The yield strength of the thermo-mechanically treated steel obeys a Hall-Petch relationship between the yield strength $\sigma_{0.2}$ and the grain size D, i.e.: $\sigma_{0.2} = \sigma_0 + KD^{-0.5}$, where $\sigma_0 = 558$ MPa and $K = 254$ MPa•μm$^{-0.5}$ for the Method#1 alloys and $\sigma_0 = 535$ MPa and $K = 284$ MPa•μm$^{-0.5}$ for the Method#2 alloys, according to the linear fit to $\sigma_{0.2}$ versus $D^{-0.5}$. The value of σ_0 differs considerably from that obtained in a 63 % cold rolled AISI 301 austenitic stainless steel [8] of 252 MPa (the values of K was 270 MPa•μm$^{-0.5}$, similar to this work). That the Method#1 alloys show a slightly higher off-set stress σ_0 than the Method#2 alloys is presumably due to the different precipitate size in these two alloys.

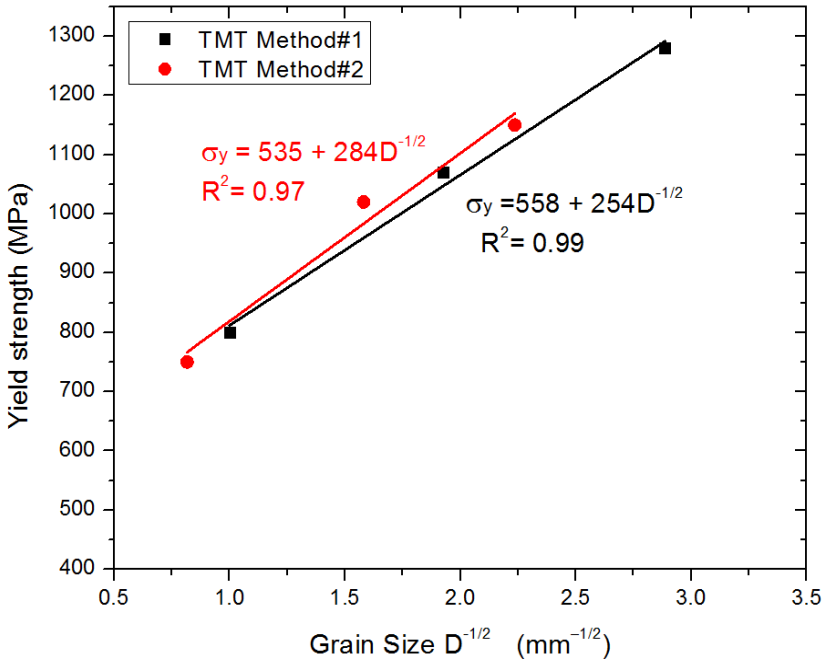

Figure 20: A plot of Hall-Petch relationship for DAFA29 after the two different thermo-mechanical treatments.

The stress σ_0 can be described, in general, as the sum of several strengthening mechanisms: 1) precipitate strengthening (σ_{ppt}), 2) strain hardening (σ_d), and 3) solid solution strengthening (σ_{ss}). The off-set stress can be expressed as

$$\sigma_0 = \sigma_{ppt} + \sigma_d + \sigma_{ss}$$

The large σ_0 observed in the current work likely arises from substantial precipitate strengthening from the finely-spaced $L1_2$-Ni_3Al precipitates. The estimated σ_{ppt} is ~289 MPa from the following equation (based on the Orowan looping mechanism) in [9].

$$\sigma_{ppt} = 0.84 \cdot \left(\frac{1.2 \cdot G \cdot b}{2 \cdot \pi \cdot L}\right) \cdot \ln\left(\frac{d}{2b}\right)$$

where G is the shear modulus (MPa), b is the burgers vector (nm), d is the particle diameter (nm), and L is the particle spacing (nm). For this calculation, a shear modulus of 80,000 MPa and a burgers vector of 0.25 nm were used. The particle diameter used for the calculation is 84 nm. This equation 3 can, thus, be written:

$$\sigma_{ppt} = \left(\frac{10.8 \cdot f^{1/2}}{d}\right) \cdot \ln\left(\frac{d}{2b}\right)$$

where f is the precipitate volume fraction and 10.8 is in the unit of MPa·nm. The volume percent of $L1_2$ Ni_3Al precipitates is 21 % [7]. According this calculation, the precipitate strengthening σ_{ppt} contributes almost half of the value of the off-set stress σ_0. Note the value of σ_{ppt} is variable and depends on the precipitates size and dislocation-precipitate interaction mechanism.

BSE images of the cross-sections of the strained microstructure for DAFA29 after treatment with Method#1, Method#2, Method#1 without cold rolling, and Method#2 without cold rolling are shown in Figures 21a-d, respectively. Figures 21e-h are the corresponding BSE images of the fracture surface of those four samples. In the sample treated with Method#1 the large Laves phase fractured perpendicular to the applied stress direction (Figure 21a). The fracture surface shows small dimples with Laves and/or B2 phase in the dimple center (Figure 21e). Large Laves phase and MC carbide are also observed on fracture surface in this sample. In the sample treated with Method#2 (Figure 21b and f), the fracture surface shows small dimples similar to Figure 21e with size of 1 to 2 μm. In the sample treated with Method#1 without cold rolling (Figure 21c and g), grain boundary precipitates are generated after annealing for 240 h. Larger cracks are observed along the grain boundaries. The fracture surface indicates that failures occur both on grain boundaries and in the matrix. Both fine grain boundary precipitates and large dimples are observed. For the sample treated with Method#2 without cold rolling (Figure 21d and h), Laves phase precipitates (exhibiting bright contrast) are present on the grain boundaries and triple junctions (Figure 21d). In some triple junctions, a eutectic structure is observed. These local eutectic structures suggest possible occasional, local melting of the alloy during the 1200ºC solutionizing treatment. The fracture surface of the materials after the 240 h anneal, shown in Figure 21h, show intergranular fracture. This fracture mode of the material is different from the others since the grain boundaries were fully covered by Laves phase and NiAl precipitates. The elongation of this sample is less than 1 % as shown in Figure 19d.

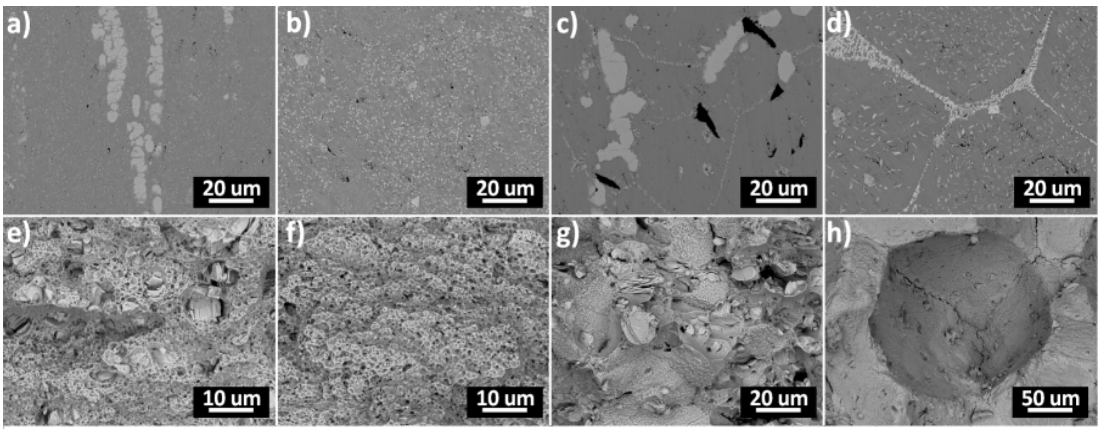

Figure 21: BSE images of the polished cross section and fracture surfaces of DAFA29 after different thermo-mechanical treatments. a) Method #1 for 240 h, b) Method #2 for 240 h, c) Method #1 without cold rolling, d) Method #2 without cold rolling; e), f), g), and h) are the fracture surface for the samples shown in a), b), c), and d).

2.2.5 High Temperature Tensile Properties of Thermomechanical Treated AFA

Tensile tests of TMT Method#1 alloys were performed at 700ºC. The stress strain curves of the three TMT alloys are shown in Figure 22a. All three TMT alloys show lower yield strength but higher elongation compared to the as-received DAFA29, see Table 3. The tensile behaviors of these TMT alloys at 700ºC are significantly different from room temperature. They show yield strength above 1000 MPa in room temperature tensile tests.

Tensile tests of TMT alloys Method#2 were also carried out at 700ºC. The stress strain curves of the three TMT alloys are shown in Figure 22b. The results are similar to the stress strain curves observed for the TMT Method#1 tests. All the TMT alloys show lower yield strength, but higher elongation. The yield strengths (measured as 0.2% proof stress) were in the range of 270-346 MPa, see Table 3.

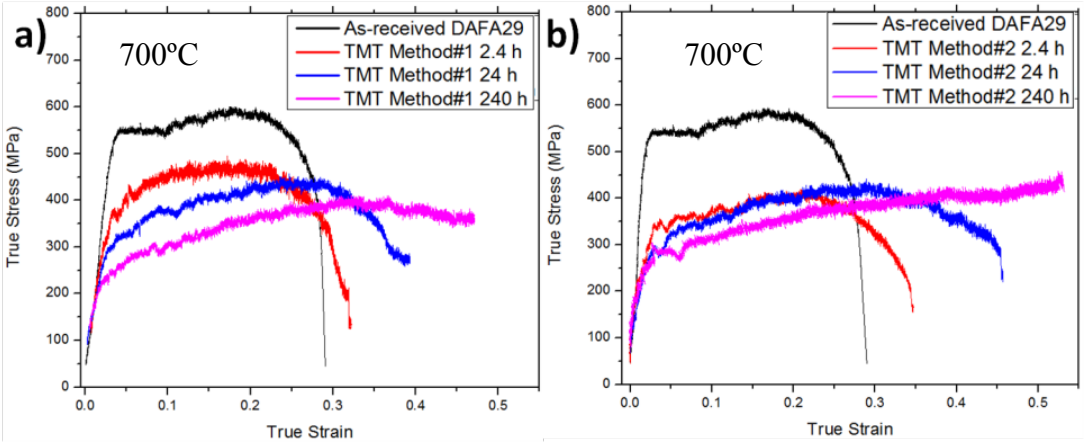

Figure 22: Stress strain curves of as-received and TMT DAFA29 at 700ºC, a) after TMT Method#1, b) after TMT Method#2.

Table 3: Yield strength, elongation at fracture and reduction in area at the neck for the as-received and TMT DAFA29 after tensile tested at 700°C

	TMT Method#1			TMT Method#2		
Materials	**Yield Strength (MPa)**	**Elongation (%)**	**Reduction in area (%)**	**Yield Strength (MPa)**	**Elongation (%)**	**Reduction in area (%)**
DAFA29	523	28	30	523	28	30
TMT 2.4h	393	32	33	346	33	49
TMT 24h	298	38	64	298	45	67
TMT 240h	225	46	93	270	53	91

After the tensile tests at 700ºC, all test specimens were characterized using the SEM. All the treated samples have different shapes of the necked region because of differences in ductility. TMT (Method#1) alloys after ageing for 2.4 h, 24 h and 240 h showed reductions in area of 33%, 64%, and 93%, respectively. The differences in the reduction in area are due to the different grain sizes for these three treated samples. The grain sizes of TMT (Method#1) annealed for 2.4 h, 24 h and 240 h samples are ~100 nm, ~270 nm, and ~1 μm, respectively. Thus, the elongation and reduction in area increased with increasing grain size, presumably due to the reduction in yield strength.

For TMT alloys treated using Method#2, the reductions in area for the 2.4 h, 24 h and 240 h samples were 49%, 67% and 91%, respectively. The grain size of TMT samples with ageing of 2.4 h, 24 h and 240 h are ~200 nm, ~450 nm, and ~2 μm, respectively. The 240 h annealed TMT alloy also has the largest area reduction and the highest elongation up to 53 % due to the fast grain growth to larger than 2 μm during 800ºC annealing.

Figure 23 shows fracture surfaces of as-received DAFA29, TMT 2.4 h, 24 h and 240 h samples after tensile testing at 700ºC. The fracture surface of as-received DAFA29 shows ductile failure with large ductile dimples and considerable plastic deformation between the dimples. The fracture surfaces of TMT alloys are covered with a thick layer of oxide due to exposure at high temperature during the tensile tests. However, the Laves phase precipitates, which show white contrast, are still visible. There are no dimples evident on the fracture surface for all three TMT alloys, although the materials are all much more ductile than as-received DAFA29. This ductility is due to the small grain sizes (ranging from ~100 nm to 1 μm) of these three TMT samples. All three fracture surfaces are coved by a layer of oxide formed during tensile test at 700ºC

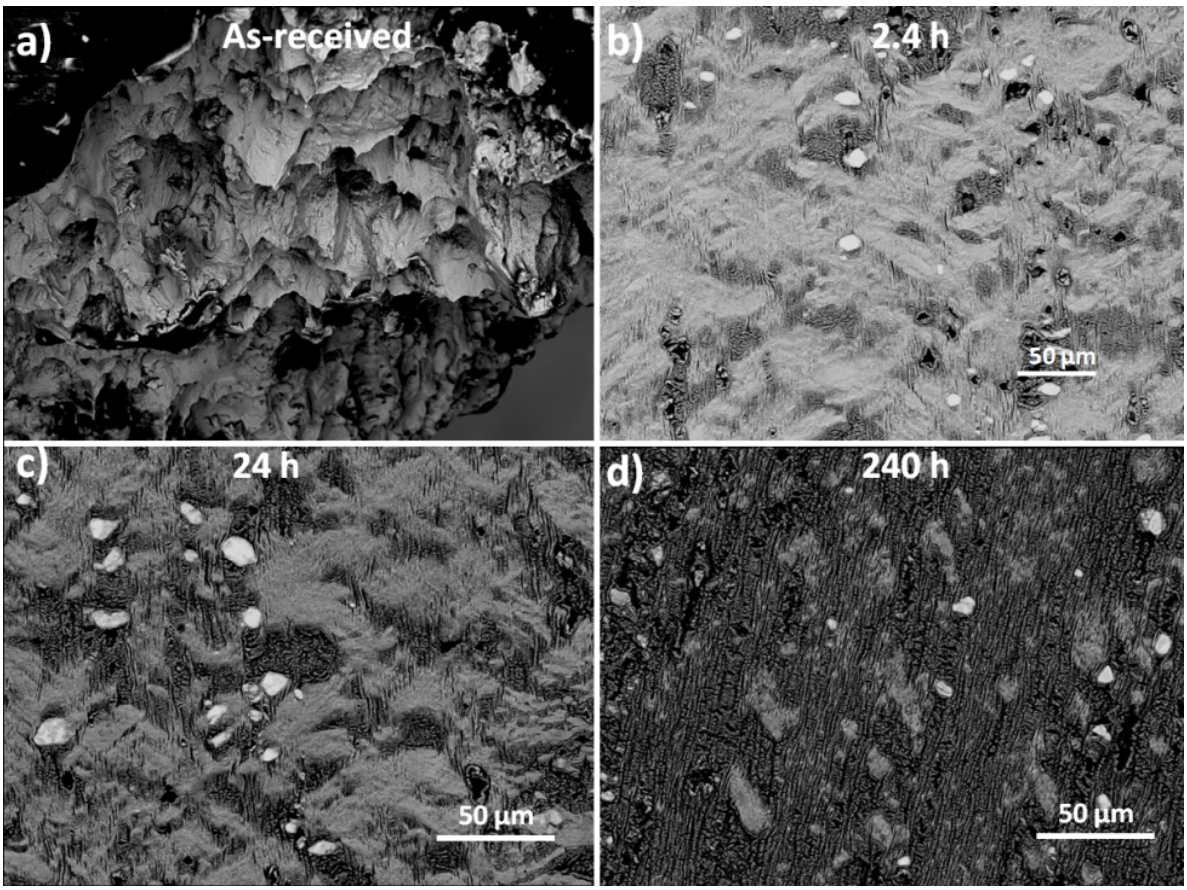

Figure 23: BSE images of fracture surfaces for as-received (a) and TMT DAFA29 (Method#1, b is for 2.4h, c is for 24 h and d is for 240 h) tensile tested at 700ºC annealed for the times indicated.

As-received and TMT DAFA29 samples were also tested at elevated temperatures from 600ºC to 800ºC. The resulting true stress-strain curves are shown in Figure 24. At 600ºC (Figure 24a), the stress-strain curve of as-received DAFA29 has a yield stress of 535 MPa, shows considerable work-hardening and an ultimate tensile strength of 665 MPa at an elongation of 20 %. The TMT alloys showed higher yield strengths of 928 and 886 MPa for Method#1 and Method#2, respectively. At 800ºC, the yield strength of as-received DAFA29 decreased to 360 MPa with no work-hardening evident. The yield strength of TMT alloys decreased dramatically lower to 150 (Method#1) and 120 MPa (Method#2) with elongations more than 40 %.

Figure 25 provides a summary of the yield stress of as-received and TMT DAFA29 tested at different temperatures. The behavior of as-received DAFA29 is similar to many f.c.c. alloys reported in the literature, i.e.: nickel-base superalloys and nickel iron-base superalloy. The yield strength is not greatly affected by the increase in temperature until it reaches a certain temperature. This transition temperature is 600ºC for the as-received DAFA29. The flow stress of $L1_2$ precipitates increase anomalously as temperature increases [10]. Therefore, the temperature independence of the yield strength of AFA alloys until 600ºC is the net effect of strength reduction of the f.c.c. phase compensated by the increase of strength from $L1_2$ precipitates.

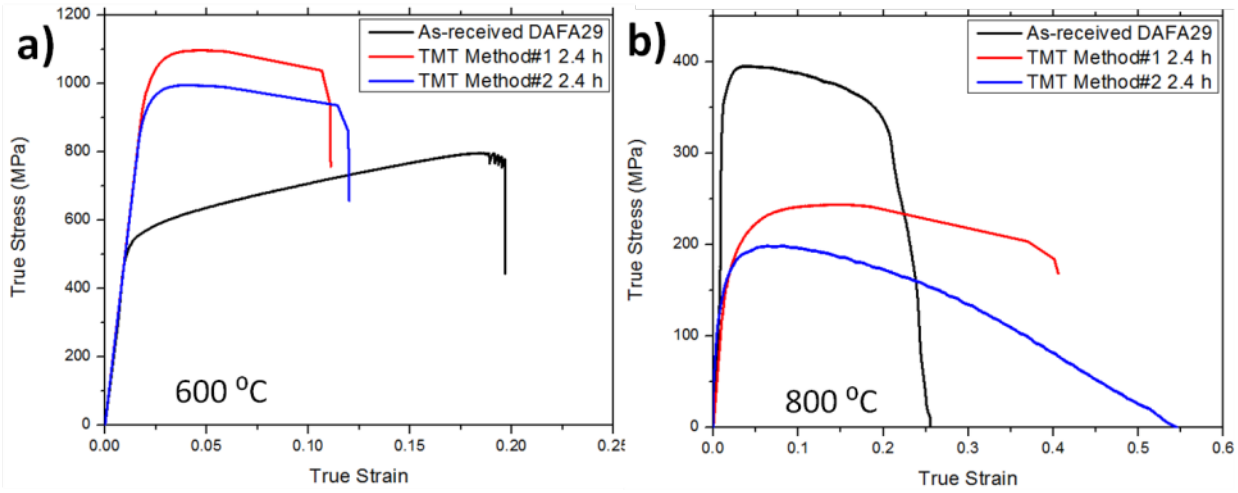

Figure 24: True stress-strain curves for as-received and TMT DAFA29 at 600ºC (a) and 800ºC (b). All the tensile tests were performed with an initial strain rate of 5 × 10^{-4} s^{-1}.

The TMT AFA alloys show yield stresses significantly larger than the as-received DAFA29 at room temperature. This is due to the fine grain size present after the TMT process for both TMT methods (100-200 nm). The yield stress of the TMT alloys decreased gradually up to 600ºC and then decreased dramatically at 700ºC. This significant loss of strength above 600ºC might be due to increased diffusion rates in TMT alloys leading to dislocation climb. The grain boundaries in TMT alloys lose their ability to interrupt dislocation motion due to the dislocation climb. The grain boundaries work as sites of weakness above 600ºC. At 800ºC, this grain boundary effect is more obvious. The yield strength of TMT alloys is less than half of the yield strength of as-received DAFA29 as shown in Figure 25. At this temperature, dislocations will be able to move around obstacles easily, the grain refined TMT alloys become significantly weaker.

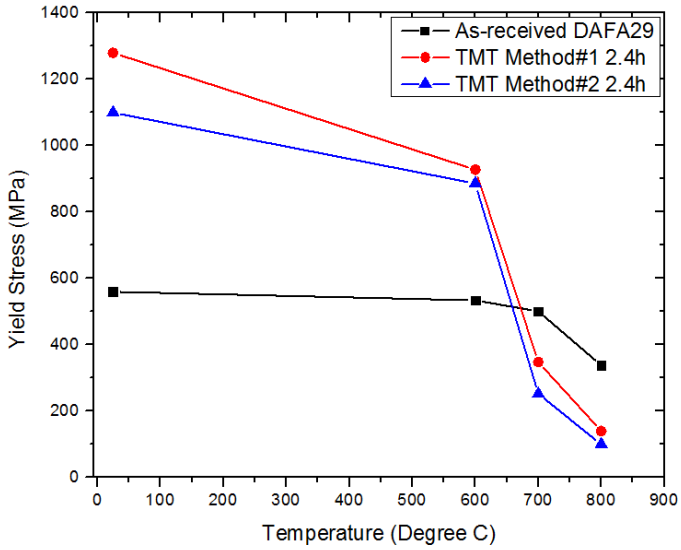

Figure 25: Yield stress of as-received DAFA29 and TMT DAFA29 (Method#1 and Method#2) as a function of temperatures (All the tests were performed at strain rate of 5 × 10^{-4} s^{-1}).

2.2.6 Strain Rate Influence on Microstructures

Generally, the flow stress of alloys at elevated temperature is a function of the applied strain rate. The magnitude of the effect is expressed by the strain rate sensitivity *m*. Theoretically, it is possible to carry out a series of tensile tests at various temperatures and strain rates. In practice, this is rarely done because of the limitations of time and the numbers of specimens required. Instead, strain rate jump tests can be performed using a single specimen. The strain rate is increased to a second level (approximately an order of magnitude) once a steady state flow stress is obtained.

Strain rate jump experiments were performed on as-received and TMT DAFA29 at 600ºC. The strain rate jump test results are shown in Figure 26a. The initial strain rate was 5×10^{-5} s^{-1} with an order of magnitude increase for each jump. The flow stresses of both TMT alloys increased with the strain rate increases. But, the flow stress of as-received DAFA29 is relatively independent of strain rate at this temperature. It is insensitive to the strain rate change at 600ºC.

Strain rate jump tests were also performed at 700ºC which is the target application temperature for AFA stainless steels. The results of strain rate jump tests of as-received and TMT alloys are shown in Figure 26b. The initial strain rate was 5×10^{-5} s^{-1} with an order of magnitude increase for each jump. The flow stresses of all samples increased as the strain rate increased. At the strain rate of 5×10^{-5} s^{-1}, the flow stress of as-received DAFA29 was 445 MPa which is almost twice that of TMT DAFA29 of 292 MPa. When the strain rate is jumped to 5×10^{-2} s^{-1}, the flow stress of as-received DAFA29 was 829 MPa, which is less than that of TMT DAFA29 of 1080 MPa.

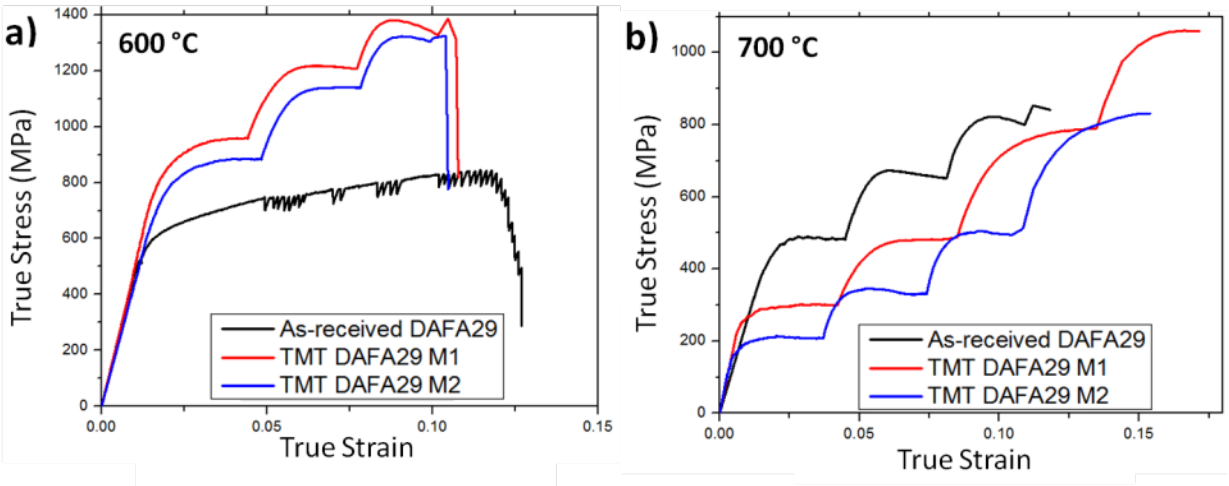

Figure 26: Strain rate jump tests of as-received and TMT DAFA29 (Method#1 and Method#2) at 600ºC (a) and 700ºC (b). Each strain rate jump is increased by an order of magnitude starting at an initial strain rate of 5×10^{-5} s^{-1}.

In order to understand the fracture behavior of as-received DAFA29 at different strain rates, tensile tests of as-received DAFA29 alloys were performed at 700ºC for selected strain rates (5×10^{-6} s^{-1}, 5×10^{-4} s^{-1}, and 5×10^{-2} s^{-1}). The resulting true stress-strain curves are shown in Figure 27. The flow stresses are comparable to the results from the strain rate jump test results shown in

Figure 26. Both the yield strength and work-hardening rate increase with increasing strain rate. A summary of the yield strengths and work-hardening rates is shown in Table 4.

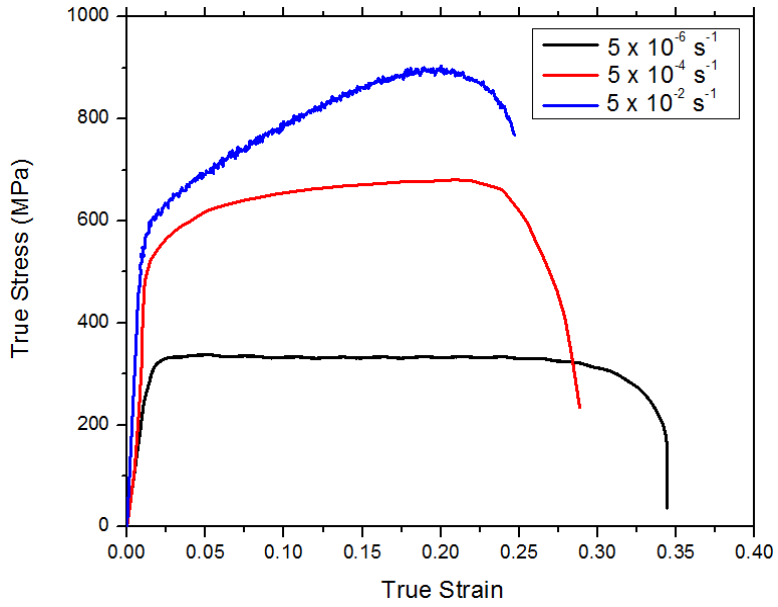

Figure 27: True stress-strain curves for as-received DAFA29 at different strain rates at 700°C.

Table 4: Yield strength and work-hardening exponent, n, of as-received DAFA29 at different strain rates. n is the exponent in the relationship $\sigma = K\varepsilon^n$, and can be obtained based on a log(σ) - log(ε) plot.

Strain rate (s^{-1})	Yield strength (MPa)	Work-hardening exponent n
5×10^{-6}	280	0
5×10^{-4}	523	0.10
5×10^{-2}	580	0.19

TEM observations were used in order to investigate the distribution of dislocations at 700ºC. Figure 27 shows BF TEM images for the samples tested at different strain rates. The sample (Figure 28a) tested at 5×10^{-2} s^{-1} has the highest dislocation density compared to the other two samples. The high dislocation density in Figure 28a effectively enhanced the dislocation interactions, which created additional barriers in the lattice for slip. These barriers produced the high work hardening rate observed at this strain rate (Figure 27). For the lower strain rates, the dislocation density was lower. The samples tested at both 5×10^{-4} and 5×10^{-6} s^{-1} show no work hardening and lower dislocation densities. The dislocations in Figure 28a are observed to align along one direction. This might be due to the high strain rate during the tensile test.

In Figure 28c, Fe_2Nb Laves phase and NiAl precipitates are present. These precipitates are located on grain boundaries and they are generated during the low strain rate test. Small (~26 nm) spherical $L1_2$-$Ni_3(Al,Ti)$ precipitates are also uniformly distributed in the f.c.c. matrix. The dislocations show strong interactions with these $L1_2$ precipitates. Numerous dislocation loops around $L1_2$ precipitates are present. The pinning effects of the precipitates result in the

observed wavy dislocations. On the grain boundaries, numerous dislocations are crowded around the Fe_2Nb Laves phase suggesting that the Laves phase precipitates are very strong obstacles to dislocation motion.

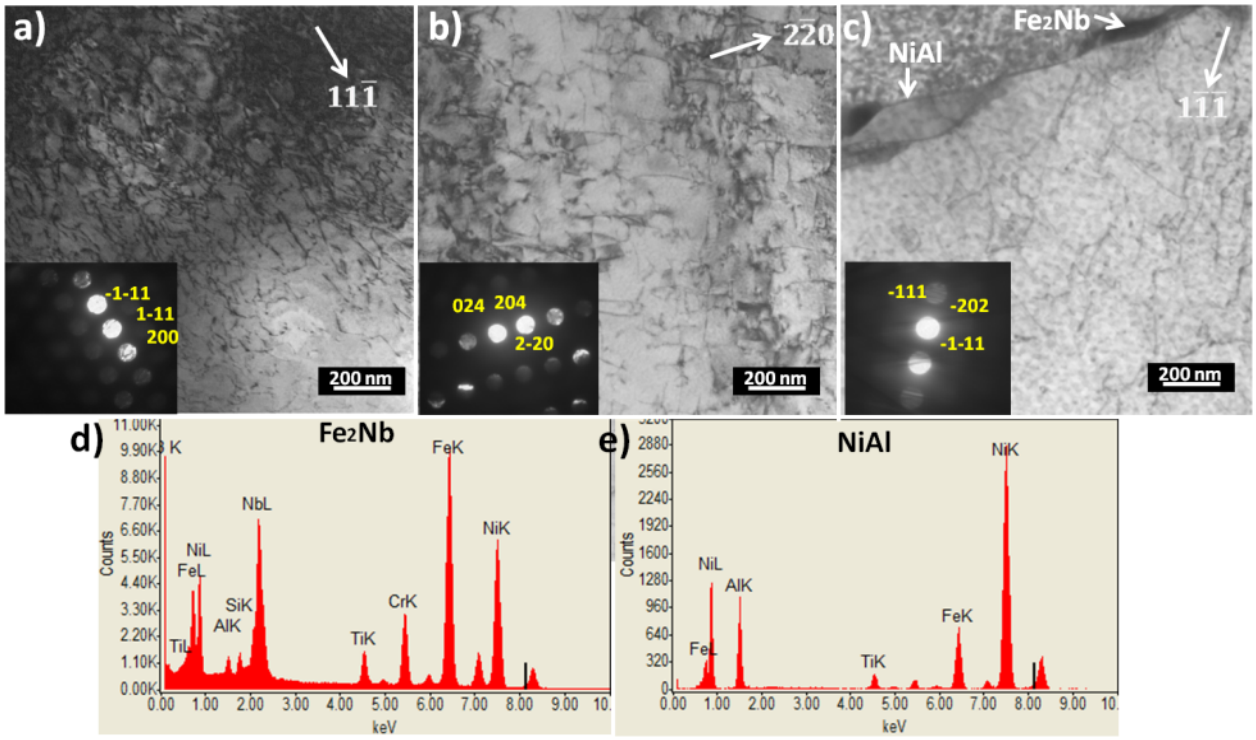

Figure 28: BF TEM images of dislocations in DAFA29 after 700°C tensile tests at different strain rates: (a) 5×10^{-2} s^{-1}, (b) 5×10^{-4} s^{-1}, (b) 5×10^{-6} s^{-1}. (d) and (e) show EDS results from the grain boundary precipitates of Fe_2Nb and NiAl in (c) for the sample test.

In the sample tested at strain rate of 5×10^{-6} s^{-1}, multiple slip features were observed in the grain boundary Laves phase precipitates. These slip features are speculated to be formed during the high temperature tensile tests at this slow strain rate. The slip bands are ~100 nm wide, see Figure 29a. All these slip features are aligned along <10-10>. Figure 29b shows a selected area diffraction pattern from this precipitate. The zone axis is [11-20]. These slip features are expected to be on the basal planes [11]. In order to confirm this, the Laves phase precipitate was characterized at different diffraction conditions.

Figure 29c, d and e show BF TEM images of the Laves phase precipitate observed at different zone axis. When viewed along both [11-20] and [1-100] the slip features are observed as lines, see Figure 29c and d, Viewing along the [10-11] (Figure 29e), those features became slip bands. By orienting these features corresponding to the [11-20] zone axis based on SAD patterns, we confirm these stacking faults are on the basal planes of the Laves phase. The fringes in both Figure 29c and d are the edge on of these parallel planer features. The white arrows in Figure 29e shows one of these features with a partial dislocation at the end of one or multiple stacking faults. This is similar to previous observation of stacking faults and bounding dislocations in other C14 structures such as Cr-Ta and Cr-Nb system [11, 12], Cr-Ti and Cr-Hf system [11, 13]

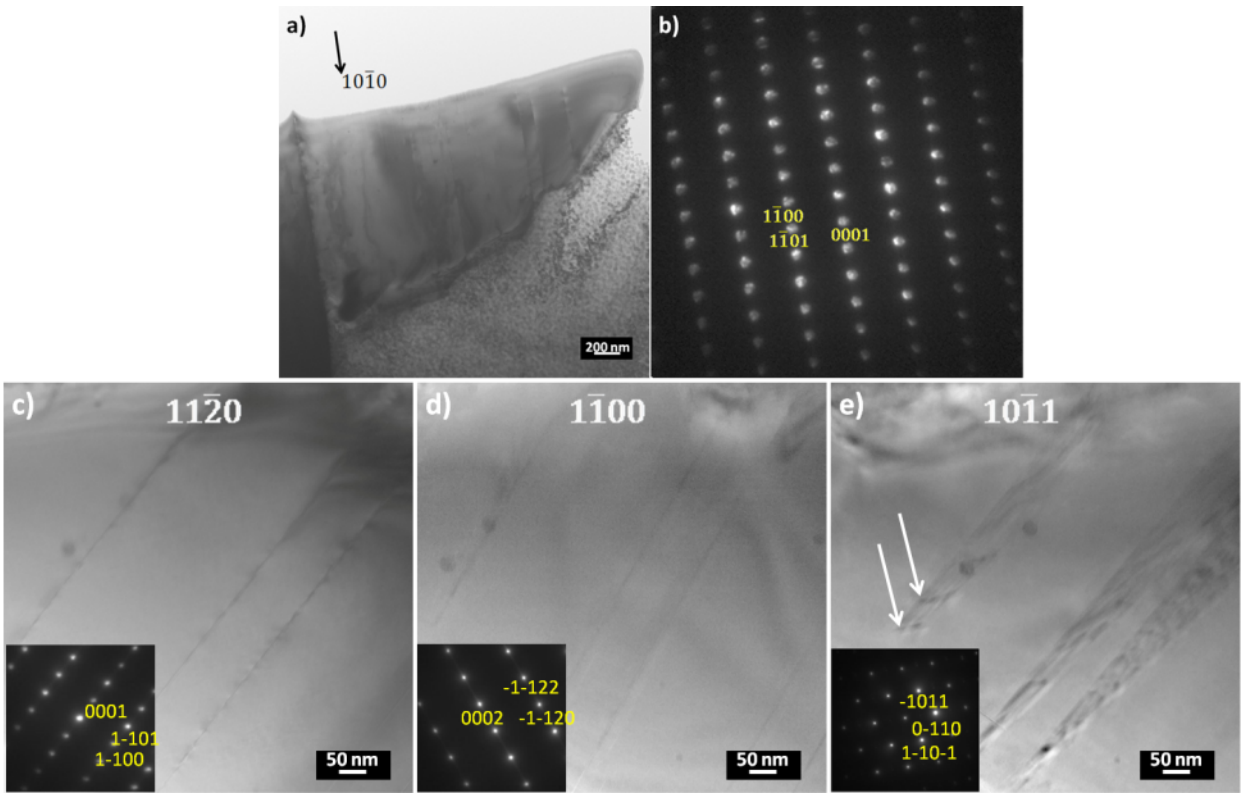

Figure 29: BF TEM images of stacking faults in a Laves phase precipitate in the as-received DAFA29 tested at 700ºC at 5 × 10^{-6} s^{-1}. (a) Laves phase precipitate, (b) the SAD on this precipitates. (c), (d), and (e) are the BF TEM images of stacking faults observed.

At 700ºC, the yield strength of as-received DAFA29 is 523 MPa, which is slightly lower than its room temperature yield strength 560MPa [14]. The alloy work-hardens significantly with an elongation of 20 % at room temperature, while it shows a low work-hardening rate at 700ºC with an elongation of 28 %.

The TMT alloys show lower yield strength (~390 MPa) but higher elongation compared to the as-received DAFA29, see Figure 22 and 25. It is evident that the TMTs which result in a fine grain size significantly improve the room temperature properties, but this grain size strengthening is negligible at 700ºC. At room temperature, assuming the off-set stress σ_0 is constant for all TMT alloys, the estimate grain size strengthening effect is ~600 MPa according to the relationship $\Delta\sigma = KD^{-1/2}$ [14, 15].

As the temperature increases to 700ºC, the grain boundary strengthening effect became negligible due to the weakness of the grain boundaries. The high volume of grain boundaries in the TMT alloys is unable to block the motion of dislocations. For the 2.4 h annealed samples, the TMT Method#1 alloy still showed higher strength than TMT Method#2 alloy at 700ºC although it has more grain boundaries (smaller grain size). This is mainly because the high temperature strength of TMT alloys has a strengthening contribution from the small Laves phase precipitates as well as the grain boundaries. The Laves phase precipitates in TMT Method#1 alloys are in the

range of 167 ± 37 nm which is slightly smaller than it is in TMT Method#2 alloys (175 ± 45 nm).

For all the annealed specimens, the 2.4 h and 24 h annealed TMT method#1 alloys shows higher yield strength compared to TMT Method#2 alloys due to a smaller grain size. When the annealing time was increased to 240 h, TMT Method#2 alloys have higher strength than TMT Method#2. This might be due to an increase in the volume fraction of the Laves phase during the long time aging process. After 240 h aging, the large Laves phase precipitates in TMT Method#2 alloys are not present. Instead smaller Laves phase are precipitated out with a size of ~560 nm. In TMT Method#1 alloys, there are still large Laves phase precipitate present in the microstructure

Table 5 summarizes the flow stress at different strain rates for the as-received and TMT DAFA29 alloys.

Table 5: Summary of flow stress at different strain rate for the as-received and TMT DAFA29 at 600°C and 700°C. The flow stress was defined as the peak stress.

Strain rate (s^{-1})	Flow stress (MPa)					
	600ºC			700ºC		
	DAFA29	Method#1 2.4h	Method#2 2.4h	DAFA29	Method#1 2.4h	Method#2 2.4h
5×10^{-5}	742	958	885	489	301	214
5×10^{-4}	792	1216	1138	673	482	346
5×10^{-3}	828	1375	1322	822	789	505
5×10^{-2}				853	1061	831

At 600ºC, which is $<0.5T_m$ (T_m is 1365ºC for as-received DAFA29), the $L1_2$ precipitates in the as-received DAFA29 are fine (~10 nm) due to the slow coarsening rate at this temperature. There is a strong dislocations cutting of forest dislocations and dislocation shearing of precipitates. This dislocation cutting and shearing results in a stress independent of the strain rate with a low strain rate sensitivity of 0.02. As the grain size decreases into the nano-size range for the TMT alloys, the rate-limiting process is increasingly influenced by the interactions of grain boundaries with dislocations, due to thermally activated dislocation annihilation at grain boundaries. This results in a larger strain rate sensitivity for all TMT alloys even at 600ºC.

At 700°C ($>0.5T_m$), the $L1_2$ precipitates coarsened to a larger size (~26 nm) during the slow strain rate testing process. The dominant mechanism changed to dislocation looping and dislocation precipitate interaction stress decreased due to $L1_2$ coarsening. At this temperature, the work hardening is negligible. The reduction of work hardening in DAFA29 is due to a softening mechanism such as dynamic recovery, which is prominent at elevated temperature. This lower strengthening effect and loss of work hardening resulted in higher strain rate sensitivity *m* of 0.12. The precipitate coarsening during the strain rate jump testing affects the flow stress behavior.

2.2.7 Strain Rate Sensitivity

The flow stress and strain rate are typically related at elevated temperature by the following equation:

$$\sigma = C\dot{\varepsilon}^m$$

where C is a constant, σ is the flow stress, $\dot{\varepsilon}$ is the strain rate, and m is the strain rate sensitivity. Based on the flow stress results shown in Table 5, the flow stress is plotted as a function of strain rate on a log-log scale in Figure 30. The strain rate sensitivity m can be obtained from

$$m = \frac{\log(\sigma)}{\log(\dot{\varepsilon})}$$

The m value can be obtained based on a linear fit as shown in Figure 30. m of as-received DAFA29 is 0.12, while the values for TMT DAFA29 is 0.18 (Method#1) and 0.19 (Method#2), i.e. the yield stresses of the TMT DAFA29 alloys are more sensitive to strain rate compared to the as-received DAFA29 at 700ºC. The slight difference in m values for TMT Method#1 and Method#2 is probably due to different grain sizes. At 600ºC, m for as-received DAFA29 is 0.02, whereas the m values for the TMT AFA alloys are 0.08 (Method#1) and 0.09 (Method#2). All the m values obtained at 600ºC are much smaller than those obtained at 700ºC, indicating that the strain rate sensitivity is influenced by the temperature for all tested alloys.

At both 600ºC and 700ºC, the alloys treated by Method#2 with a grain size of ~200 nm have a slightly higher m than alloys treated by Method#1. Alloys treated by Method#1 have a grain size of ~100 nm which is about half size of alloys treated by Method#2. It shows an increase in strain rate sensitivity with decreasing grain size. This trend has also been observed in other nanocrystalline alloys [16, 17].

At the same testing temperature, the strain rate sensitivity is larger for the smaller nano-sized grains in the TMT alloys compared to coarse grains of ~40 μm for the as-received DAFA29. A number of models [16, 18, 19] indicate the grain size dependence of the strain rate sensitivity is related to a decrease in the activation volume V.

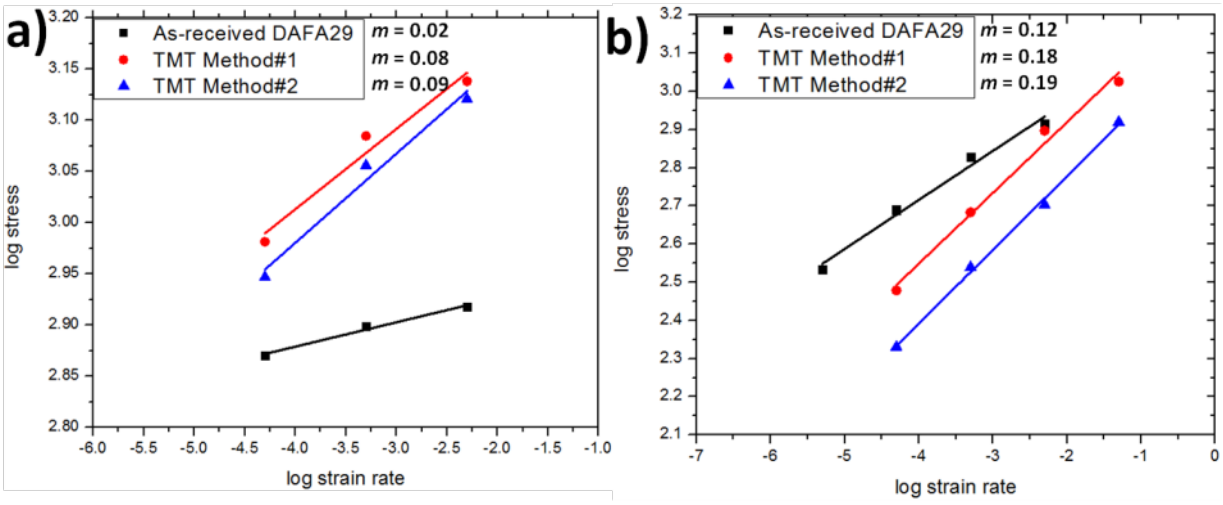

Figure 30: Flow stress as a function of strain on log-log scale plots from data obtained for alloys tested at (a) 600°C and (b) 700°C.

The strain rate sensitivity m can also be expressed as [17, 18, 20]:

$$m = \frac{\sqrt{3}kT}{V\sigma}$$

where k, T, V and σ are Boltzman constant, absolute temperature, activation volume and yield/flow stress, respectively.

The activation volume V is broadly defined as the rate of decrease of activation enthalpy with respect to the flow stress at a fixed temperature. It influences the rate-controlling mechanisms in the plastic deformation of engineering metals and alloys [17]. Based on analysis of the activation volume, one may suggest a hypothesis about the controlling deformation mechanisms in the TMT alloys. The value of V is some two orders of magnitude smaller for nanocrystalline metals than for microcrystalline metals [17].

The activation volume V can be calculated based on the two previously listed equations. A plot of log ($\dot{\varepsilon}$)/log (σ) as function of σ has a slope of $V/\sqrt{3}kT$ and activation volumes can be obtained based on the value of the slope. The activation volume for metals is normally expressed in terms of b^3, where b is the shortest burgers vector of a perfect dislocation. In f.c.c. iron the burgers vector is 0.253 nm. The calculated activation volumes for DAFA29 at 700ºC is 1.1 b^3 (65 b^3 at 600 ºC), while the values for the TMT alloys are 0.7 b^3 (Method#1) and 0.8 b^3 (Method#2), respectively. The activation volume for the fine grained TMT alloys is smaller than that of the coarse-grained alloys. Dislocations have a higher activation barrier when the grain size enters the nanometer regime. This is similar to other alloys tested at both room temperature and elevated temperature [21-23]. The mechanisms related with low activation volumes in nanograin materials are thought to be associated with thermally-activated diffusion processes at the grain boundaries [24].

2.2.8 Deformation Mechanisms

The relationship between strain rate and stress of the precipitation-strengthened alloys at elevated temperature can be described by a power law relationship [25-27]:

$$\dot{\varepsilon} = A\left(\frac{GbD}{kT}\right)\left(\frac{\sigma}{G}\right)^n$$

where G is the shear modulus (MPa), b is the Burgers vector (nm), D is the diffusion coefficient of the f.c.c. matrix (m^2/s), k is the Boltzmann constant, T is the absolute temperature (K), and n is the stress exponent. A stress exponent n in the range of 3-5 is typical for solid solution alloys. Specifically, n is 5 for nickel and nickel-chromium alloys [13, 26, 28]. For precipitate-strengthened alloys, the n values obtained are normally larger than those obtained for solid solution alloys [27]. The high stress exponent arising from small dispersed precipitates being obstacles to the movement of dislocations [29, 30].

In order to reduce the high stress exponent values, a threshold stress term σ_t is introduced into the above equation to account for the influence of the precipitates. The effective stress is defined as $\sigma - \sigma_t$. Thus, the above equation can be rewritten:

$$\dot{\varepsilon} = A'\left(\frac{GbD}{kT}\right)\left(\frac{\sigma - \sigma_t}{G}\right)^n$$

The value of the threshold stress σ_t depends on the dislocation precipitate interaction mechanism. The mechanism could be dislocation cutting, Orowan looping, or dislocation climb. This value can be determined using the methodology suggested by Lagneborg and Bergman [31]. This equation can be rewritten:

$$\dot{\varepsilon}^{1/n} = A''(\sigma - \sigma_t)$$

where all the constant terms are collected in the constant *A"*. The threshold stress σ_t can be obtained from a plot of $\dot{\varepsilon}^{1/n}$ as a function of σ, as shown in Figure 31 and the threshold stress is the x-intercept. The threshold stress obtained using this method is 217 MPa for as-received DAFA29 at 700ºC, which is similar to the threshold stress value measured in another AFA alloy tested at the same temperature [25]. The threshold stresses are 50 MPa (Method#1) and 9 MPa (Method#2) for the TMT alloys tested at 700ºC. These values increase to 670 MPa (Method#1) and 574 MPa (Method#2) for the TMT alloys tested at 600ºC. Table 6 provides a summary of threshold stresses for the different processing conditions. The threshold stress of alloys treated by Method#1 is slightly larger than that of Method#2 for both temperatures. The value of the threshold stress decreased significantly with an increase in temperature, and is almost zero for alloys treated by Method#2 at higher temperature.

Table 6: Threshold stresses extrapolated from $\dot{\varepsilon}^{1/5}$ vs σ plots.

	Threshold stress (MPa)		
Temperature (ºC)	**As-received DAFA29**	**TMT Method#1**	**TMT Method#2**
600	--	670	574
700	217	50	9

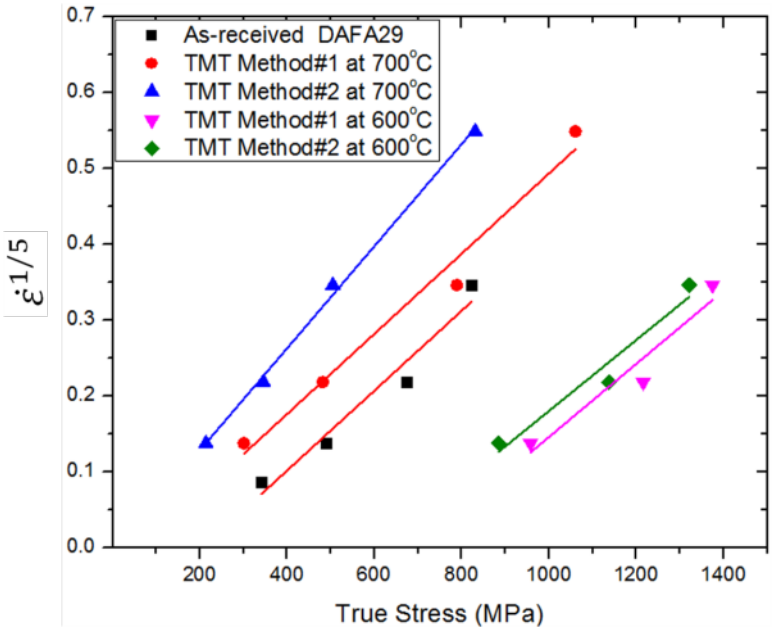

Figure 31: Plots of $\dot{\varepsilon}^{1/5}$ as a function of stress for as-received DAFA29 and the TMT alloys.

Figure 32 shows a plot of strain rate as a function of effective stress (σ - σ_t) for the as-received and TMT DAFA29 alloys. The corrected *n* value is 4.2 for the as-received DAFA29 tested at 700ºC which is close to the stress exponent value of another AFA alloy reported in [25]. At 600ºC, the *n* values of treated alloys decrease to 4.9 and 5.0 which are typical of *n* values for solid solution alloys [32].

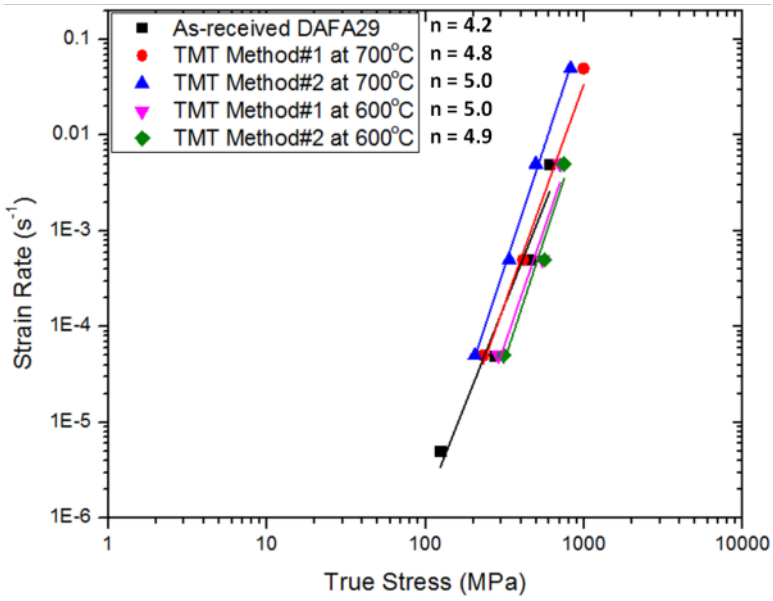

Figure 32: Strain rate as a function of the effective stress (σ - σ_t) for as-received and TMT DAFA29 alloys. The plots are on log-log scales.

The extrapolated threshold stresses of the treated alloys at 600ºC are much higher than those obtained at 700ºC. They decrease significantly with the increase in temperature of 100ºC. Three possible mechanisms are considered to explain the threshold stress in precipitation-strengthened alloys: 1) precipitate cutting, 2) Orowan dislocation bowing, and 3) dislocation climbing.

The Orowan dislocation bowing stress for dislocations that interact with the $Ni_3(Al,Ti)$ particles is given by:

$$\tau_o = \frac{Gb}{L - 2r}$$

where τ_o is the shear stress necessary for precipitates bypass by Orowan bowing, L is particle spacing, r is the radius of precipitates.

At 700ºC, the average size of $Ni_3(Al, Ti)$ precipitates is 30 nm after an 800ºC anneal for 2.4 h. The particle spacing obtained based on L and the volume fraction is 140 nm. The volume fraction of $L1_2$ phase can be calculated based on density and phase fraction from a JMatPro simulation shown in Figure 33. G is approximately 50 GPa for AFA alloys and b is estimate to be 0.253 nm. The calculated Orowan shear stress is about 180 MPa for both TMT AFA alloys. The threshold stress values of TMT alloys are about $0.3\tau_o$ (50 MPa for Method#1) and $0.05\tau_o$ (9 MPa for Method#2). These values are similar to those obtained from the Arzt-Ashby model

for the local climb and general climb mechanisms [33]. For as-received DAFA29, the calculated Orowan shear stress is about 212 MPa with a particle spacing of 120 nm and average particle size of 26 nm. This Orowan stress is consistent with the threshold stresses of as-received DAFA29, which is 217 MPa.

At 600ºC, the threshold stress values are much higher than Orowan shear stress for both TMT alloys. This might be due to a change to a precipitate shearing mechanism and a higher volume fraction of $Ni_3(Al,Ti)$ at this temperature (Figure 33).

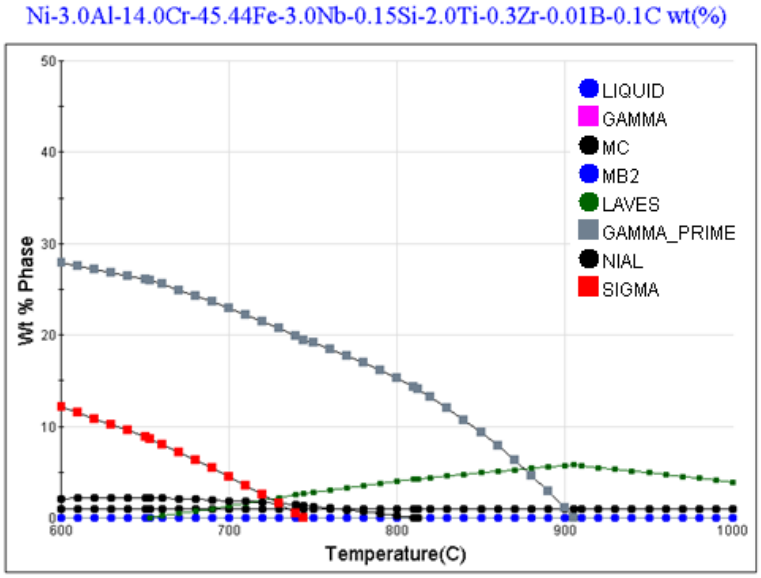

Figure 33: Phase fractions of different phases in DAFA29 alloys from a JMatPro simulation.

The activation energy (Q) can be determined by assuming that strain rate follows an Arrhenius type relationship [26, 34]:

$$\dot{\varepsilon}\exp(\frac{Q}{RT}) = A \cdot \sigma^n$$

where A is a constant, R is the gas constant and n is the stress exponent. This equation can be converted to the following equation [34].

$$\ln\sigma = \frac{\ln\dot{\varepsilon} - \ln A}{n} + \frac{1}{T} \cdot \frac{Q}{R \cdot n}$$

The activation energy under a constant strain rate was calculated based on the above equation. $Q/(R \cdot n)$ is the slope of $\ln\sigma$ plotted as a function of 1/T. Figure 34 shows the plot of $\ln\sigma$ as a function of 1/T for as-received DAFA29 and TMT alloys at strain rate of 5×10^{-5} s^{-1}. Based on the calculation, the activation energy for as-received DAFA29 is 124 kJ/mol. The activation energies of the TMT alloys are 409 kJ/mol for Method#1 and 491 kJ/mol for Method#2, respectively. The activation energy of as-received DAFA29 is similar to other AFA alloys studied by Zhou et al. [25]. The activation energy is slightly larger than other AFA alloys and austenite steels. But this high activation energy is also found in other superalloys such as alloy

617 [26] and IN 718 [35]. Such large values of activation energy can be reduced to 248–251 kJ/mol when considering the effective stress instead of the applied stress [36].

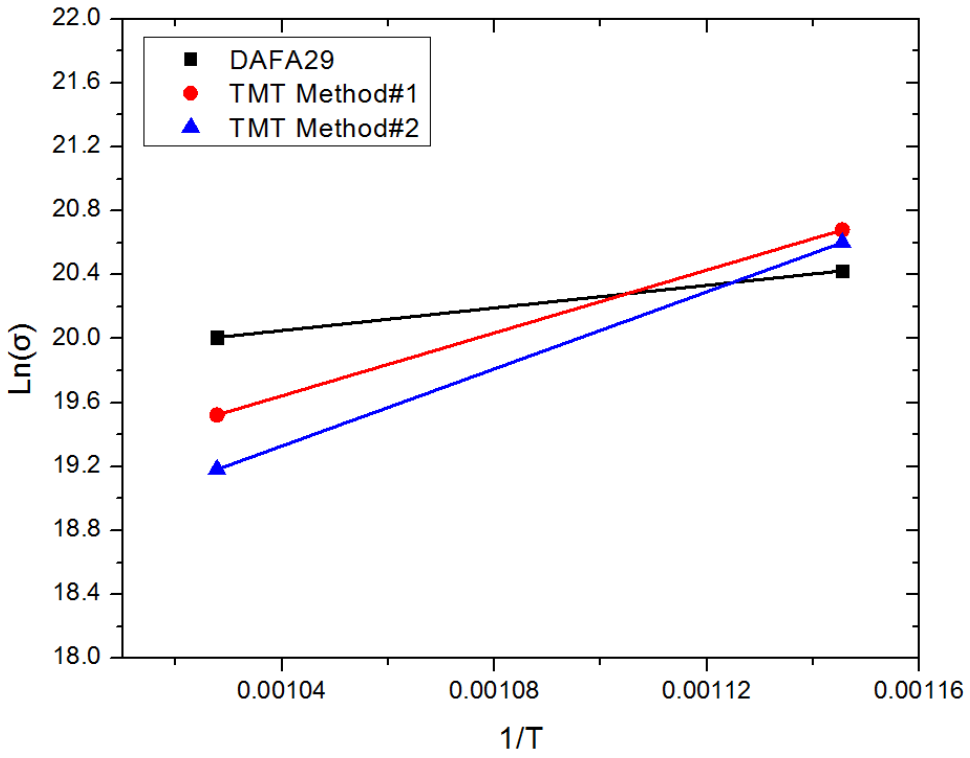

Figure 34: Plot of ln(σ) as a function of 1/T

2.2.9 The Effects of Annealing on the Microstructure and Mechanical Behavior

The effects of simply annealing at 800°C on the microstructure and mechanical properties of DAFA 26 and DAFA 29 were also examined. Figure 35a and b shows the microstructures of hot-rolled DAFA26 and DAFA29, respectively. The grain size of DAFA26 is ~30 µm while that of DAFA29 is ~40 µm. The white contrast elongated particles in DAFA26 are Laves phase, and are aligned in the hot rolling direction: no other precipitates were observed in DAFA26. The white contrast particles in DAFA29 are both Laves phase and MC carbides. The MC carbides normally have a blocky shape with sharp-edged geometry, while the Laves phase precipitates have an elongated shape due to the hot rolling. These two types of particles can easily be differentiated based on EDS results: EDS data from Laves phase and MC carbides in DAFA29 are shown in Figure 35c and d.

Twins were also observed in many grains in as-received DAFA26. The calculated twin boundary density in DAFA26 is 22 ± 4 /mm (28 twin boundaries counted) based on the method reported in [37]. Almost no twin boundaries were observed in as-received DAF29.

DAFA26

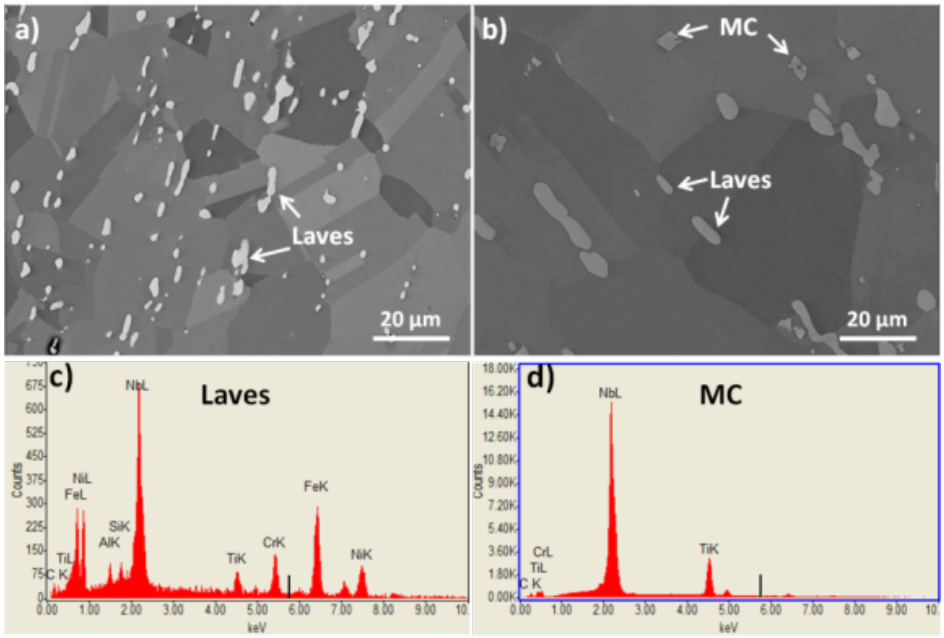

DAFA29

Figure 35. BSE images of as-received DAFA26 (a) and DAFA29 (b). (c) and (d) are EDS data from the Laves phase and MC carbide particles in (b). No MC carbides are present in DAFA26.

The microstructures of DAFA26 and DAFA29 are shown in Figure 36 after aging for 2.4 h, 24 h and 240 h at 800°C. There is no obvious grain growth for either DAFA26 or DAFA29 after these aging times. Twins were still observed in 240 h-aged DAFA26, but the twin boundary density was reduced to 16 ± 3 /mm (32 twin boundaries counted). Again, no twins were observed in aged DAFA29. The morphology and size of Laves phase (bright contrast) precipitates in DAFA26 didn't change during the aging process. The MC carbides still have the blocky shape with sharp-edged geometry. The average size of MC carbides also didn't increase even after 240 h aging.

As the aging time was increased, more and more grain boundary precipitates are observed in both DAFA26 and DAFA29. This is particularly evident for the alloys aged for 240 h as shown in Figure 36e and f. The grain boundary in DAFA29 is almost fully covered with these precipitates.

The small needle shape precipitates in the f.c.c. matrix of 240 h-aged DAFA26 and DAFA29 are co-precipitates of Laves phase and B2-NiAl phase based on EDS analysis. They had formed randomly inside matrix after 240 h aging.

Figure 37 shows high magnification BSE images of the grain boundary precipitates after aging at 800°C for different times. Figure 37a, c and e show BSE images of aged DAFA26 after aging times of 2.4 h, 24 h and 240 h. As the aging time increases, more Laves phase (bright contrast) and B2-NiAl (dark contrast) precipitates are formed on grain boundaries. The two precipitates are also identified by EDS in SEM. For the sample aged for 240 h, the grain boundaries are largely covered with the precipitates of Laves and B2-NiAl phase. The grain boundary coverage for this sample is 83 % according the calculation method used in [38, 39].

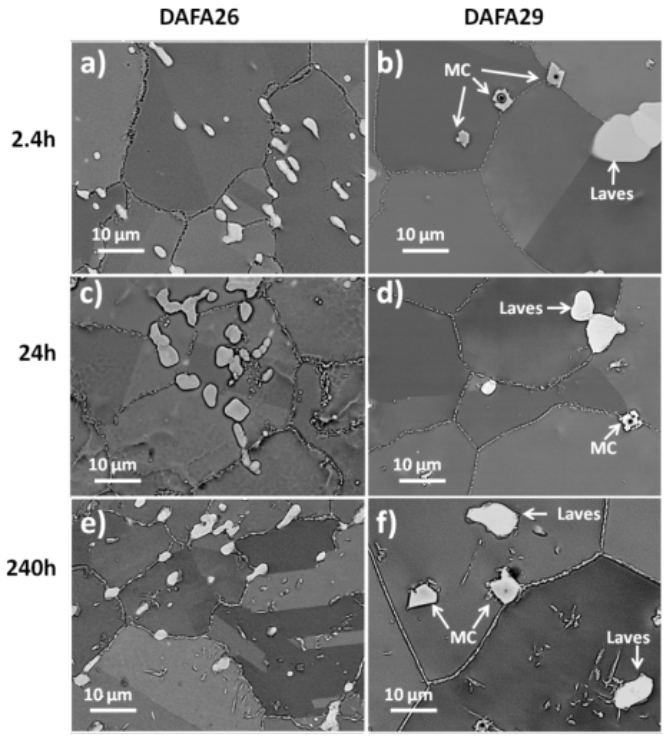

Figure 36: BSE images of the microstructures of the DAFA26 aged at 800°C for 2.4h (a), 24h (c), and 240h (e) and DAFA29 aged for 2.4h (b), 24h (d), and 240h (f).

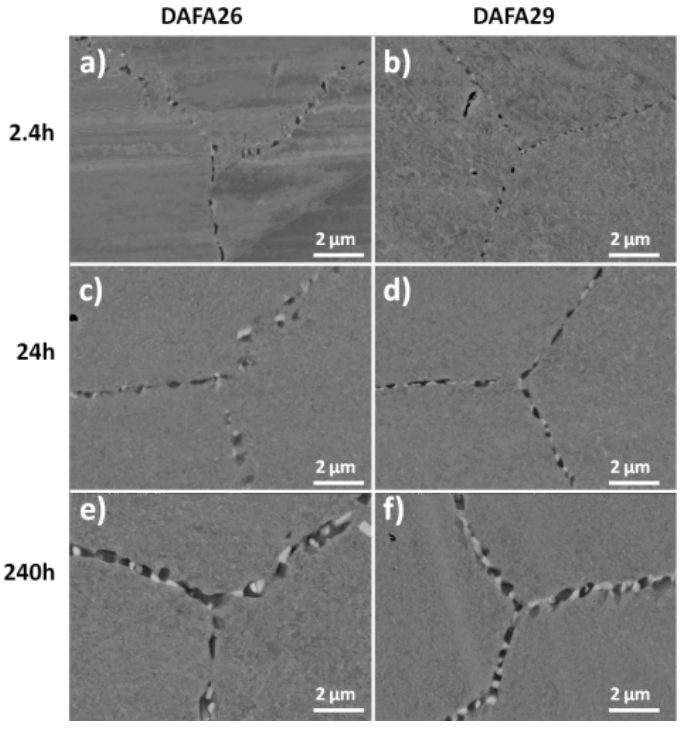

Figure 37: BSE images of the microstructures of the grain boundaries in DAFA26 aged at 800°C for 2.4h (a), 24h (c), and 240h (e) and DAFA29 aged for 2.4h (b), 24h (d), and 240h (f).

Similar phenomena were also observed for DAFA29, see Figure 37b, d, and f. As the aging time increased, increasing amounts of Laves phase and B2-NiAl precipitates formed on the grain boundaries. EDS measurements showed that no MC carbides were present. Laves phase and B2-NiAl precipitates are densely packed in the grain boundaries in 240 h-aged DAFA29 with a grain boundary precipitate coverage of 94 %, i.e. a higher grain boundary than in DAFA26.

In order to further determine the size of Laves phase precipitates and B2-NiAl precipitates in grain boundaries of 240 h-aged DAFA26 and DAFA29, samples were mechanical polished and characterized in SEM. BSE images of grain boundaries of 240 h-aged DAFA26 and DAFA29 are shown in Figure 38a and b. The lighter contrast particles in the grain boundaries are the Laves phase and the darker contrast particles in the grain boundaries are the B2-NiAl precipitates.

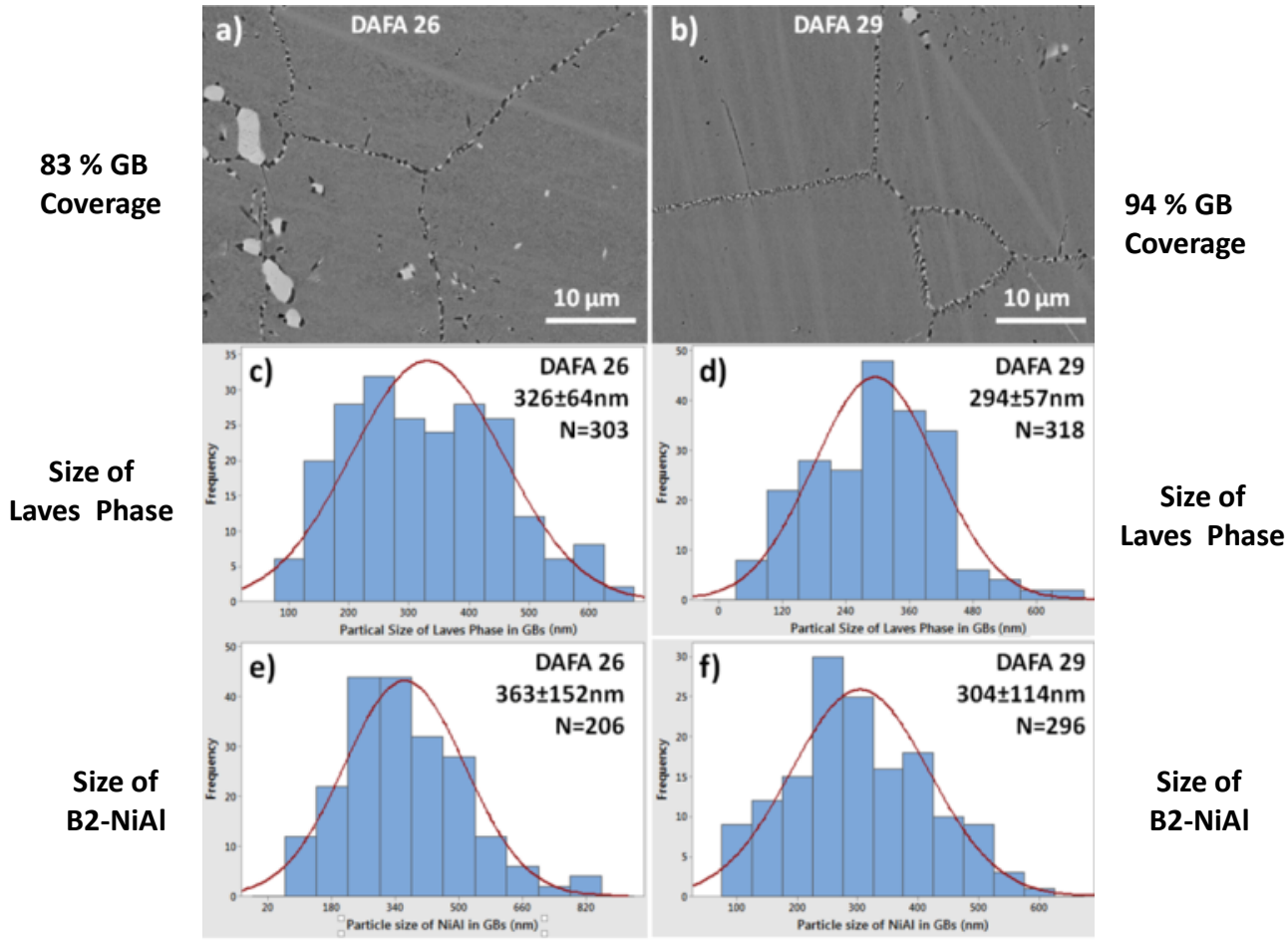

Figure 38: BSE images of grain boundary precipitates for (a) 240h-aged DAFA26 and (b) 240 h-aged DAFA29; (c) and (d) are histograms of the Laves phase size in the grain boundaries of DAFA26 and DAFA29, respectively; (e) and (f) are histograms of the NiAl size in the grain boundaries of DAFA26 and DAFA29, respectively. (N stands for the number of particles counted and ± means the standard deviation of the particle size.)

Statistical analysis was performed to characterize the size and size distribution of the Laves phase and B2-NiAl in the grain boundaries. The size distribution histograms of the Laves phase particles are shown in Figure 38c and d for 240 h-aged DAFA26 and DAFA29, respectively. The average size (defined as equivalent diameter sphere) of Laves phase is 326 ± 64 nm in DAFA26, which is 11 % larger than in DAFA29 (294 ± 57 nm). The histograms of the B2-NiAl are shown in Figure 38e and f for 240 h-aged DAFA26 and DAFA29. The average size is 363 ± 152 nm in DAFA26, while it is 304 ± 114 nm in DAFA29. Further, in 240 h-aged DAFA29, the grain boundary has 10% more precipitate coverage than in DAFA26. Thus, the boron in DAFA29 influences the distribution and inhibits the coarsening of the grain boundary precipitates. That boron suppress the coarsening of grain boundary precipitates has also been observed in Fe-20Cr-30Ni-2Nb (at.%) alloy [40, 41], Ni-Fe alloy [9, 42], and Nickel based superalloy (617B) [43].

The blocky MC carbides and Laves phase in the matrix of DAFA29 were very stable during the aging process, i.e. there was no significant change of size and morphology observed even after 240 h annealing.

The coarsening behavior of the $L1_2$ phase present in the matrix was also investigated using both the TEM and the SEM. Figure 39 shows TEM images of the coarsening of the $L1_2$ phase at different annealing times at 800ºC.

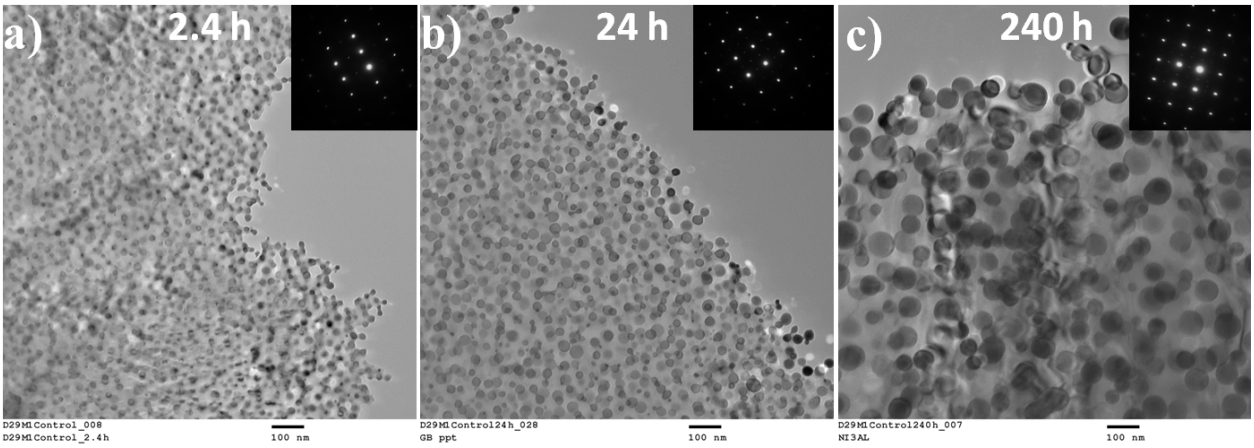

Figure 39: BF TEM images and electron diffraction patterns of DAFA29 after annealing at 800ºC for 2.4 (a), 24 (b), and 240 h (c).

Figure 40 shows SE images of the spherical $L1_2$ particles in all the aged alloys. The morphology of $L1_2$ particles is still spherical after 240 h aging at 800ºC. As the aging time increases from 2.4h to 240h, the $L1_2$ phase grew. Based on statistical analysis, the particle size (average diameter) of $L1_2$ particles in DAFA26 increases from 18 ± 2 nm to 62 ± 15 nm after aging for 240 h, while the $L1_2$ particles in DAFA29 grow from 17 ± 3 nm to 62 ± 14 nm. Histograms of the $L1_2$ particle size in DAFA26 and DAFA29 at each aging time are shown in Figure 41. The sizes of $L1_2$ particles are similar in both DAFA26 and DAFA29 for each aging time. The additions of boron and carbon in DAFA29 have no evident influence on the size and morphology of $L1_2$ particles.

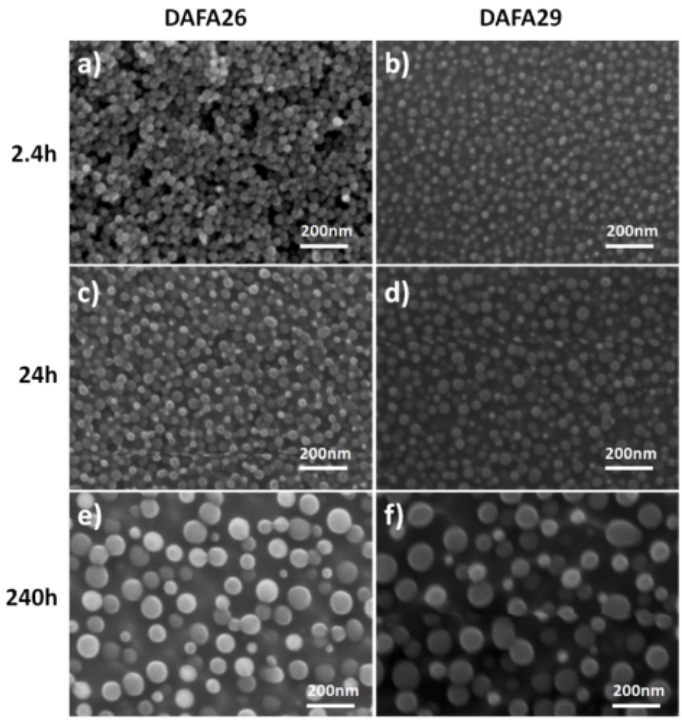

Figure 40: SE images of the $L1_2$ particles in the DAFA26 aged for (a) 2.4 h, (c) 24 h, and (e) 240 h and DAFA29 aged for (b) 2.4 h, (d) 24 h, and (f) 240 h.

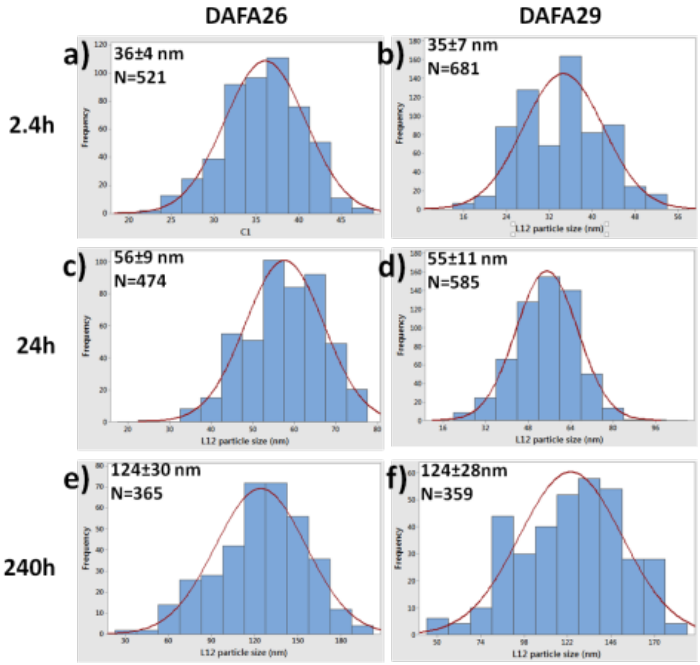

Figure 41: Histograms of particle diameter of $L1_2$ in the DAFA26 aged for (a) 2.4 h, (c) 24 h, and (e) 240 h and DAFA29 aged for (b) 2.4 h, (d) 24 h, and (f) 240 h. (N is the number of particles counted. ± means the standard deviation of particle diameter.)

The average diameter (d) of the $L1_2$ precipitates is plotted against the aging time in Figure 42a. The $L1_2$ size increases as the aging time increased for both aged DAFA26 and DAFA29. There is a linear relationship between d_t^3 - d_0^3 and t, where d_0 is the average diameter of the $L1_2$ phase in the as-received alloys (~10 nm). This linear relationship suggests coarsening of the $L1_2$ precipitates follows the Lifshitz-Slyozov-Wagner (LSW) model. Although the LSW model is strictly applicable when the precipitate volume fraction is very small, the cubic growth kinetics of the $L1_2$ particles has been observed in many superalloys [9, 44, 45]. The LSW model predicts time dependent coarsening behavior of the $L1_2$ particles by the following equations [44]:

$$d_t^3 - d_0^3 = kt$$

$$k = \frac{8\gamma V_m D C_m}{9RT}$$

where t is the aging time, d_t is the $L1_2$ particle size at the time of t, k is the coarsening rate, which depends on several parameters, γ is the interfacial energy between the precipitate and f.c.c. matrix, V_m is the molar volume fraction of $L1_2$ precipitates, D is the diffusion coefficient of the solute, C_m is the atomic fraction of solute in equilibrium with the precipitate, R is the gas constant, and T is the absolute temperature. The coarsening rate of the $L1_2$ particles in aged DAFA26 is similar to that of DAFA29, which suggests the coarsening kinetics of the $L1_2$ phase in both DAFA26 and DAFA29 are similar and follow the LSW model, i.e. the boron has no effect on the coarsening kinetics.

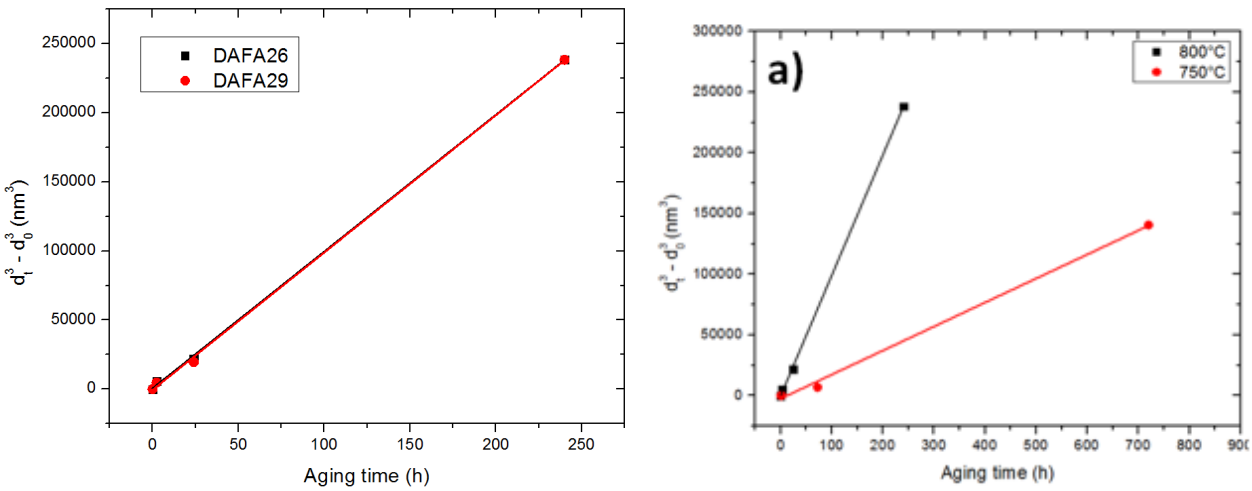

Figure 42: Plot of (a) $L1_2$ precipitate size versus aging time for both DAFA26 and DAFA29 at 800°C, and (b) $L1_2$ size versus aging time for DAFA26 at both 750 °C and 800 °C.

In order to estimate the activation energy, Q, of the coarsening of the $L1_2$ particles, DAFA26 was also aged at 750°C for 2, 72, and 720h. The plot of $L1_2$ size versus aging time at two different temperatures is shown in Figure 42b. At both 750°C and 800°C, the coarsening kinetics of the $L1_2$ particles again follow the LSW model and there is a linear relationship between d_t^3 - d_0^3 and t. As expected, the coarsening rate constant k is higher at 800°C compared to 750°C (k is 0.28 nm^3/s at 800°C, while it is 0.068 nm^3/s at 750°C).

Assuming that both the chemical composition and volume fraction of $L1_2$ particles do not change at a given temperature, the relation for calculating the activation energy Q for $L1_2$ coarsening can be described by:

$$Ln\ (kT) = constant - Q/T$$

This relation yields an active energy of 264 kJ/mol for $L1_2$ coarsening in DAFA26. This value is similar to the activation energy for volume diffusion of Ti and Al in Ni [44]. Similar values of activation energy of $L1_2$ coarsening have also been reported in other Ni/Fe-based superalloys [9, 44]. This result indicates the coarsening of $L1_2$ precipitates is mainly controlled by the volume diffusion of Ni and Al elements in f.c.c. matrix.

Returning to the grain boundary phases, discontinuous precipitation of the B2-NiAl phase was found in DAFA26 annealed for both 2.4 h and 24 h, but not for 240 h, see Figure 43. The precipitation was found to be common throughout all the grain boundaries for short-time aged DAFA26 (2.4 h and 24 h) microstructures examined. No preferred boundary misorientation for precipitation was found. TEM EDS results are shown in Figure 43c. These precipitates are rich in Ni, Fe, Cr and Al. This discontinuous precipitation was not found in any aged DAFA29 alloys based on both SEM and TEM observations. The boron and carbon additions in DAFA29 presumably suppress the discontinuous precipitation.

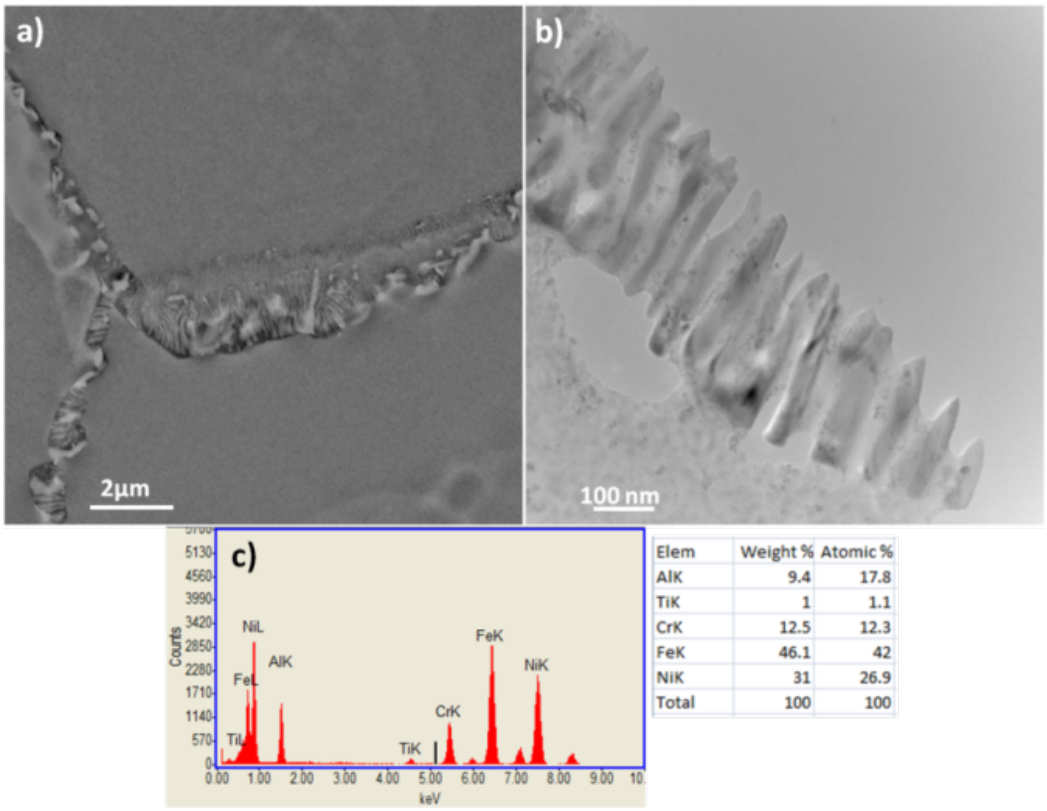

Figure 43: (a) BSE and (b) BF TEM images of discontinuous precipitation (cellular growth) in 2.4 h-aged DAFA26, and (c) TEM-EDS data from the precipitates.

This suppression of discontinuous precipitation by boron has also been found in other alloys systems such as Cu-Ti alloys [46] and Ni-Fe alloys [9, 37]. This is possibly because diffusion of elements in grain boundaries was diminished by boron or the mobility of the transformation in front of the grain boundaries was reduced probably owing to pinning effect of boron segregates or other precipitates.

Figure 44 shows a TEM image of Laves phase and B2-NiAl precipitates in a grain boundary of 240 h-aged DAFA29. EDS spectra of the three grain boundary precipitates are shown in Figure 44b, c and d. A small peak of boron is detected in the EDS spectrum for the Laves phase precipitate and the peak is located at 0.18 keV. No boron peak was detected in the two EDS spectra from the B2-NiAl precipitates. In the EDS data from the f.c.c. matrix, a carbon peak was detected at 0.28 keV. No carbon peak was found in the grain boundary precipitates.

Precipitate free zones (PFZ), with a width of 200 nm, are clearly observed around the grain boundary Laves phase and B2-NiAl precipitates. This zone lacks strengthening from the $L1_2$ precipitates compared to the f.c.c. matrix. EDS results from PFZ and f.c.c. matrix are shown in Figure 44e and f. These results show the microchemistry of the PFZ is mainly composed of Fe, Ni and Cr, while the f.c.c. matrix is composed of Fe, Ni, and Al. The f.c.c. matrix has more Ni, Al and Ti than the PFZ. This is because of the spherical $L1_2$-Ni_3(Al,Ti) precipitates are present in the f.c.c. matrix. There are almost no $L1_2$-Ni_3(Al,Ti) precipitates observed in the PFZ.

A PFZ can help to relieve stress concentrations on the grain boundary precipitates. However, if the zone is too ductile or too wide, it may create large strain concentrations in the grain boundary, resulting in enhanced grain boundary shear which may again lead to premature failure [47]. Baither et al. [48, 49] studied PFZs in polycrystalline γ'-strengthened nickel-based superalloy Nimonic PE16 using *in-situ* TEM. They confirmed that the PFZ will lower the yield strength only when PFZ's width exceeds 1.7*(L-r)*, where *L* is interparticle spacing and *r* is radius of the $L1_2$ particles. Beyond this width, dislocations are generated in the PFZ and the resulting dislocation pileups lead to the reduction of yield strength. For 240 h-aged DAFA29, the $L1_2$ volume fraction is 15.4 % and the average precipitate diameter is 62 nm. The calculated interparticle spacing L is around 133 nm based on following equation [50]:

$$L = \left(\sqrt{\frac{2\pi}{3f}}\right) \times r$$

where f is the volume fraction of $L1_2$ phase. The value of 1.7(L-r) is 178 nm, which is slightly smaller than the width of PFZ in 240 h-aged DAFA29 (200 nm). Thus, according to Baither et al.'s analysis [48, 49], the PFZs in the 240 h-aged DAFA alloys are starting to produce softening.

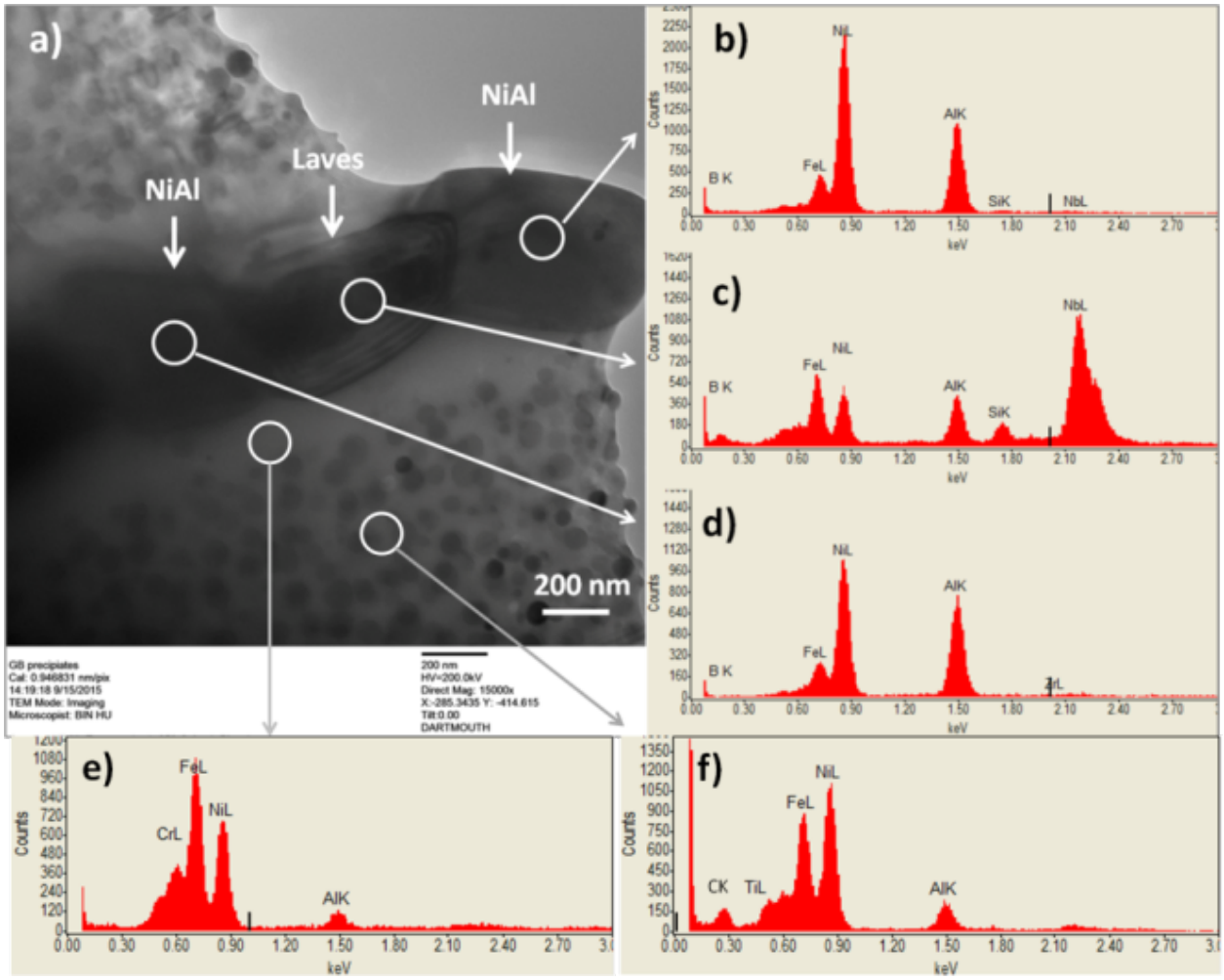

Figure 44: (a) BF TEM image, (b), (c) and (d) are EDS results of grain boundary precipitates in a grain boundary in DAFA29; (e) and (f) are the EDS results from the PFZ and the f.c.c. matrix.

Tensile testing of the aged DAFA26 and DAFA29 was carried out at 700ºC at an initial strain rate of 5×10^{-4} s^{-1}. The resulting stress-strain curves are shown in Figure 45. Both AFA alloys show much higher yield strengths after 2.4 h aging compared to the as-received alloys. Among all the aged samples, the maximum strength was achieved after aging for 2.4 h. The yield strength decreased after aging for longer times.

For DAFA26, as the annealing time increased from 2.4 h to 240 h, the yield strength decreased from 700 MPa to 485 MPa. The yield strength of 2.4 h aged DAFA26 is similar to 24 h aged DAFA26. As the annealing time increased from 2.4 h to 240 h, the yield strength of DAFA29 decreased from 731 MPa to 514 MPa after 240 h aging. The yield strength of DAFA29 decreased gradually upon annealing for longer times. The elongation of all aged DAFA9 only changed slightly, while the elongation for aged DAFA29 increased with aging time. A summary of yield strength, ultimate tensile strength, and elongation for aged DAFA26 and DAFA29 is shown in Table 7.

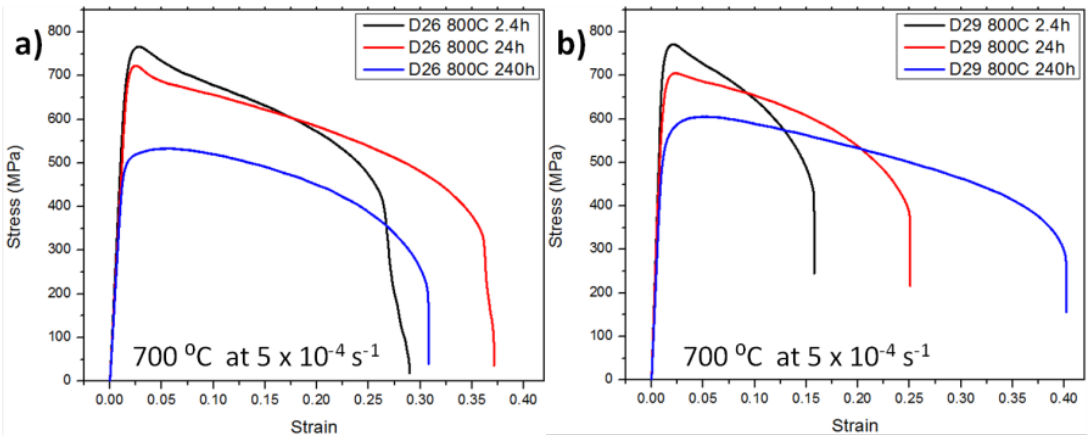

Figure 45: Tensile test results at 700ºC of (a) aged DAFA26 and (b) aged DAFA29. All tests were performed at an initial strain rate of 5 × 10^{-4} s^{-1}.

Table 7: Summary of yield strength, ultimate tensile strength, and elongation for aged DAFA26 and DAFA29 alloys (The data are based on three tests for each specimen)

	DAFA26			DAFA29		
Materials	**YS (MPa)**	**UTS (MPa)**	**Elongation (%)**	**YS (MPa)**	**UTS (MPa)**	**Elongation (%)**
As-received	512	582	30	504	601	26
2.4h	711	766	27	731	771	15
24h	696	723	33	678	705	23
240h	485	533	30	518	605	38

Figure 46 shows the fracture surfaces for 240 h-aged DAFA26 and DAFA29, respectively. Both of the fracture surfaces show dimples, indicating ductile fracture.

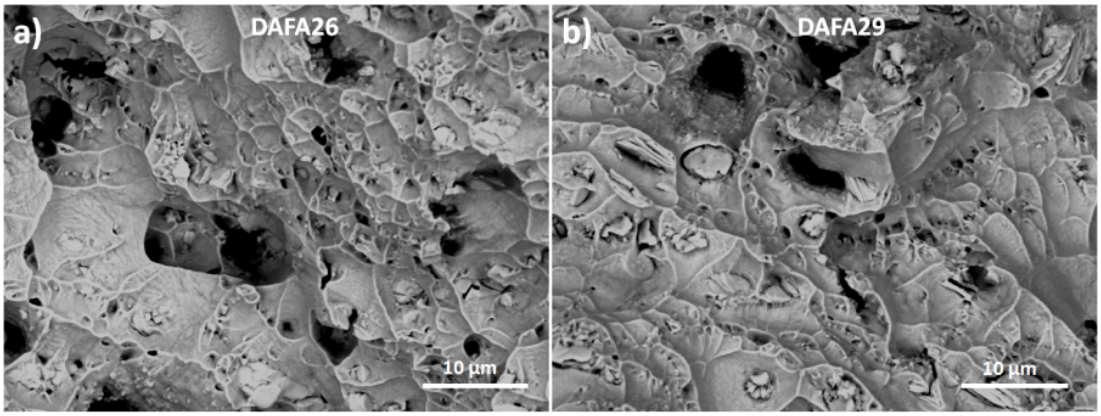

Figure 46: Fracture surfaces of (a) 240 h-aged DAFA26 and (b) 240 h-aged DAFA29 after tensile tests at 700ºC with an initial strain rate of 5 × 10^{-4} s^{-1}.

After aging 2.4 hours, both DAFA26 and DAFA29 achieved their highest yield strengths at 700ºC compared to samples aged at longer times. This indicates that the maximum strengthening effect from $L1_2$ precipitates can be obtained by aging less than 24 h ($L1_2$ particle diameter is less than 55 nm). Figure 47 shows the yield strength and elongation as function of aging time. The yield strength first increased and then decreased due to $L1_2$ precipitate coarsening. The elongation for both aged alloys decreased first and then increased.

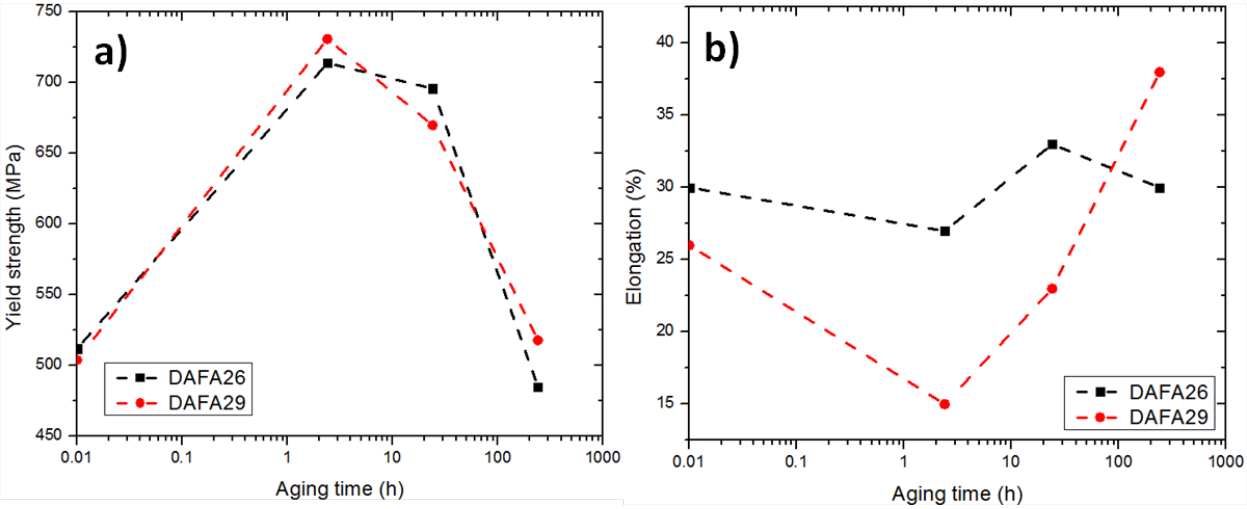

Figure 47: Yield strength and elongation of DAFA26 and DAFA29 as a function of aging time

In order to understand the origin of the yield strength obtained for all aged samples, we assume the yield strength was related to the grain size obtained, according to the Hall-Petch relationship:

$$\sigma_y = \sigma_0 + KD^{-0.5} \quad (5)$$

where σ_0 is the off-set stress, D is the average grain size, and K is a constant. The off-set stress can be expressed by following equation:

$$\sigma_0 = \sigma_{ppt} + \sigma_{ss} \quad (6)$$

where σ_{ppt} is strengthening contribution due to the presence of $L1_2$ precipitates, σ_{ss} is the strengthening contribution due to solid solution strengthening. σ_{ppt} can be obtained from following equation [51]:

$$\sigma_{ppt} = \left(\frac{10.8 \cdot f^{1/2}}{d}\right) \cdot ln\left(\frac{d}{2b}\right) \quad (7)$$

where b is the Burgers vector (nm), d is the particle diameter (nm), f is the precipitate volume fraction (%) and 10.8 has unit of MPa·nm. The volume fraction of $L1_2$ Ni_3Al precipitates is 15.4% in DAFA29 is and 14.8% in DAFA26 according to JMatPro simulations.

The calculated σ_{ppt} and $KD^{-0.5}$ values are shown in Table 8 for both DAFA26 and DAFA29. σ_{ss} is obtained by subtracting σ_{ppt} and $KD^{-0.5}$ values from the yield strength obtained from tensile

testing. The solution strengthening values for 240 h-aged DAFA29 is higher than 240 h-aged DAFA26. This solution strengthening must be due to boron in the f.c.c. matrix. The lattice parameter of f.c.c. matrix for 240 h-aged DAFA29 is also slightly larger than it is in 240h-aged DAFA26 presumably due to the boron.

Table 8: Calculated values of precipitate strengthening and solution strengthening in aged DAFA26 and DAFA29.

	Aging time	YS (MPa)	σ_{ppt} (MPa)	$KD^{-0.5}$ (MPa)	σ_{ss} (MPa)
DAFA26	2.4 h	710	494	51	165
	24 h	696	350	50	296
	240 h	485	184	46	255
DAFA29	2.4 h	731	514	38	179
	24 h	678	362	36	280
	240 h	514	190	34	290

240h-aged DAFA29 shows much higher elongation than 240h-aged DAFA26. This elongation difference might be due to the boron influence. It has been found previously that boron additions can increase the ductility of some intermetallics and alloys [52, 53]. Wang et al. [54] found boron can improve the elongation by 50 % to 100 % of Fe-Ni alloys after heat treatments at temperatures from 650-700ºC. The boron addition increased the grain boundary strength (increase or more obvious dimples) of these Fe-Ni alloys and optimized the $M_{23}C_6$ carbides distribution at grain boundaries. Zhou et al. [55] found boron doping of the nickel-based superalloy M951 increased its tensile elongation from 8 % to 28 % in tensile tests at 1100ºC. The boron increases the dislocation motion in the grain boundary and dissipates the strain at the head of dislocation pileups in the vicinity of grain boundaries. These will prevent premature micro-crack formation and consequently produce better ductility [55]. Chiu et al. [56] studied the effect of 0.5 at.% boron doping on the mechanical properties γ/γ' nickel-aluminum alloys. Boron doping caused >30 % improvements in tensile elongation for the alloy after homogenization at 1100ºC and prolonged annealing at 1200ºC. The ductility enhancement by boron has also been observed in other alloy system such as Co-Al-W high-temperature alloys during high temperature tensile tests [57].

Figure 48a and b shows the grain boundary precipitates coverage and elongation as a function of aging time for both aged DAFA26 and DAFA29. The grain boundary precipitates coverage increased as the aging time increased for both DAFA26 and DAFA29. The elongation of DAFA29 also increased as the aging increased from 2.4 h to 240 h, while the elongation for DAFA26 increased first and then decreased slightly. Figure 48c shows the grain boundary coverage as a function of elongation for both aged DAFA26 and DAFA29. A correlation between grain boundary coverage and elongation for DAFA29 is found, but not for DAFA26. This might again be associated with the boron segregating to the grain boundaries at longer aging times. It was found that boron was preferentially located at the interface between the matrix and

the grain boundary precipitates. Tytko et al. [43] found boron enrichment at $M_{23}C_6/\gamma$ interfaces in Nickel based superalloy (617B) using atom probe tomography. Li et al. [42] also found that boron was preferentially located at the phase interface of the grain boundary precipitate Ni_3Ti and the f.c.c. matrix in Ni-Fe alloy using APT. Such boron enrichment was also observed in Fe_2Nb laves phase precipitates in Fe-20Cr-30Ni-2Nb (at.%) alloys [40, 41]. As the annealing time increases, grain boundary precipitate coverage will increase in DAFA29. With the coverage increase, more boron will segregate to the grain boundary precipitates interfaces and result in better ductility.

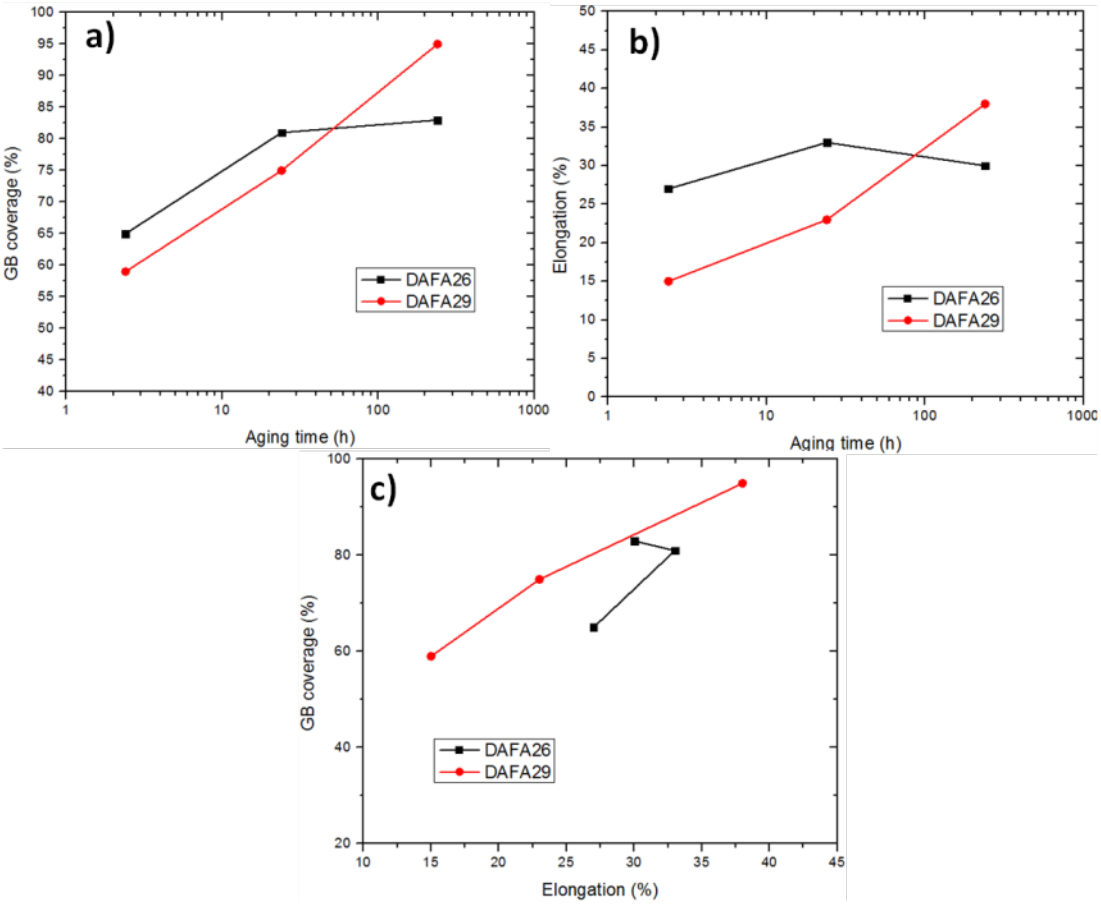

Figure 48: (a) Grain boundary coverage and (b) elongation at failure as a function of aging time; (c) grain boundary coverage as a function of elongation for both aged DAFA26 and DAFA29.

2.2.10 Analysis of Creep-Tested DAFA 29

DAFA 29 specimens were analyzed after creep failure from tests performed at both 750°C/100 MPa and 700°C/170 MPa at Carpenter Technology.

Figure 49 shows a gamma-prime strengthened AFA stainless steel sample after being creep tested at 750°C and 100 MPa. It has an obvious necked region. The material fractured at 5,282 h with 39.4% elongation and 44.4% reduction in area at the neck. Figure 49b shows an optical micrograph of the fracture surface (cross-sectional view) after creep failure. Figure 49c is

the side view photograph of this fracture sample. Numerous cracks are observed in the necked reign on the edge surface perpendicular to the applied stress direction. Figure 49d, e and f are images from the creep specimen tested at 700°C and 170 MPa. This specimen fractured at 8,123 h with 35% elongation and a 40% reduction in area at the neck. There is no significant difference between the two specimens tested in the two conditions based on the optical microscope images.

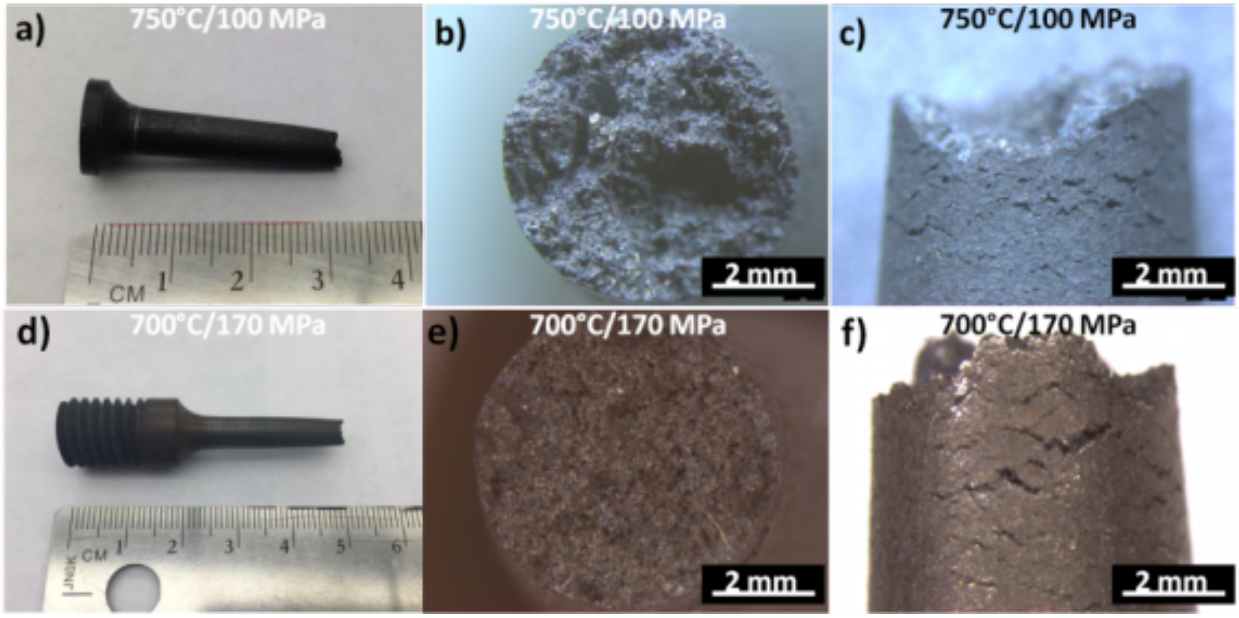

Figure 49: Photographs and optical micrographs of the gamma-prime strengthened AFA stainless steel creep tested at 750°C/100 MPa (a, b, c) and 700°C/170 MPa (d, e, f): a) and d) are photographs of the creep samples after fracture; b) and e) are cross-sectional optical micrographs of fracture surfaces; and c) and f) are side view optical micrographs.

Figure 50 shows SE images of the fracture surfaces for the samples creep tested in the two conditions. Figure 50a and b are SE images of creep sample tested at 750°C/100 MPa, while Figure 50c and d are for the creep sample tested at 700°C/170 MPa. Although the specimen tested at 750°C/100 MPa show an elongation of 39% at fracture, some cleavage surfaces (as indicated by white arrows) were observed with cavities as shown in Figure 50a. These cleavage surfaces with dimples around them indicate a mixed fracture mode. Figure 50b shows one of the cavities formed with a particle in the center at higher magnification. These microvoids (Figure 50b) were observed with a second-phase particle such as a Laves phase and/or MC carbides in the center. The second phase particles are suspected to act as the void initiator to initiate the cracks. During creep, the cracks grow gradually and form the microvoids. The fracture surface of the specimen tested at 700°C/170 MPa is shown in Figure 50c. Although the applied stress for this specimen was almost double that of the previous sample, the fracture surface is still similar to specimen in Figure 50a with many grain facets (cleavage surfaces) indicating intergranular fracture.

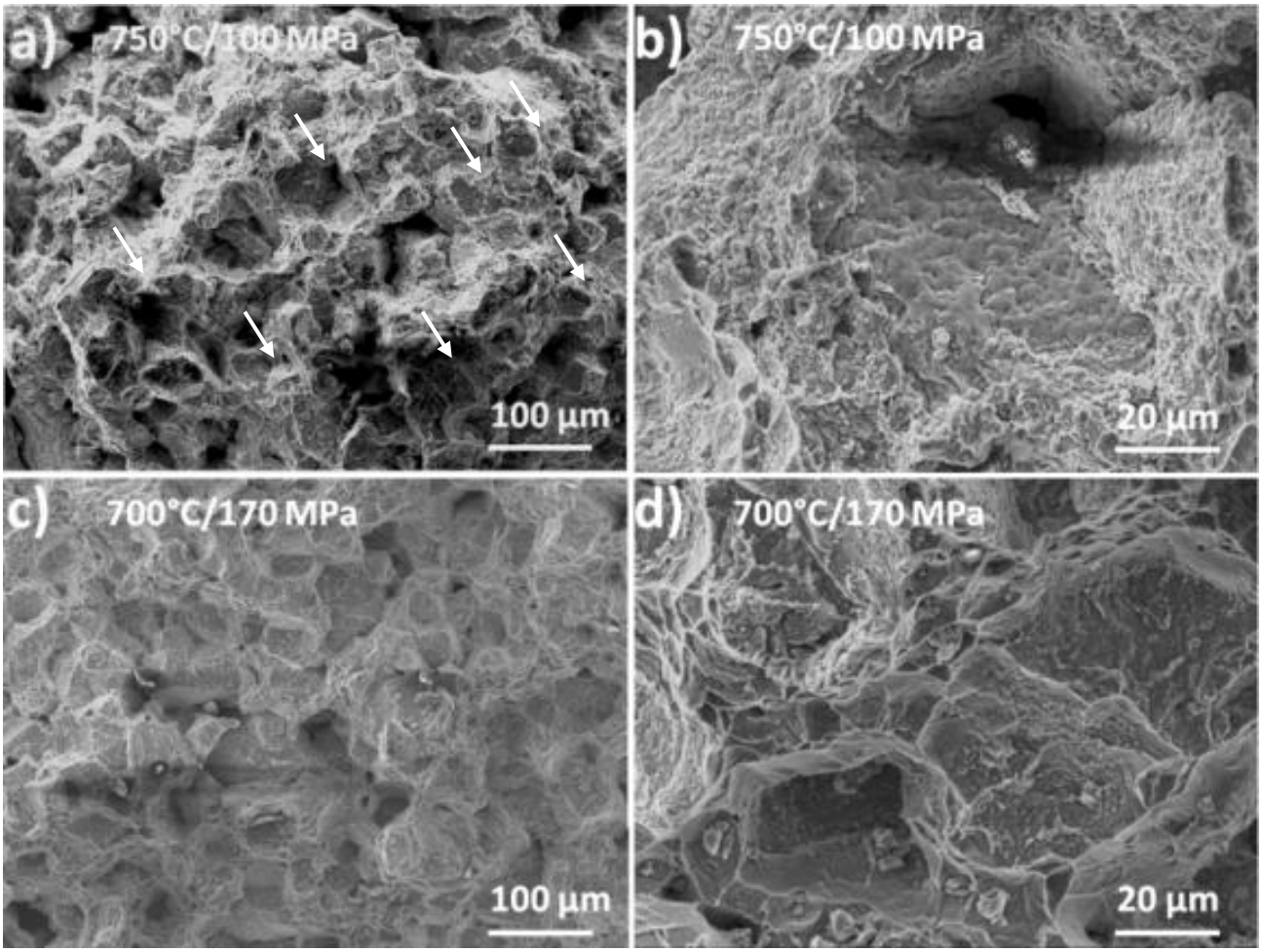

Figure 50: SE images of the fracture surfaces of the gamma-prime strengthened AFA stainless steel creep samples: a) tested at 750°C/100 MPa; b) high magnification image of a); c) tested at 700°C/170 MPa; and d) high magnification of c).

Figure 51 shows a specimen from the crept region of the AFA sample tested at 750°C/100 MPa and its control sample. The control sample is the head of the creep sample, which saw the same temperature of 750ºC for 5282 h but without any stress applied. A large number of precipitates are present in the matrix and grain boundaries for both two samples. In most cases, the B2-NiAl precipitates are spatially co-located with the Laves phase precipitates. On the grain boundaries, the B2-NiAl phase and Laves phase precipitates alternate with each other. For the sample that was creep tested (Figure 51a), the large Laves phase precipitates have fractured due to the applied stress. Small voids (dark spots in Figure 51 as indicated by yellow arrows) are observed for both two crept and control samples. The number of voids in creep-tested samples is significantly more than in the control samples.

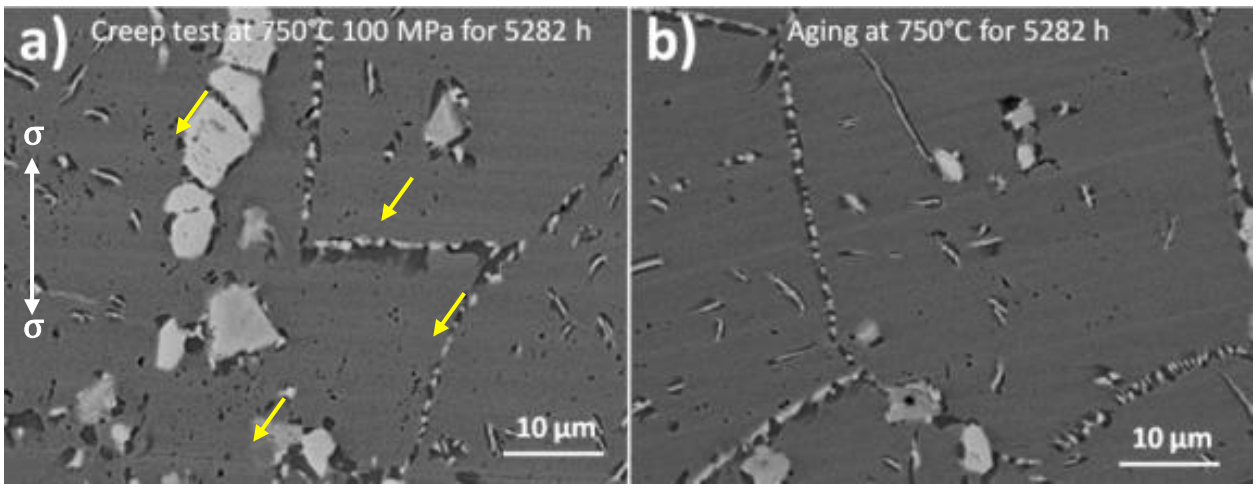

Figure 51: BSE images of (a) a sample taken from the crept region of the gamma-prime strengthened AFA stainless steel and (b) a control sample. The sample was creep tested at 750°C/100 MPa for 5282 h, while the control sample is from the head of the creep specimen which saw 750°C for the same time but no applied stress. The white arrow in (a) indicates the stress direction. The yellow arrows point to small voids.

Figure 52 shows BSE images of one of the cracked regions in AFA stainless steel creep failure samples after creep testing at 750°C/100MPa. Cracks are observed on the grain boundaries where small Laves phase and NiAl precipitates are located. Most of the cracks initiated from the second phase precipitates and propagated along the grain boundaries where most of Laves and B2 phase precipitates exist. The grain boundary region behaves as a weak path for crack propagation.

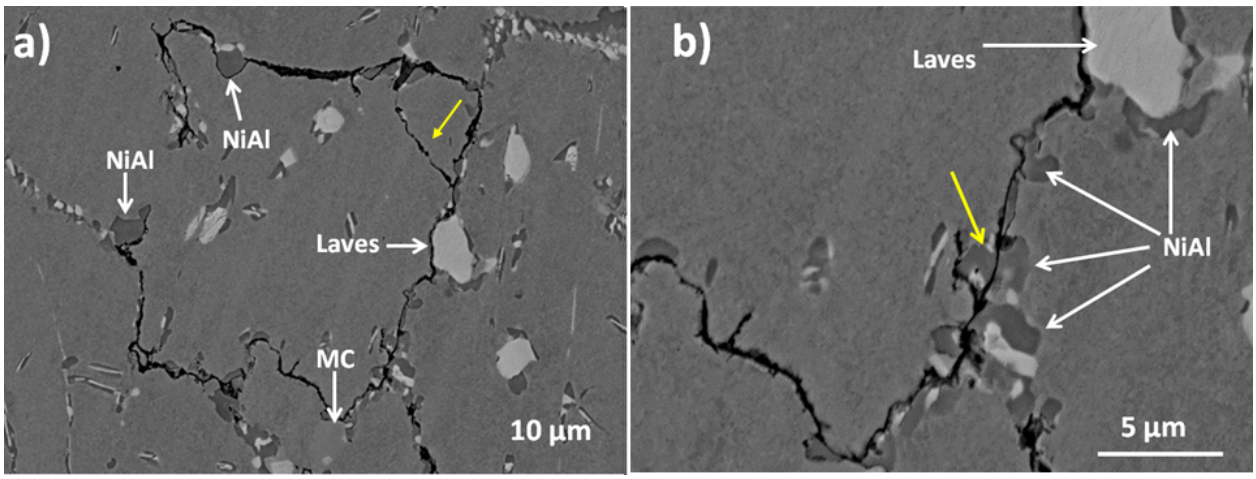

Figure 52: BSE images of the polished surface in the strained region of AFA stainless steel creep failure sample after 750°C/100 MPa test for 5282 h, (a) cracks on grain boundaries, (b) higher magnification image of (a).

Interestingly, most of cracks are around the edge of the NiAl and Laves phase precipitates, as shown in Figure 52a. A precipitates free zone (PFZ) is located on the edge of these precipitates.

Cracks also go through some of NiAl precipitates as shown in Figure 52b (indicated by a yellow arrow). The NiAl has a solvus temperature around 800°C in this alloy system according to simulation using JMatPro software. The NiAl is relatively soft when creep tested at 750°C, which is close to its solvus temperature. There is a transgranular crack observed inside the grain, as indicated by a yellow arrow in Figure 52a. In some of grain boundaries, cracks also exist even though there are no obvious grain boundary precipitates. This is shown in the lower left corner of Figure 52b. No cracking of precipitates that are present in the f.c.c. matrix was observed for this specimen.

The SEM was also used to characterize the microstructure of the sample tested at 700°C/170MPa. Figure 53 shows a comparison of microstructures of a crept sample and the corresponding control sample. There are fewer grain boundary precipitates present compared to the sample tested at 750°C/100MPa, see Figure 53, due to the lower testing temperature. In this case, no fractured large Laves phase precipitates were observed.

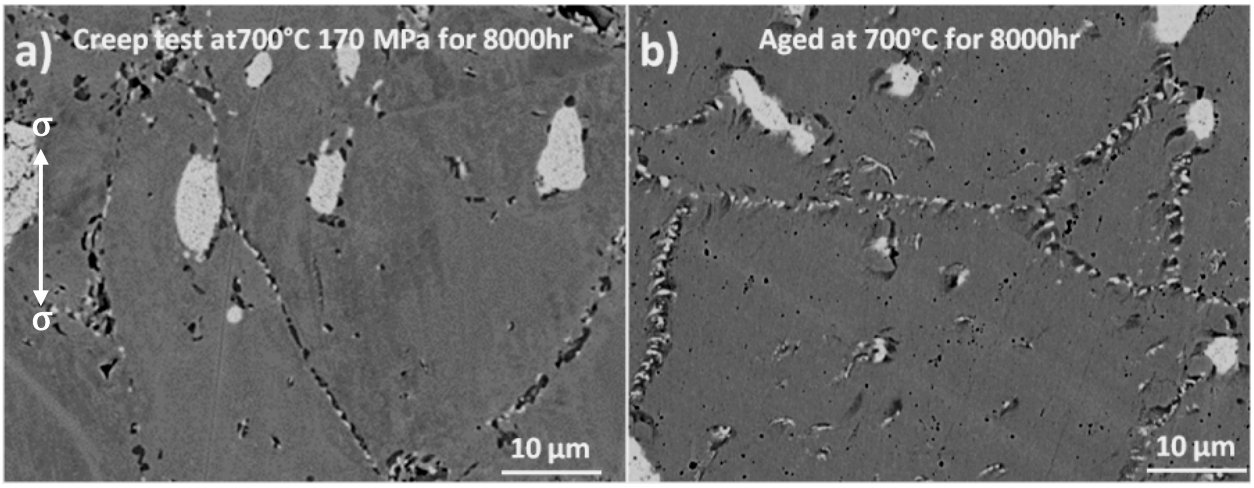

Figure 53: BSE images of (a) sample from the crept region, and (b) a control sample. The failed creep sample saw 700°C/170 MPa for 8123 h, while the control sample is from the head of the creep specimen which saw 700°C for the same time but no applied stress.

Figure 54 shows the cracks in the crept region in the AFA alloy after testing at 700°C/170 MPa. The applied stress is almost double that of the first test condition. Cracks in the grain boundary Laves phase were present as shown in both Figure 54a and b. Most of cracks propagate on the edge of precipitates where a PFZ is located. The PFZ is likely weak due to the lack of precipitates.

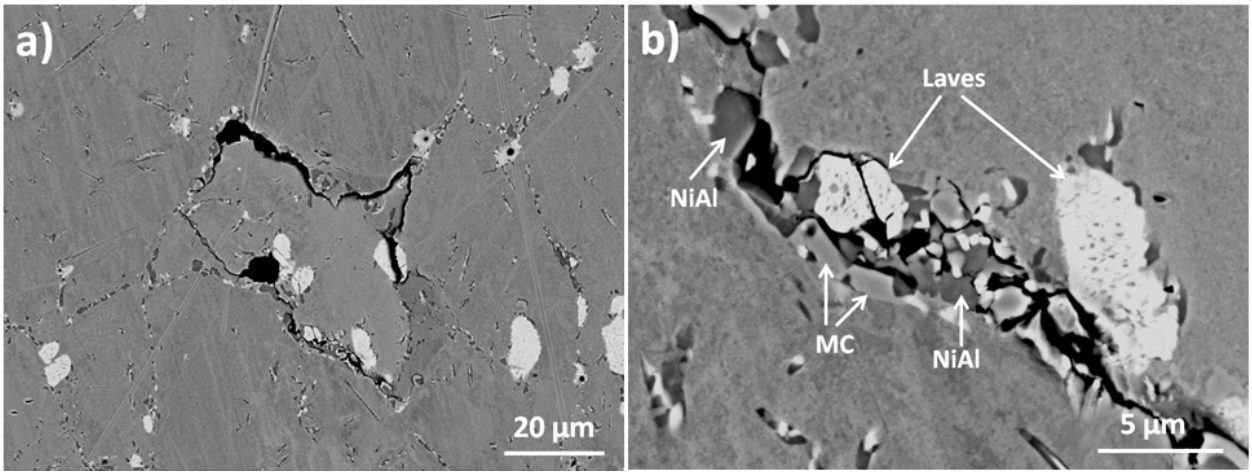

Figure 54: BSE images of cracks in the strained region of the AFA alloy creep failure sample after 700°C/170 MPa for 8123 h, (a) cracks along the grain boundaries of one grain, (b) higher magnification image of a).

Figure 55 shows a BSE image of the electrochemically polished AFA stainless steel after creep testing at 750°C/100 MPa. Laves and B2 phases appeared on the matrix surface due to the different electrochemical etching rates between them and the f.c.c. matrix. Spherical $L1_2$ precipitates are visible in the f.c.c. matrix and appear as the tiny spherical particles even after 5282 h creep testing. On the grain boundaries, there are Laves phase and B2-NiAl phase precipitates, and there is a clear PFZ between the grain boundary and the precipitates there and the f.c.c. matrix.

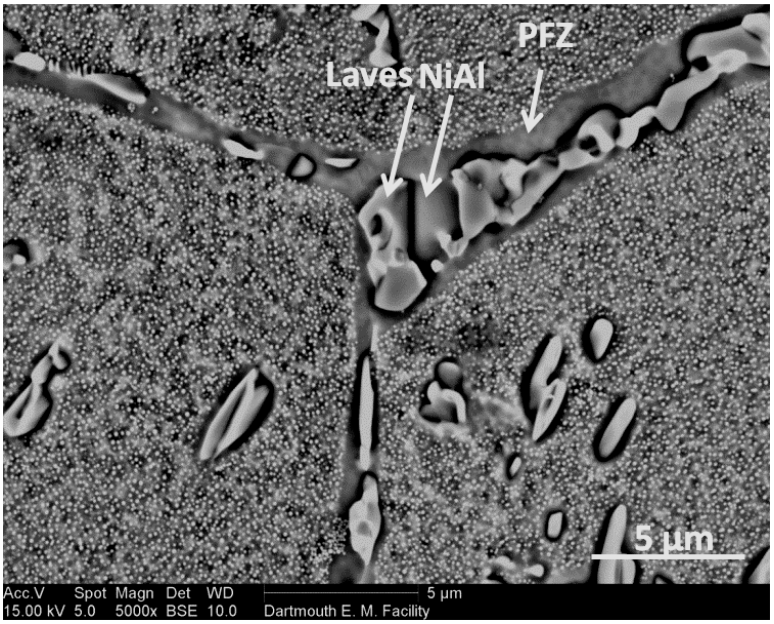

Figure 55: BSE image of electrochemically-polished surface after creep testing at 750°C/100 MPa for 5282 h. The large precipitates in f.c.c. matrix are the co-precipitates of Laves phase and NiAl precipitates, while the small precipitates in matrix are $L1_2$ precipitates.

In order to see this PFZ at higher magnification, a TEM was used to perform further analysis. Figure 56 shows a BF TEM image of a B2-NiAl precipitate and the PFZ around it. The width of the B2-NiAl precipitate is around 750 nm, while the PFZ is almost the same width as the B2 precipitate. EDS results from PFZ and f.c.c. matrix are shown in Figures 56b and c. These results show the microchemistry of the PFZ is mainly Fe, Ni and Cr, while the f.c.c. matrix is composed of Fe, Ni, Cr and Al. The f.c.c. matrix has more Ni, Al and Ti than the PFZ. This is due to the many spherical $L1_2$-structured $Ni_3(Al,Ti)$ precipitates that are present in the f.c.c. matrix. There are almost no $L1_2$-$Ni_3(Al,Ti)$ precipitates observed in the PFZ, while many $L1_2$ particles are located in the f.c.c. matrix. It is likely that the weak PFZ is where cracking occurs.

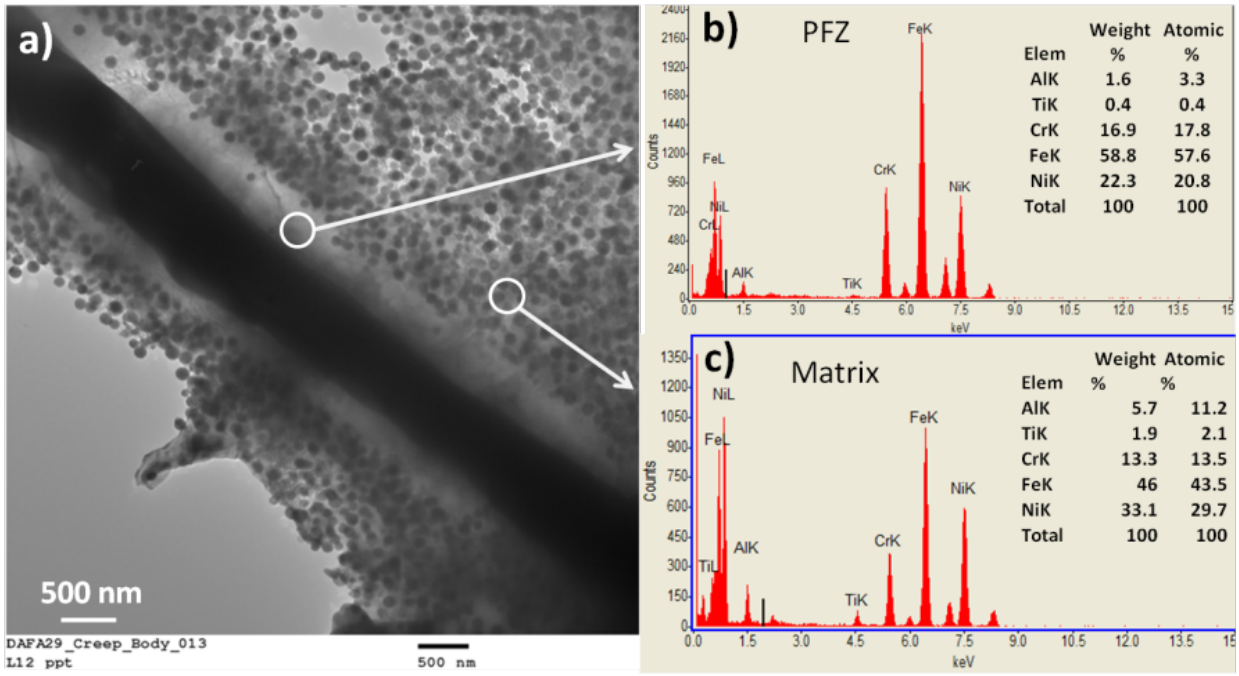

Figure 56: (a) BF TEM image of a NiAl precipitate, the PFZ around it and the surrounding f.c.c. matrix in the sample creep tested at 750°C/100 MPa for 5282 h, (b) and (c) are the EDS results from the PFZ and the f.c.c. matrix, respectively. The small precipitates are $L1_2$-$Ni_3(Al,Ti)$.

3. Summary

It was found that a solutionizing anneal at 1200ºC followed by cold rolling and annealing at 800ºC can be used to generate a finer-scale and more uniform distribution of Laves phase precipitates in as-received DAFA29 alloy. However, the solution anneal produced a large increase in grain size from 40 to 250 μm. Heat-treated DAFA29 alloys contain Fe_2Nb Laves phase, MC carbide, $Ni_3Al(Ti)$ $L1_2$, and B2 NiAl precipitates after the two thermo-mechanical treatments. During the thermo-mechanical processing, cold rolling produces a high density of dislocations, which act as nucleation sites for Fe_2Nb Laves phase, MC carbide, B2 NiAl, and $Ni_3Al(Ti)$ precipitate formation. Meanwhile, nanocrystalline grains were produced after cold rolling and short time anneals, which grow rapidly to micron-scale size on subsequent annealing at 800ºC. These nanocrystalline steels processed through large strain cold rolling (90 %) exhibit a dramatic increase in yield strength up to 1280 MPa. The yield strength decreases upon further annealing due to grain growth and precipitate coarsening. The yield strength of thermo-mechanically treated AFA steels exhibits a Hall-Petch relationship with a large value for σ_0 that likely arises from precipitate strengthening (σ_{ppt}) according to calculations.

Unfortunately, the TMT didn't increase the yield strengths of AFA alloys at 700ºC, although it significantly enhanced the yield strength of the AFA alloys at room temperature. The yield stress of TMT alloys decrease rapidly from 600ºC to 700ºC, which might be because the loss of grain boundary strengthening in TMT alloys due to fast dislocation climb at 700ºC. At this temperature, dislocation will be able to move around obstacles easily and the large volume of grain boundaries in TMT alloys work as sites of weakness. The TMT alloys have higher strain-rate sensitivity and lower activation volume compared to as-received DAFA29 at elevated temperatures. The higher strain-rate sensitivity and lower activation volume are due to the nanocrystalline grain size of the alloys. The strain rate and stress of these TMT alloys satisfy a power law relationship with the stress exponent around 5, whereas the stress exponent is around 4 for the as-received DAFA29. These values ruled out the mechanisms of bulk diffusion and grain boundary diffusion to explain the flow behavior. At 700ºC, dislocation climb appears to be the dominant mechanism for deformation of TMT alloys. When the temperature decreases to 600ºC, the mechanism might change to dislocation shearing indicated by the dramatically increased threshold stress. The flow stress of the as-received AFA alloy is insensitive to strain rate at 600ºC due to strong work hardening at this temperature. It also shows significant serrated flow on the stress-strain curve, likely associated with dynamic strain aging.

After the characterization of aged AFA alloys, we found that the largest strengthening effect from $L1_2$ precipitates can be obtained by aging less than 24 h for both AFA alloys. During aging, the coarsening behavior of $L1_2$ precipitates was the same in both DAFA26 and DAFA29, i.e.: the addition of carbon and boron has no significant effects on the lattice parameter, morphology and size of $L1_2$ precipitates in the aged AFA alloys. Both the precipitate size distributions and precipitate kinetics growth were quantified. Boron enhanced the grain boundary precipitate coverage and suppressed the coarsening of both Laves phase and B2-NiAl in the grain boundaries in the AFA alloys. The boron addition to the AFA alloys seems to suppress the formation of twins and discontinuous precipitation, which were both observed in the boron-free material. The yield strength of both DAFA26 and DAFA29 decreased as the aging time was increased. The strength loss is mainly due to the coarsening of the $L1_2$ precipitates. The higher ductility observed in 240 h-aged DAFA29 is attributed to the boron addition. The boron

appeared to increase the grain boundary strength and optimize the precipitate distribution in the grain boundaries.

Though the Laves and B2-NiAl phase precipitated along the grain boundaries can improve the creep properties, cracks were still initiated and propagated along the grain boundaries, which suggests that the grain boundaries are the weaker regions for causing fracture of the DAFA29 during creep. A wide precipitate free zone (PFZ) is observed beside the Laves phase and B2-NiAl precipitates along the grain boundaries in the DAFA29 alloy. Calculations suggested that this is a weak region when stress is applied at elevated temperature and it could potentially provide the path for the propagation of cracks.

4. Conclusions

The TMTs used in this study significantly increased the mechanical properties of AFA alloys at room temperatures due to the formation of nanocrystalline grains after cold rolling and short time anneals. However, the TMTs didn't increase the yield strengths of AFA alloys at ≥700ºC. At these temperatures, dislocation climb is the dominant mechanism for deformation of TMT alloys. The strain rate and stress of these TMT alloys satisfy a power law relationship with the stress exponent around 5, whereas the stress exponent is around 4 for the as-received DAFA29. During aging of the AFA alloys, it was found that the largest strengthening effect from $L1_2$ precipitates can be obtained by aging for less than 24 h. The yield strength of AFA alloys decreased as the aging time increased due to coarsening of $L1_2$ precipitates. Boron addition to the AFA alloys increases the grain boundary strength and improves the grain boundary precipitate distribution. Failure analysis and post-mortem TEM analysis suggested that the grain boundaries are weak regions that cause fracture of DAFA29 during creep. Although the Laves phase and B2-NiAl phase precipitated along the boundaries can improve the creep properties, the cracks were still initiated and propagated along the boundaries.

The work involved collaborations with Drs. M.K. Miller, L. Yao, Y. Yamamoto and M. P. Brady at the Oak Ridge National Laboratory and Drs. S. Chen and Z. Cai at Argonne National Laboratory. The work also involved two undergraduates Y. Sun and R. Harder. Bin Hu successfully defended his Ph.D. Thesis based on this project in November, 2015.

5. Project Outreach

Publications

1. B. Hu, G. Trotter, I. Baker, M.K. Miller, L. Yao, S. Chen, Z. Cai, "The Effects of Cold Work on the Microstructure and Mechanical Properties of Intermetallic Strengthened Alumina-Forming Austenitic Stainless Steels", Metallurgical and Materials Transactions, 46 (2015) 3773-3785.

2. B. Hu and I. Baker, “The Effect of Thermo-mechanical Treatment on the High Temperature Tensile Behavior of an Alumina-forming Austenitic Steel” , Materials Science and Engineering A, 651 (2016) 795–804.

3. G. Trotter, B. Hu, Y. Sun, R. Harder, M. K Miller, L. Yao and I. Baker, “Precipitation Kinetics During Aging of an Alumina-Forming Austenitic Stainless Steel”, Materials Science and Engineering A, **667** (2016) 147–155.

4. “Effect of Boron and Carbon Addition on Microstructure and Mechanical Properties of the Aged Gamma Prime Alumina-Forming Austenitic Alloys”, B. Hu, G. Trotter, Z. Wang, S. Chen, Z. Cai and I. Baker, submitted to Materials Science and Engineering A.

5. “Creep Failure of a Gamma Prime-Strengthened Alumina-forming Austenitic Stainless Steel”, B. Hu, I. Baker, S.J. Kernion, Y. Yamamoto and M.P. Brady, submitted to the Eighth International Conference on Advances in Materials Technology for Fossil Power Plants, Algarve, Portugal, October 10-14, 2016.

6. “Intermetallic Strengthened Alumina-Forming Austenitic Steels for Energy Applications, Bin Hu, Ph.D. Thesis, Dartmouth College 2016.

Presentations

1. The Microstructure and Mechanical Properties of AFA Stainless Steels”, I. Baker, G. Trotter, B. Hu, G. Rayner, N. Afonina, M.K. Miller, L. Yao, S. Chen, Z. Cai and P.R. Munroe, to be presented at the Eighth International Conference on Advances in Materials Technology for Fossil Power Plants, Algarve, Portugal, October 10-14, 2016.

2. B. Hu, I. Baker, " The Effects of Thermo-mechanical Treatments on the Microstructure and Mechanical Properties of Iron Based Superalloys", Materials Science & Technology 2015, Columbus, OH, USA, October 4-8 2015

3. B. Hu, I. Baker, "The Study of Thermo-Mechanical Treatments on the Microstructure and Mechanical Properties of AFA Steels", Intermetallics 2015, Bad Staffelstein, Germany, Sept 28 - Oct 2, 2015

4. B. Hu, I. Baker, "Intermetallic Strengthened Alumina-Forming Austenitic Steels for Energy Applications", Gordon Research Conferences, Biddeford, ME, USA, July 19-26, 2015

5. B. Hu, I. Baker, "Intermetallic Strengthened Alumina-Forming Austenitic Steels for Coal-Fired Power Systems", 2015 NETL Crosscutting Research Review Meeting, Pittsburgh, PA, USA, April 27-30, 2015

6. B. Hu, G. Trotter, I. Baker, “The Effects of Thermo-mechanical Treatment on the Microstructure and Mechanical Properties of Iron Based Superalloys”, 2014 MRS Fall Meeting, Boston, MA, USA, November 30-December 5, 2014

7. B. Hu, G. Trotter, I. Baker, “The Effects of Cold Work and Heat Treatment on the Microstructure and Mechanical Properties of Iron Based Superalloys”, Materials Science & Technology 2014, Pittsburgh, PA, USA, October 12-16, 2014

8. B. Hu, G. Trotter, I. Baker, "The Effects of Thermo-mechanical Treatments on the Microstructure and Mechanical Properties of Iron Based Superalloy", 2014 NETL Crosscutting Research Review Meeting, Pittsburgh, PA, USA, May 19-23, 2014

9. B. Hu, G. Trotter, L. Yao, M. K. Miller, Y. Yamamoto, M. P. Brady, I. Baker, “Intermetallic Strengthened Alumina-Forming Austenitic Steels for Energy Application”, Materials Science & Technology 2013, Montreal, Quebec, Canada, October 27-30, 2013

10. B. Hu, G. Trotter, Y. Yamamoto, M. P. Brady, I. Baker, "Laves Phase-Strengthened Austenitic Steels for Energy Applications", Gordon Research Conferences, Biddeford, ME, USA, August 11-16, 2013.

6. References:

[1] R.W. Swindeman, P.J. Maziasz, E. Bolling, J.F. King, in, 1990, pp. 125.
[2] R.W. Swindeman, P.J. Maziasz, The effect of MC forming additions and 10% cold work on the high temperature strength of 20Cr-30Ni-Fe alloys, 1991.
[3] Y. Yamamoto, M.P. Brady, Z.P. Lu, C.T. Liu, M. Takeyama, P.J. Maziasz, B.A. Pint, Metallurgical and Materials Transactions A, 38 (2007) 2737-2746.
[4] Y. Yamamoto, M.P. Brady, M.L. Santella, H. Bei, P.J. Maziasz, B.A. Pint, Metallurgical and Materials Transactions A, 42 (2011) 922-931.
[5] Y. Yamamoto, M.L. Santella, M.P. Brady, H. Bei, P.J. Maziasz, Metallurgical and Materials Transactions A, 40 (2009) 1868-1880.
[6] G. Trotter, G. Rayner, I. Baker, P.R. Munroe, Intermetallics, 53 (2014) 120-128.
[7] Y. Yamamoto, M. Govindarajan, M.P. Brady, Scripta Materialia, 69 (2013) 816-819.
[8] S. Rajasekhara, P. Ferreira, L. Karjalainen, A. Kyröläinen, Metall and Mat Trans A, 38 (2007) 1202-1210.
[9] J. Moon, M.-H. Jang, J.-Y. Kang, T.-H. Lee, Materials Characterization, 87 (2014) 12-18.
[10] Z. Zhong, Y. Gu, Y. Yuan, T. Yokokawa, H. Harada, Materials Characterization, 67 (2012) 101-111.
[11] K. Kumar, P. Hazzledine, Intermetallics, 12 (2004) 763-770.
[12] K. Kumar, L. Pang, C. Liu, J. Horton, E. Kenik, Acta Materialia, 48 (2000) 911-923.
[13] C. Allen, P. Delavignette, S. Amelinckx, Physica status solidi (a), 9 (1972) 237-246.
[14] B. Hu, G. Trotter, I. Baker, M.K. Miller, L. Yao, S. Chen, Z. Cai, Metall and Mat Trans A, 46 (2015) 3773-3785.
[15] K. Ma, H. Wen, T. Hu, T.D. Topping, D. Isheim, D.N. Seidman, E.J. Lavernia, J.M. Schoenung, Acta Materialia, 62 (2014) 141-155.

[16] M. Dao, L. Lu, R.J. Asaro, J.T.M. De Hosson, E. Ma, Acta Materialia, 55 (2007) 4041-4065.
[17] R.J. Asaro, S. Suresh, Acta Materialia, 53 (2005) 3369-3382.
[18] L. Capolungo, Atomistic and Continuum Modeling of Nanocrystalline Materials: Deformation Mechanisms and Scale Transition, Springer Science & Business Media, 2010.
[19] S. Cheng, E. Ma, Y. Wang, L. Kecskes, K. Youssef, C. Koch, U. Trociewitz, K. Han, Acta Materialia, 53 (2005) 1521-1533.
[20] J. Chen, L. Lu, K. Lu, Scripta Materialia, 54 (2006) 1913-1918.
[21] F. Dalla Torre, P. Spätig, R. Schäublin, M. Victoria, Acta Materialia, 53 (2005) 2337-2349.
[22] Y.M. Wang, A.V. Hamza, E. Ma, Acta Materialia, 54 (2006) 2715-2726.
[23] Y. Wang, A. Hamza, E. Ma, Applied Physics Letters, 86 (2005) 241917.
[24] V. Maier, K. Durst, J. Mueller, B. Backes, H.W. Höppel, M. Göken, Journal of Materials Research, 26 (2011) 1421-1430.
[25] D. Zhou, X. Xu, H. Mao, Y. Yan, T. Nieh, Z. Lu, Materials Science and Engineering: A, 594 (2014) 246-252.
[26] J.K. Benz, L.J. Carroll, J.K. Wright, R.N. Wright, T.M. Lillo, Metall and Mat Trans A, 45 (2014) 3010-3022.
[27] O.D. Sherby, P.M. Burke, Progress in Materials Science, 13 (1968) 323-390.
[28] A. Brown, M. Ashby, Scripta Metallurgica, 14 (1980) 1297-1302.
[29] S. Zhu, S. Tjong, J. Lai, Acta Materialia, 46 (1998) 2969-2976.
[30] C. Stallybrass, A. Schneider, G. Sauthoff, Intermetallics, 13 (2005) 1263-1268.
[31] R. Lagneborg, B. Bergman, Metal Science, 10 (1976) 20-28.
[32] D.N. Seidman, E.A. Marquis, D.C. Dunand, Acta Materialia, 50 (2002) 4021-4035.
[33] E. Arzt, M.F. Ashby, Scripta Metallurgica, 16 (1982) 1285-1290.
[34] A. Smolej, B. SkAzA, M. FAzArinc, Materials and Geoenvironment, 56 (2009) 389-399.
[35] S.C. Medeiros, Y.V.R.K. Prasad, W.G. Frazier, R. Srinivasan, Materials Science and Engineering: A, 293 (2000) 198-207.
[36] W. Chen, M. Chaturvedi, Materials Science and Engineering: A, 183 (1994) 81-89.
[37] Z. Guo, H. Liang, M. Zhao, L. Rong, Materials Science and Engineering: A, 527 (2010) 6620-6625.
[38] I. Tarigan, K. Kurata, N. Takata, T. Matsuo, M. Takeyama, in: MRS Proceedings, Cambridge Univ Press, 2011, pp. mrsf10-1295-n1206-1203.
[39] I. Tarigan, N. Takata, M. Takeyama, in: Proceedings of the 12th International Conference on Creep and Fracture of Engineering Materials and Structure (JIMIS 11), 2012.
[40] S. Chen, C. Zhang, Z. Xia, H. Ishikawa, Z. Yang, Materials Science and Engineering: A, 616 (2014) 183-188.
[41] H. Ishikawa, C. Zhang, S.-W. Chen, Z.-G. Yang, Acta Metall. Sin. (Engl. Lett.), 28 (2015) 424-429.
[42] H. Li, H. Song, W. Liu, S. Xia, B. Zhou, C. Su, W. Ding, Ultramicroscopy, (2015).
[43] R. Viswanathan, W. Bakker, Journal of Materials Engineering and Performance, 10 (2001) 81-95.
[44] Z. Zhong, Y. Gu, Y. Yuan, Materials Science and Engineering: A, 622 (2015) 101-107.
[45] S. Zhao, X. Xie, G.D. Smith, S.J. Patel, Materials letters, 58 (2004) 1784-1787.
[46] S. Semboshi, J. Ikeda, A. Iwase, T. Takasugi, S. Suzuki, Materials, 8 (2015) 3467-3478.
[47] P. Venkiteswaran, M. Bright, D. Taplin, Materials Science and Engineering, 11 (1973) 255-268.

[48] D. Baither, T. Krol, E. Nembach, Philosophical Magazine, 83 (2003) 4011-4029.
[49] T. Krol, D. Baither, E. Nembach, Scripta Materialia, 48 (2003) 1189-1194.
[50] R.C. Reed, The Superalloys: Fundamentals and Applications, Cambridge University Press, 2006.
[51] G.T. B. Hu, Ian Baker, M.K. Miller, L. Yao, S. Chen, And Z. Cai, Metall and Mat Trans A, (2015).
[52] K. Aoki, O. Izumi, in, Japan Inst Metals 1-14-32, Ichibancho, Aoba-Ku, Sendai, 980-8544, Japan. P. 358-359., 1979, pp. 358-359.
[53] P. Jozwik, W. Polkowski, Z. Bojar, matrix, 36 (2015) 40.
[54] C. Wang, Y. Guo, J. Guo, L. Zhou, Materials Science and Engineering: A, (2015).
[55] P. Zhou, J. Yu, X. Sun, H. Guan, Z. Hu, Materials Science and Engineering: A, 491 (2008) 159-163.
[56] Y. Chiu, A. Ngan, Metall and Mat Trans A, 31 (2000) 3179-3186.
[57] K. Shinagawa, T. Omori, K. Oikawa, R. Kainuma, K. Ishida, Scripta Materialia, 61 (2009) 612-615.